

Design and Modeling of an Electrostrictive Inchworm Actuator

by

Stanley George Burns

B.Eng., University of Victoria, 1999

A Thesis Submitted in Partial Fulfillment of the
Requirements for the Degree of

MASTER OF APPLIED SCIENCE

in the Department of Mechanical Engineering

We accept this thesis as conforming
to the required standard

[Redacted Signature]
Dr. A. Suleman, Supervisor (Department of Mechanical Engineering)

[Redacted Signature]
Dr. J. W. Provan, Department Member (Department of Mechanical Engineering)

[Redacted Signature]
Dr. T. A. Gulliver, External Examiner (Department of Electrical Engineering)

[Redacted Signature]
Dr. E. Prasad, Outside Member (Sensor Technology Limited)

© STANLEY GEORGE BURNS, 2001

University of Victoria

All rights reserved. This thesis may not be reproduced in whole or in part, by
photocopy or other means, without the permission of the author.

Supervisor: Dr. Afzal Suleman

Abstract

The majority of high force linear actuators today are manufactured on the basis of hydraulic technology. However, there is a strong and increasing demand to switch to electric technology. Applications for such actuators include the car, airplane, and space industries. The concept is by no means a new one, but the present research proposes a proof-of-concept solution in the design of large displacement and medium force inchworm actuators. The technology considered uses an electrostrictive mechanism that “walks” inside an outer casing. This motion emulates an inchworm, summing small steps to achieve large displacements.

The conceptual design of the electrostrictive inchworm actuator was carried out using the finite element analysis. A prototype was constructed based on the numerical simulation results. With the design validated, some applications were explored by optimizing the structural strength of variable geometry adaptive truss structures.

Exam

Dr. A. Suleman, Supervisor (Department of Mechanical Engineering)

Dr. J. W. Provan, Department Member (Department of Mechanical Engineering)

Dr. T. A. Gulliver, External Examiner (Department of Electrical Engineering)

Dr. E. Prasad, Outside Member (Sensor Technology Limited)

TABLE OF CONTENTS

1.	Introduction	1
1.1.	Background and Motivation	1
1.2.	Thesis Objectives	2
1.3.	State of the Art	2
1.4.	Past Inchworm Designs	6
1.5.	Added Value of the Research	10
1.6.	Electromechanical Materials.....	10
	The Piezoelectric Effect	12
	The Electrostriction Effect	13
1.7.	Piezoceramic Stacks	15
1.8.	Proposed Inchworm Actuator	16
1.9.	Thesis Layout.....	17
2.	Actuator Design and Modeling.....	18
2.1.	Actuator Specifications	18
2.2.	Material Selection	18
2.3.	Conceptual Design	19
2.4.	Finite Element Modeling.....	23
	Piezoelectric/Electrostrictive Stack Modeling.....	24
	Brake Assembly Modeling.....	27
2.5.	Brake Assembly Design Optimization.....	29
	Fixed Dimensions	29
	Free Dimensions	30
2.6.	Performance Criteria	31
	The Range.....	32
	The Blocked Force.....	32
	The Fatigue Safety Factor	33
2.7.	Parametric Analysis.....	35
	Notch Thickness (NT).....	35
	Shoulder Thickness.....	36
	Arm Thickness.....	36
	Arm Angle.....	37
	Notch Diameter.....	37
	Casing Pre-Stress	38
2.8.	Final Design.....	45
2.9.	Finite Element Mesh Study	47
3.	Actuator Prototype and Testing.....	49
3.1.	Electrostrictive Stacks	49
3.2.	The Inner Crawler	50
3.3.	Outer Casing	53
3.4.	Controller Design	54
3.5.	Prototype Results	58
4.	Adaptive Truss Structures	61
4.1.	The Concept.....	62
	One-Story Truss.....	63
4.2.	Optimization Algorithms.....	68
	Ansys Optimization	68

MatLab optimization.....	70
4.3. Two-Story Truss	71
4.4. Pyramid Structure.....	77
4.5. Dome Structure	79
4.6. Asymmetric Truss Structure	82
4.7. Symmetric Truss Structure	85
4.8. Tower Structure.....	89
5. Conclusions and Future Work	93

LIST OF FIGURES

Figure 1-1 Ferroelectric hysteresis loop generated by a cyclic electric field.....	11
Figure 1-2 Strain vs. electric field plot for a ferroelectric piezoelectric (PZT)	13
Figure 1-3 Strain vs. electric field for an electrostrictive (PMN)	14
Figure 1-4 Proposed electrostrictive inchworm actuator.....	16
Figure 2-1 Conceptual inchworm actuator design model original design	20
Figure 2-2 Different flexure orientations.....	21
Figure 2-3 Selected conceptual design	22
Figure 2-4 Inchworm actuator stack actuation sequence.....	23
Figure 2-5 SOLID98 tetrahedral coupled-field solid	24
Figure 2-6 Ansys model of stack.....	25
Figure 2-7 Graph of %strain vs. electric field for BM600.....	26
Figure 2-8 Graph of %strain vs. electric field for BM600 (zoom).....	26
Figure 2-9 Finite element model for the flextensional frame and stack with nuts.....	28
Figure 2-10 Actuator design dimensions	30
Figure 2-11 Brake assembly free dimensions	31
Figure 2-12 Brake assembly range	32
Figure 2-13 Brake assembly in contact with outer casing	33
Figure 2-14 Arm deformation before and after snap through.....	37
Figure 2-15 Casing pre-stress vs. force exerted on adjustment nuts during actuation	38
Figure 2-16 Variation of notch thickness with free dimension design parameters	39
Figure 2-17 Variation of shoulder thickness with free dimension design parameters	40
Figure 2-18 Variation of arm thickness with free dimension design parameters.....	41
Figure 2-19 Variation of arm angle with free dimension design parameters.....	42
Figure 2-20 Variation of notch diameter with free dimension design parameters.....	43
Figure 2-21 Variation of notch diameter with free dimension design parameters.....	44
Figure 2-22 Final design modeling results.....	45
Figure 2-23 Mesh density analysis	48
Figure 3-1 Design and prototype stacks.....	50
Figure 3-2 Inner crawler	50
Figure 3-3 Flextensional frame	51
Figure 3-4 Casing pre-stress vs. force exerted on adjustment nuts before actuation ..	51
Figure 3-5 First outer casing design	53
Figure 3-6 Final outer casing design	53
Figure 3-7 Assembly of outer casing and inner crawler.....	54
Figure 3-8 Controller schematic.....	56
Figure 3-9 Controller assembly.....	57
Figure 3-10 Controller waveforms	57
Figure 3-11 Controller waveform with ramping function	58
Figure 4-1 NASDA's future geostationary platform (GPF)	61
Figure 4-2 ARES's proposed space system	62
Figure 4-3 One-story fixed truss.....	63
Figure 4-4 One-story fixed structural strength.....	64
Figure 4-5 One-story adaptive truss	64
Figure 4-6 One-story optimized structural strength in Ansys and in MatLab	65
Figure 4-7 One-story adaptive shapes	66

Figure 4-8 Structural strength of fixed and adaptive one-story trusses	67
Figure 4-9 Line representation of A1 range	69
Figure 4-10 Random values of A1 between 0° and 90°	69
Figure 4-11 Random values of A1 between 50° and 90°	69
Figure 4-12 Random values of A1 between 59° and 90°	70
Figure 4-13 Two-story adaptive truss	72
Figure 4-14 Two-story structural strength	73
Figure 4-15 Two-story adaptive shapes	74
Figure 4-16 Two-story stress contour plot with $\theta = -90^\circ$	75
Figure 4-17 Two-story stress contour plot with $\theta = -30^\circ$	76
Figure 4-18 Two-story stress contour plot with $\theta = 90^\circ$	76
Figure 4-19 Adaptive pyramid	77
Figure 4-20 Boundary conditions for the apex of the pyramid	77
Figure 4-21 Pyramid structural strength	78
Figure 4-22 Pyramid adaptive shapes	79
Figure 4-23 Dome structure	79
Figure 4-24 Dome apex boundary conditions	80
Figure 4-25 Dome structural strength	81
Figure 4-26 Adaptive dome shapes	81
Figure 4-27 Asymmetric truss structure	82
Figure 4-28 Adaptive asymmetric truss shapes	83
Figure 4-29 Asymmetric truss structural strength	84
Figure 4-30 Adaptive asymmetric truss element stresses for angles $\theta \approx 90^\circ$	84
Figure 4-31 Asymmetric truss structural strength with extra data point $\theta = -1.09^\circ$	85
Figure 4-32 Symmetric truss structure	85
Figure 4-33 Adaptive symmetric truss shapes	86
Figure 4-34 Symmetric truss structural strength	87
Figure 4-35 Symmetric truss element stresses for $\theta = 50^\circ$ and $A1 \approx 140^\circ$	87
Figure 4-36 Symmetric truss element stresses for $\theta = 60^\circ$ and $A1 \approx 150^\circ$	88
Figure 4-37 Symmetric truss element stresses for $\theta = 70^\circ$ and $A1 \approx 160^\circ$	88
Figure 4-38 Tower structure	89
Figure 4-39 Tower structural strength	90
Figure 4-40 Adaptive tower shape for F at $\theta = 0^\circ$, $\beta = 0^\circ$ and $\theta = 12.5^\circ$, $\beta = 0^\circ$	91
Figure 4-41 Adaptive tower shape for F at $\theta = 38^\circ$ and $\beta = 33^\circ$	92

LIST OF TABLES

Table 1-1 Inchworm actuator designs and patents reported in the published literature	9
Table 1-2 Properties of piezoelectric material BM500.....	13
Table 1-3 Properties of electrostrictive material BM600	14
Table 2-1 Actuator design specifications.....	18
Table 2-2 Thermal expansion and elastic properties for various metals	19
Table 2-3 Comparison of free displacement of BM500 and BM600	27
Table 2-4 Ansys design model results	46
Table 2-5 Actuator output force	47
Table 3-1 Comparison of design and prototype stacks.....	49
Table 3-2 Brake assembly results of Ansys prototype model and prototype.....	59
Table 4-1 One-story comparison of structural strength and optimized angle.....	66
Table 4-2 One-story results	67
Table 4-3 Two-story results	72
Table 4-4 Local minima convergence for the two-story truss with $\theta = -90^\circ$	75
Table 4-5 Pyramid results	78
Table 4-6 Dome results	80
Table 4-7 Asymmetric truss results	83
Table 4-8 Symmetric truss results	86
Table 4-9 Tower results	90
Table 4-10 Adaptive tower results for F at $\theta = 38^\circ$, $\beta = 33^\circ$	92
Table 5-1 Summary of inchworm actuator results	96

Acknowledgements

I would like to thank my supervisor, Dr. Afzal Suleman, for his guidance in both academic and personal matters. He provided me with a platform on which to expand my horizons, and further my knowledge and understanding in mechatronics and adaptive structures.

I am also grateful to Dr. Eswar Prasad of Sensor Technology Limited for the financial support and recommendations he provided me with through the various stages of my work. A special thank you goes to Dr. Dave Waechter for his dedication and perseverance during the course of this project.

Credit must also be given to Dr. James Provan for his guidance, advice and motivation as a member of the supervisory committee.

A big thank you to my office mates for making my work environment so enjoyable. To Ramin Sedaghati who kept the atmosphere light with his Persian humor. To Ana Filipa, who helped to deepen my appreciation for the Portuguese culture. To Jeff Schoenfeld, who helped out in a time of need, and to Rodney Katz for his machining talents.

Thank you all for your help and support.

To Kelly Coolen, and Jeff Schoenfeld.

INTRODUCTION

Over the past decade, new fields of engineering have emerged from a surge of invention and innovation, led by multifunctional materials. In particular, the emerging science of multifunctional materials has spurred progress in the engineering field to enhance the performance of structural systems. The new technologies have invited us to revise the engineering rules, not only because they spur new industries but also because they embody a sweeping capacity to lower the weight and cost of designing and manufacturing new structural systems while improving overall performance.

Most of the high force linear actuators in use today are manufactured on the basis of hydraulic technology. There is a strong demand to switch to electric technology. From environmental, health and safety points of view, the use of flammable and toxic fluids would be eliminated. From technical and economical points of view, the electric actuators would improve the efficiency of the control systems and remove the electro-hydraulic interface. The thesis presents the design, modeling and proof-of-concept experimental prototype of an electrostrictive inchworm actuator.

1.1. Background and Motivation

Hydraulic actuators offer high force and large displacement capabilities. They provide variable stroke outputs over a large frequency range. For these reasons, they are the actuators of choice for many aerospace, automotive, and robotic applications. The main drawbacks to hydraulic actuators are that they rely on toxic fluids and require a hydraulic pressure generator that increases the weight, complexity and power wastage of the system. For example, the brake system of a vehicle contains 0.7 liters of fluid. Assuming that 70% of the fluid is recovered during the recycling process, approximately 8,000 tons are emitted into the environment during one year. Brake fluids contain carcinogenic oligoglycol ethers, and corrosion inhibitors, such as benzotriazols or tolyltriazols, which are classified as water polluting [1]. Another drawback to hydraulic actuators is the flammability of the hydraulic fluid. Some applications are designed such that the hydraulic actuators carrying flammable

hydraulic fluids are close to braking disks that heat up during operation. The risks and limitations of hydraulic systems have prompted research and development of alternative linear actuators.

Electromagnetic linear actuators have existed for decades. This device delivers limited stroke and force as the total energy is restricted by the electrical energy stored in the coil. In addition, the device is rather bulky, expensive, limited in frequency (due to large inertia) and presents a potential safety hazard in the case of a power failure.

1.2. Thesis Objectives

The objective behind this thesis is to develop a new electric inchworm actuator to replace existing hydraulic actuators in the framework of the more electrical car, aircraft, and spacecraft. The multifunctional piezoelectric and electrostrictive materials and devices have created opportunities for novel applications due to the unique high strain and lower voltage characteristics. Besides actuator applications, the technology may become transferable to other domains such as primary flight control actuators that require a longer stroke.

The issues addressed in the framework of this research include actuator modeling and design using the finite element method, manufacturing, assembly and testing of the proof-of-concept prototype, controller design and structural optimization of variable geometry trusses using the new inchworm actuators as active elements.

1.3. State of the Art

In the last decade, technological developments in computer and materials science and mechanical and electrical engineering have evolved to the point where their synergistic combination have culminated in the new field of multi-disciplinary research in “mechatronics”. The advances in material sciences have provided a comprehensive and theoretical framework for implementing multifunctionality into materials and the development of high speed digital computers has permitted the transformation of that framework into methodologies for practical design and production. The concept is elementary: a highly integrated sensor system provides data on the environment of the structures to a processing and control system, which in turn signals integrated actuators to modify the structural properties in an appropriate

fashion. In addition, this integrated system has a functionality that adds significant value to materials, technologies and end-products, by enabling system performance enhancements that are not possible with traditional approaches. Mechatronic systems offer substantial near-term business potential across a broad range of technologies, applications and markets.

There are several key technological developments that have combined to establish the potential feasibility of mechatronic systems. One of the advances is the development of functional materials and their utilization in devices such as distributed actuators and sensors. The other development comes from the field of electrical engineering, with the advent of new algorithms and signal processing technologies. The pursuit of advanced multifunctional materials with related electro-magneto-thermo-mechano-rheological properties has opened up new horizons in terms of actuation simplicity, compactness and miniaturization potential. The most recognized types of materials are shape memory alloys, magnetostrictive materials and piezoelectrics, which develop strains (or displacements) when exposed to thermal, magnetic and electric fields, respectively.

The shape memory effect occurs in a number of alloys that undergo a special type of phase transformation, called the thermoelastic martensite transformation. When this deformed material is subsequently heated above a critical temperature, the martensitic phase reverts to the original austenitic phase and the material recovers its original pre-deformed shape. The most common commercially available Shape Memory Alloy (SMA) is the Ni-Ti alloy. Nitinol is very ductile, can be easily deformed, and has good strength and strain rate.

Magnetostrictive materials exhibit a change in dimension when placed in a magnetic field. Terfenol-D, (Tb, Dy, Fe), is the most popular and commercially available magnetostrictive material. Recent research on magnetostrictive materials shows that they provide strokes significantly larger than their electromechanical counterparts, but they tend to be difficult to implement in structural systems because of the surrounding bulk of magnetic field generators.

The electrostrictive phenomenon is a nonlinear property which exists in all dielectric materials. Some of these materials can offer higher electrically induced strains with

lower hysteresis than piezoelectric materials. The strain is proportional to the square of the applied electric field and independent of its polarity. The most promising electrostrictive material is lead magnesium niobate (PMN); however, this material is still not widely available on the commercial market. Constitutive models for electrostrictors are not as mature as models for piezoelectrics, due to the nonlinearities.

Magneto-rheological and electro-rheological fluids used in vibration damping problems have been the subject of considerable research since these materials exhibit fast, reversible and controllable changes in behavior. However, in spite of advances in sensing and controls, fundamental rheological research as applied to vibration damping has lagged behind.

Piezoelectric behavior can be manifested in two distinct ways. The direct piezoelectric effect occurs when a piezoelectric material becomes electrically charged when subjected to a mechanical stress. As a result, these devices can be used to detect strain, movement, force, pressure, or vibration by developing appropriate electrical responses, as in the case of force and acoustic sensors. The converse piezoelectric effect occurs when the piezoelectric material becomes strained when placed in an electric field. The ability to induce strain can be used to generate a movement, force, pressure, or vibration through the application of a suitable electric field. The most promising commercial piezoelectric materials are lead zirconate titanate (PZT) and polyvinylidene fluoride (PVDF).

PZT's offer low strains ($\sim 0.06\%$) with significant hysteresis ($\sim 15-20\%$), whereas electrostrictive PMN materials exhibit higher strains ($\sim 0.1\%$) with lower hysteresis ($\sim 1-4\%$). However, the temperature operating limits for PMN would require that it be specially insulated for any type of outer space application. For all other considerations, PMN would be handled similarly to PZT and actuator designs for one material could be applied to the other. While PZT is a preferred material for most applications, future commercial applications may favor a direct replacement of PZT with PMN because of its increased strain capabilities and superior hysteresis efficiency. The shape memory material Nitinol is very ductile and thus produces the greatest displacement albeit the weakest force of the actuators under consideration. However, it does have the advantage of being easily shaped into different actuator

geometries. Nitinol is less desirable from the point of view of precision and economy of design due to its power consumption, accuracy and hysteresis characteristics. It can also be observed that Terfenol-D and PZT compare very closely in the displacement characteristics. In structures, the most widely used multifunctional materials to date have been piezoelectrics. Piezoelectrics have higher bandwidths than are possible in shape memory alloys, they are more compact than magnetostrictive devices and they are bi-directional, unlike electrostrictives.

Electric field controlled actuators can provide lightweight, accurate and reliable linear actuation. Piezoelectric and electrostrictive elements have low displacements, but offer very large force capabilities [2,3]. Larger displacements can be achieved by stacking piezoelectric or electrostrictive elements and summing small incremental steps (inchworm movement). The potential now exists for electric field controlled actuators to deliver high forces over large displacements and to compete effectively with hydraulic systems. These actuators are being used in micro-positioning xy-tables, ultrasonic motors, impact printer heads, vehicle suspensions, and precision machining equipment [4,5].

The development of electric field controlled actuators, also referred to as strain-induced actuators, has also been addressed in a variety of outer space applications. Primary attention during the last decade has been given to research in the area of variable geometry truss structures [6-10]. For example, electrostrictive actuators are used in the correction of the aberrations in the Hubble Telescope. Variable geometry truss structures can adopt a wide range of geometric configurations by lengthening or shortening some of their active elements, each containing a strain-induced actuator. This ability allows these structures to adopt configurations that maximize their structural strength. These structures may also use strain-induced actuators to produce damping effects to suppress vibrations [11,12]. This technology has been integral to many space truss systems including large span roof trusses, space reflectors, and robotic arms [6]. Other applications include release mechanisms, positioning devices, shape control of large flexible surfaces, dexterity and obstacle avoidance [13].

1.4. Past Inchworm Designs

A publication and patent search was performed to stimulate new ideas and to prevent re-inventing old designs. This search is by no means a complete history of inchworm actuator development, but does provide a rich history of previous work. A chronological account of the documented patents and papers is presented in Table 1.1.

During the last 40 years of development, piezoceramic inchworm actuators have circled around a common theme. This theme incorporates piezoceramic stacks for gripping and extending which create actuator motion. In 1964, Stibitz [14] used a magnetostrictive material on the end of three rods. Each of the three rods would grip, release or push the inner shaft in a predetermined sequence that would actuate the shaft. McNancy [15] developed an amplification device consisting of a piezoceramic stack that was specially positioned against ball bearings. The displacement of the piezoceramic was transferred and amplified through the ball bearings. In 1966, Hsu [16] designed an actuator using a hollow cylinder with an inner clamping and extending device.

In 1967, Locher [17] developed a mechanism that used two cams to grip and release an inner shaft. The center shaft contained a piezoceramic material producing the extension. In 1968, Brisbane [18] invented an inchworm actuator using a tube and an inner crawler. The crawler had three piezoceramic elements: two for gripping and one for extension. In 1972, Galutva [19] designed an actuator, which consisted of several piezoceramic elements used for gripping and extending.

In 1975, Bizzigotti and May [20] introduced an inchworm actuator that used curved surfaces to grip the outside of a shaft. The piezoceramic on one end would grip the shaft while the center piezoceramic would extend. After extension, the piezoceramic on the other end would grip the shaft to capture the displacement. In 1976, Sakitani [21] invented the inchworm actuator that would clamp and extend on a surface providing a precise displacement.

In 1979, Ishikawa [22] developed an actuator incorporating the use of two extending and two clamping piezoceramic elements. When energized in a particular sequence the upper shaft would be forced to move horizontally. In 1980, O'Neill [23] presented the first stacked piezoceramic actuator. The idea of stacking increased the actuator

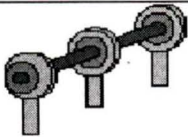
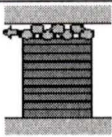
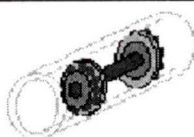
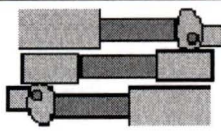
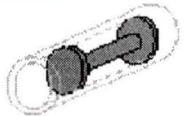
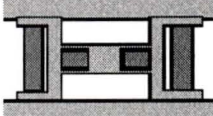
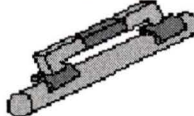
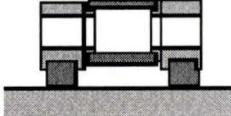
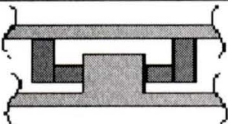
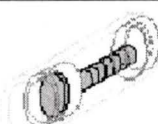
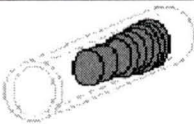
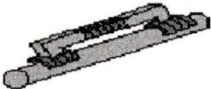
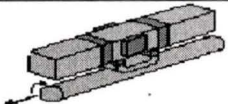

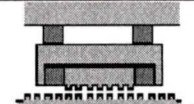
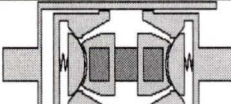
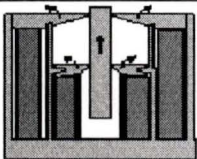
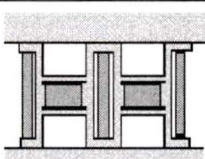
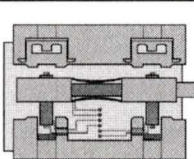
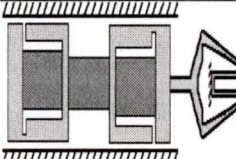
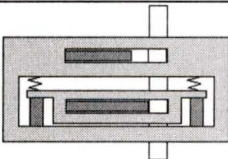
displacement. The design involved a cylindrical tube with an inside crawler. In 1984, Taniguchi [24] presented an actuator that used an outer cylindrical shell and an inner crawler. The inner crawler consisted of several cylindrical piezoceramic elements connected together. The firing sequence of the cylindrical piezoceramics was such that a “rippling” motion of extending and clamping made the inner body move. In 1986, Hara [25] modified the design of Bizzigotti and May by incorporating stacked piezoceramics to increase the actuation displacement. In 1986, Staufenberg [26] created an actuator capable of translational and rotational motion. Many piezoceramics were used in the design. Some were used to grip the shaft were others were used to push the shaft outward (translational motion), or to push the shaft sideways (rotational motion). In 1988, Fujimoto [27] filed a patent consisting of two similar inchworm actuators that use an inner crawler to creep inside a channel.

In 1990, Murata [28] used one set of piezoceramics to engage a shaft with an extremely small pitch. Once engaged, the shaft would be actuated by another set of piezoceramics. In 1991, Shibuta et al. [29] designed an actuator for precise pointing and vibration suppression for anticipated use on the Geostationary Platform planned by NASDA. In 1994, Rennex [30] used piezoceramics with flexure clamps to hold and actuate the inner shaft. In 1996, Pandell and Garcia [31] designed an actuator similar to the design of Galutva but having one extra stage for extension and clamping. In 1997, Galante [32] designed an actuator having an inner shaft that would move with respect to the outer casing. The inner shaft had one piezoceramic used for extension, where as the outer casing had two piezoceramics used for gripping. Firing the piezoceramics in a special sequence forced the inner shaft to move. In 1999, Canfield et al. [33] developed an actuator for minimally invasive surgery. The proposed mechanism consists of an inchworm that moves a set of jaws (machined from titanium by the wire EDM process). When the inchworm moves back and forth the jaws are force to clamp and unclamp. Also in 1999, Frank et al. [34] developed an inchworm for flow control.

Unfortunately, many of these designs rely on extremely high tolerances ($\sim 2.54\mu\text{m}$) with no method of adjustment. In the case of Frank et al. [34], for example, the clearance between output shaft and the gripping surface is less than $5\mu\text{m}$. This exceptionally high tolerance makes the actuator extremely delicate. Any tiny imperfections in machining results in significant loss of performance or prevent

actuator motion entirely. Furthermore, most of the inchworm actuators are patented ideas and there has not been an effort to study in detail the design to provide real proof-of-concept performance data. The only designs that have reported performance results are the actuators proposed by Pandell and Garcia with an output force of 13N and a static holding force of 44N with a maximum speed of 1mm/s. The gripping device proposed by Canfield et al. produced a block force of 44N and also a maximum speed of 1mm/s at a frequency of 100Hz.

Table 1-1 Inchworm actuator designs and patents reported in the published literature

			
Stibitz, 1964	McNancy, 1964	Hsu, 1966	Locher, 1967
			
Brisbane, 1968	Galutva, 1972	Bizzigotti et al., 1975	Sakitani, 1976
			
Ishikawa, 1979	O'Neill, 1980	Tanigushi, 1984	Hara, 1986
			
Staufenberg, 1986	Fujimoto, 1987	Murata, 1990	Shibuta et al., 1991
			
Rennex, 1994	Pandell and al., 1996	Galante, 1997	Canfield et al., 1999
			
Frank et al., 1999			

1.5. Added Value of the Research

Transportation plays a vital role in Canada's economy and our overall quality of life. However, by its very nature, transportation activity has impacts on the environment, ranging from air pollution, greenhouse gas emissions and water pollution to urban sprawl - all of which impact on our health and well being. Sustainable transportation can create viable, long-term economic and business opportunities. The development of fuel cells, new materials and design innovation technologies presents new, strategic growth opportunities in an increasingly competitive global economy.

The field of mechatronics is predicted to be one of the key-enabling technologies that will fuel industrial growth in the 21st century. Canada's two main competitors, Japan and USA, are extensively investigating multifunctional material technologies. The improved understanding of the behavior of innovative devices and how to enhance performance will be of direct use to the transportation industries. Given its multidisciplinary nature, covering materials science, actuator design and control, the research will produce results that will directly benefit the transportation and manufacturing sectors in Canada.

The research output provides basic and applied research data to support the development of innovative technologies, focusing on the use of multifunctional materials, through the expansion of knowledge in mechatronics. This thesis proposes a new technology of high force inchworm actuators suitable for brakes that has been validated in laboratory tests.

1.6. Electromechanical Materials

A dielectric is a material in which a polarization occurs when it is placed in an electric field. All dielectrics are electrostrictive, meaning they increase in length and decrease in diameter when subject to a longitudinal electric field. The induced strain is proportional to the square of the applied field [35].

Some dielectrics are piezoelectric, which means when subject to an applied electric field they have different strains along crystallographic polar directions. Hence they can only occur in substances which have no center of symmetry (like quartz). The strain is greater than the electrostrictive strain (which is also present) and is directly

proportional to the applied field and has no hysteresis with the reversal of the field direction [35].

Some piezoelectrics are ferroelectric. These piezoelectrics have a spontaneous polarization caused by the formation of small electric dipoles upon cooling through a Curie temperature. The dipoles can be aligned by an applied field, which gives a much greater piezoelectric strain, compared to regular piezoelectrics [35]. The other criterion for a ferroelectric is that the direction of polarization can be reversed by a sufficiently strong reversed electric field as shown in Figure 1-1.

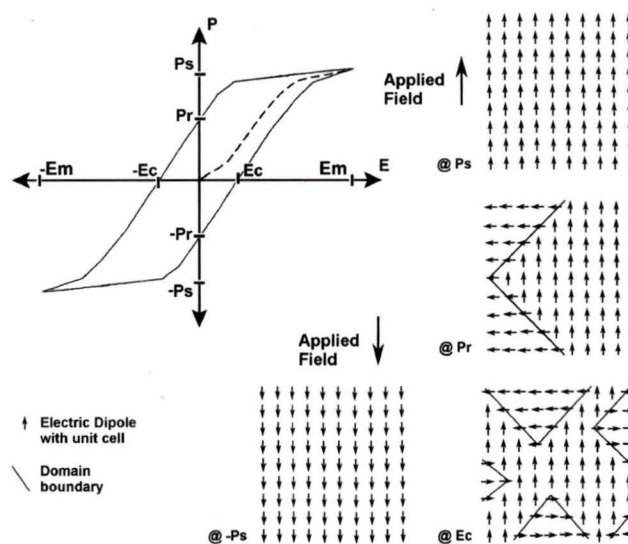


Figure 1-1 Ferroelectric hysteresis loop generated by a cyclic electric field

In Figure 1-1, an electric field is applied until all the dipoles are aligned in one direction. When this occurs the ferroelectric is said to have reached its saturation polarization (P_s). At this value, the maximum displacement (due to tension) is also reached. When the electric field is removed, the crystal does not revert back to its random orientation of dipoles but exhibits a remnant polarization (P_r). In fact, an opposite electric field of magnitude $-E_c$ is needed for the crystal to achieve no net polarization. This field is called the coercive field. By applying a field of $-E_m$, the ferroelectric completely re-orientates itself in a direction opposite to that obtained at E_m . At this value the maximum displacement (due to compression) is reached. By re-applying an electric field of E_m , the crystal will undergo one complete hysteresis loop.

Some ferroelectrics have a very gradual transition at the Curie temperature. This means the polarization is not spontaneous and builds up slowly on successive cooling. These are called relaxor ferroelectrics. Some of them (like PMN) exhibit even greater voltage induced strains compared to piezoelectrics, and thus are being investigated for actuator applications. The strain is related to the square of the applied field, so the effect is electrostrictive, rather than piezoelectric [35].

The Piezoelectric Effect

The piezoelectric effect is the ability of a crystal to exhibit electric polarity when subject to a mechanical stress. The inverse piezoelectric effect is the ability of a crystal to deform when subjected to an electric field. Both effects are linear. If the crystal is connected to a circuit a tension will generate current in one direction whereas a compression will generate current in the reverse direction [36]. When an electric field is applied to a piezoelectric crystal, it expands. Conversely, when the field is reversed, the crystal contracts. The inverse piezoelectric effect is useful in actuator applications [36]. The governing equation for the inverse piezoelectric effect (along the “3” axes direction) is presented in Equation 1-1 [37].

$$e_3 = d_{33}E_3 \quad (1-1)$$

where,

e_3 = Material strain

d_{33} = Piezoelectric charge coefficient

E_3 = Electric field

The electric and mechanical coupling of piezoelectrics is very useful, but ferroelectric piezoelectrics, such as PZT, exhibit hysteresis as shown in Figure 1-2.

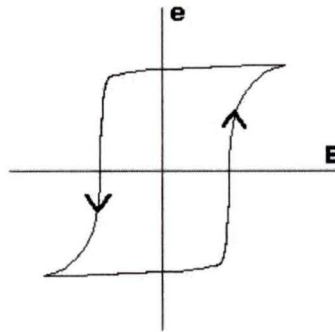


Figure 1-2 Strain vs. electric field plot for a ferroelectric piezoelectric (PZT)

The commercial piezoelectric material, BM500, is made from a PZT composition. Some properties of this material are presented in Table 1.2

Table 1-2 Properties of piezoelectric material BM500

Property	BM500	Reference
Density	7650 Kg/m ³	[38]
Frequency range	< 30 kHz	[38]
Maximum strain	0.06%	[38]
Hysteresis	15 to 20%	[38]
Piezoelectric charge coefficient (d ₃₃)	365 pC/N	[38]
Poisson's ratio	0.44	[39]
Coefficient of thermal expansion	~3 E-6/C	[40]
Young's modulus	5.3E10 N/m ²	[38]

The Electrostriction Effect

The electrostriction effect, which results from the lack of polar properties in centrosymmetric crystals, is the ability of a crystal to produce a strain regardless of the direction of the electric field. Moreover, the strain is proportional to the square of the applied field. When a dielectric (with or without a center of symmetry) is subjected to an electric field, the dipoles align themselves into the direction of the field to minimize energy [37]. A strain vs. electric field plot for a typical electrostrictive material is shown in Figure 1-3.

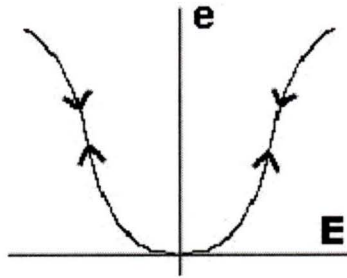


Figure 1-3 Strain vs. electric field for an electrostrictive (PMN)

Consequently, electrostrictive strains depend only on the field's magnitude regardless of field's polarity. Electrostrictive (PMN) materials are governed by Equation 1-2 [37].

$$e_3 = M_{33}E_3^2 \quad (1-2)$$

where,

e_3 = Material strain

M_{33} = Electrostrictive charge coefficient

E_3 = Electric field

Fortunately, electrostrictive materials exhibit negligible hysteresis at high fields [38]. The electrostrictive material, BM600, is made from a PMN composition. The material properties are presented in Table 1-3.

Table 1-3 Properties of electrostrictive material BM600

Property	BM600	Reference
Density	7800 Kg/m ³	[38]
Frequency range	< 1 kHz	[38]
Maximum strain	0.1%	[38]
Hysteresis	1 to 4%	[38]
Equivalent piezoelectric charge coefficient (d33)	500 to 1800 pC/N	[38]
Poisson's ratio	0.45	[39]
Coefficient of thermal expansion	~1 E-6/C	[41]
Young's modulus	1.0E11 N/m ²	[38]

1.7. Piezoceramic Stacks

The amount of strain produced in a piezoceramic (piezoelectric or electrostrictive material) is dependent on the thickness of the element and the magnitude of the voltage applied across the thickness. To increase the amount of displacement, many thin piezoceramic elements can be stacked on top of each other. In this stack arrangement, the total stack displacement is equal to the number of elements multiplied by the displacement of each element as shown in Equation 1-3 [42].

$$\delta_3 = d_{33} E_3 t n \quad (1-3)$$

where,

δ_3 = Zero load deflection

d_{33} = Piezoelectric charge coefficient

E = Electric field

t = Thickness of each stack wafer

n = Number of wafers

Construction of a stack is achieved by gluing many “wafers” of active material on top of one other. Before the wafers are ready for stack assembly, they must be individually fired, silvered, and poled [43]. The wafers must be protected from excessively high temperatures that will cause the active material to de-pole (lose their dipole properties) [43].

The stacks are then encased in a protective wrapping. Lead wires protrude from the encasing for electrical connection. Metal washers are placed at each end to evenly distribute the load to the brittle ceramic. Loads must be compressive and perfectly centered to not damage the stacks [43,44].

1.8. Proposed Inchworm Actuator

This research and development of an electrostrictive inchworm actuator was funded by Sensor Technology Limited. The specifications, as set forth by the supporting company are as follows:

- Actuator stroke greater than 15mm
- Supplied voltage less than 200V
- Actuator pushing force greater than 20N

The actuation materials envisaged for application as the stack elements of the inchworm actuator were piezoelectric BM500 (PZT) and electrostrictive BM600 (PMN). The final design incorporates the electrostrictive material due to its superior displacement characteristics.

The finite element software Ansys was used to model the actuator and project the optimal combination of design parameters. Because Ansys is capable of analyzing piezoelectric materials, but not electrostrictive materials, the Ansys model was designed having a piezoelectric stack with an “equivalent” d_{33} piezoelectric constant. This piezoelectric constant was calculated to give the identical displacement of the true electrostrictive stack. This technique is further discussed in Chapter 2.

Here, a new inchworm actuator design is presented. An inner crawler is assembled from three electrostrictive stacks and two flextensional frames all held together by a threaded rod with locking nuts as shown in Figure 1-4.

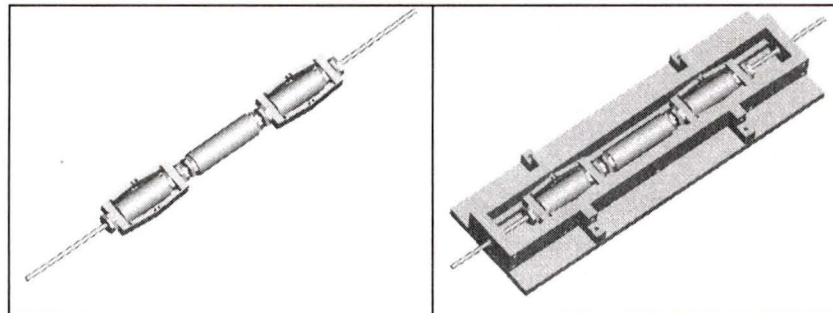


Figure 1-4 Proposed electrostrictive inchworm actuator

When one of the brake stacks is energized, it expands longitudinally causing the surrounding flextensional frame to distort reducing its width. When the center stack is energized, the threaded rod is stretched and distance between the flextensional frames is increased. By energizing each of the stacks in a particular sequence, motion is thus created. Consider the actuator in a vertical position. First, the top brake stack is energized, releasing the grip of the top flextensional frame from the wall of the casing. Next, the center stack is energized to move the entire top assembly upwards. The top brake stack is then de-energized and the flextensional frame comes back into contact with the casing. The bottom brake stack is now energized releasing the grip of the bottom flextensional frame. The center stack, now de-energized, moves the bottom assembly up. The bottom stack is then de-energized, so the bottom flextensional frame once again grips the casing wall. By rapid cycling of this sequence, motion is created.

The actuator was designed to maintain a locked position when no electrical energy is supplied. Additionally, the design was made to have a high degree of adjustability through the use of adjustment nuts.

1.9. Thesis Layout

This thesis is organized in five chapters. Chapter 1 presented the background and motivation to carry out this research as well as a thorough investigation of existing literature on actuators to identify the designs already created. Chapter 2 investigates three possible design alternatives for the brake assembly component. A parametric study using the finite element method is carried to identify the optimal combination of design parameters for the selected design. In Chapter 3, the design and manufacturing of the prototype based on the model is performed to prove the concept and a controller is developed to drive the inchworm mechanism. In Chapter 4, applications of the developed actuator are demonstrated using adaptive truss structures with the goal of maximizing structural strength using the variable geometry truss concept. Chapter 5 discusses the conclusions and setbacks, and delineates recommendations for possible future work.

ACTUATOR DESIGN AND MODELING

This chapter presents the design and modeling aspects of the proposed inchworm actuator. The actuator performance objectives and material selection are discussed, followed by a conceptual design for the brake assembly component. A parametric finite element analysis is carried out to select the best design. The parametric study has enabled the selection of the design dimensions to achieve acceptable performance in all aspects of the design.

2.1. Actuator Specifications

The goal of the actuator is to meet the performance specifications set by Sensor Technology Limited [43] and these are presented in Table 2-1.

Table 2-1 Actuator design specifications

Actuator Specifications	
Minimum Displacement (mm)	15
Minimum Force Output (N)	20
Maximum Operating Voltage (V)	200

2.2. Material Selection

The material for the flextensional frame was chosen to have a coefficient of thermal expansion similar to that of the electrostrictive stack to minimize the thermal effect. However, the present research does not involve an investigation of the influence of thermal variations on the actuator performance. The flextensional frame material selection criterion was to reduce any temperature dependant dimensional variation between the stack and the surrounding material. The metals that were investigated are presented in Table 2-2 [40].

Table 2-2 Thermal expansion and elastic properties for various metals

Metal Possibilities	Coefficient of thermal expansion ($1 \times 10^{-6}/\text{C}$)	Young's Modulus (GPa)
Aluminum 3003	24.0	69.0
Steel (oil hardened)	11.7	200.0
Stainless Steel 304	17.3	193.1
Brass (65% Cu, 35% Zn)	20.0	100.0
Titanium (6% Al, 4% V)	9.5	114.0

The metals chosen must have a high Young's modulus to efficiently transfer the stack force to the brake pads, and a coefficient of thermal expansion similar to the selected actuator stack material. As shown in Table 2-2, the materials with the highest Young's modulus are oil hardened tool steel, stainless steel 304, and titanium (6% Al, 4%V). The titanium was chosen, however, because it is the closest match to the coefficient of thermal expansion of the piezoceramic ($\sim 1 \times 10^{-6}/\text{C}$) [41]. Moreover, titanium (6%Al, 4%V) has a high strength to weight ratio (density = 4730Kg/m^3), which makes it advantageous for space applications, an area of interest to Sensor Technology Limited.

The material for the outer casing was originally chosen to be made from titanium to match the flextensional frame material. However, due to the high cost of machining a prototype at the preliminary design stage, it was decided that the outer casing would be made from oil hardened tool steel.

2.3. Conceptual Design

The inchworm actuator concept uses small incremental steps to attain large displacements. This motion is achieved by a mechanism that "crawls" inside an outer casing. The walking mechanism consists of two brake assemblies separated by a center electrostrictive stack. Each brake assembly is forced to clamp and unclamp in a particular sequence to capture the displacement of the center stack. Consequently, the brake assemblies are the most critical aspect of the actuator design.

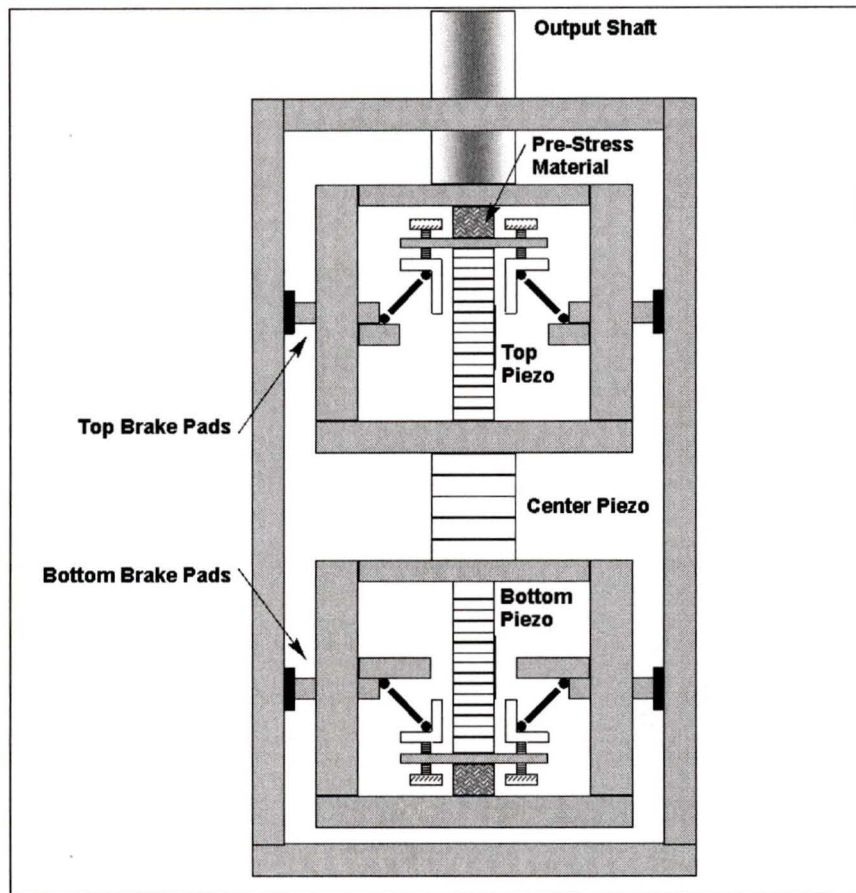


Figure 2-1 Conceptual inchworm actuator design model original design

The first proposed configuration for the actuator is presented in Figure 2-1. Firing each stack in a predetermined sequence creates the actuator motion. First, the top piezo stack is energized. This action compresses the pre-stress material and forces the diagonal arms connected to the brake pads to move up and in; this action releases the top brake pads. Next, the center stack is actuated, pushing the top brake assembly upward. Afterward, the top stack is de-energized, forcing the top brake pads to grip the outer casing. The bottom stack is then fired, releasing the bottom pads. Subsequently, the center stack is de-energized, moving the bottom brake assembly up. Finally, the bottom stack is de-energized, forcing the bottom pads to grip the outer casing and capture the displacement. This sequence is repeated in rapid succession emulating the movement of an inchworm.

Conceptually this design works, but it has a large number of parts thus making the machining and matching of the various pieces quite complicated in the presence of such small tolerances ($\sim 2.54\mu\text{m}$). The large number of parts also makes the actuator

expensive and difficult to manufacture. Another problem is the stack pre-stressing. Electrostrictive stacks are generally weak in tension and should therefore always operate in compression [43]. In fact, it is recommended that tensile loads should not exceed 80% of the initial compressive pre-stress [41]. Unfortunately, this design does not include a pre-stress for the center stack and thus does not ensure that it will always remain in compression. Conceptually this actuator works, but simplifications and additional pre-stressing need to be added.

The second design iteration was aimed at reducing the number of parts in the brake assemblies. To achieve this, the idea of using one solid piece of material to surround each brake stack was investigated. When the piezoceramic stack is energized the surrounding material (flextensional frame) is forced to flex and change its radial dimension. To find the best shape of the flextensional frame, three flexure orientations were investigated. Using finite element analysis, a unit force was given to each model in Figure 2-2 and the displacement of the top right corner was recorded.

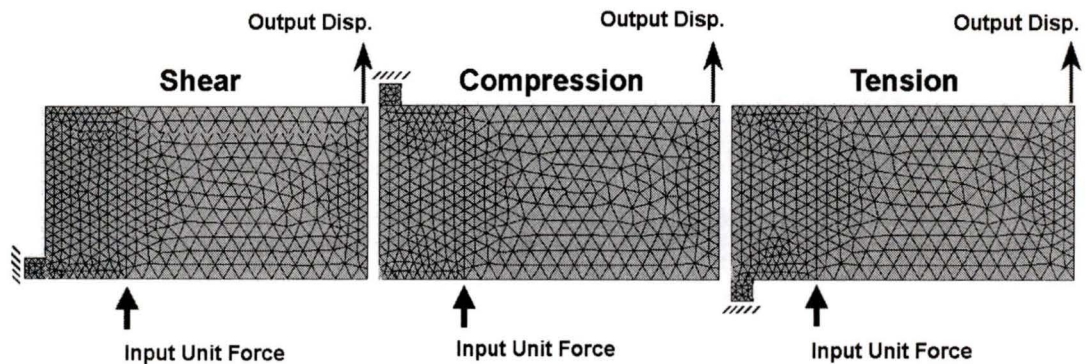


Figure 2-2 Different flexure orientations

The shear model produced a displacement of 1.000mm, the compression model produced a displacement of 0.792mm, and the tension model produced a displacement of 0.789mm. Since the shear model proved to be the most efficient, a frame shape that used a shear bending orientation was found to be the most suitable.

The flextensional frames are designed to have an interference fit with the outer casing. When the brake stacks are energized, the frames are forced to distort and reduce in width. This action frees the flextensional frames and allows them to move freely

within the outer casing. When the stacks are de-energized, the frames grip the outer casing locking the actuator in place.

The advantage of this design is that it has very few parts and allows the actuator to maintain a locked position when no electrical power is supplied. Unfortunately, it does not allow for fine adjustments. Any slight misalignment or tolerance inconsistency may prevent the brake assembly from freeing itself from the outer casing. It was therefore decided that further improvements could still be made to the design.

The third iteration design incorporates adjustment nuts to facilitate changes in the design parameters. Circular notches are integrated into the flextensional frames to target bending at specific locations as shown in Figure 2-3.

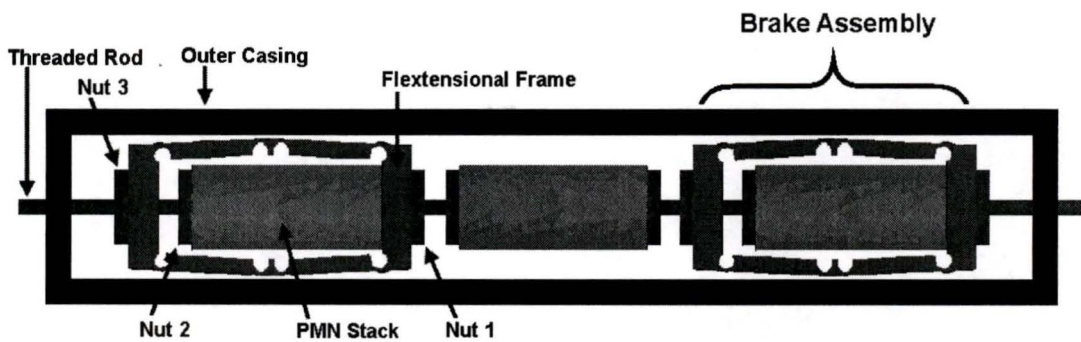


Figure 2-3 Selected conceptual design

Additionally, a rod with adjusting nuts has been inserted through the center of the actuator. In this design, each brake assembly incorporates two pre-stressing adjustments: one for the stack and one for the frame. When adjustment nuts 1 and 2 are tightened, the stack is pre-stressed. This ensures the stacks always remain in compression. When adjustment nuts 1 and 3 are tightened, the frame is pre-stressed. Pre-stressing the frame allows a fine width adjustment within the outer casing.

The actuator sequence is illustrated in Figure 2-4.

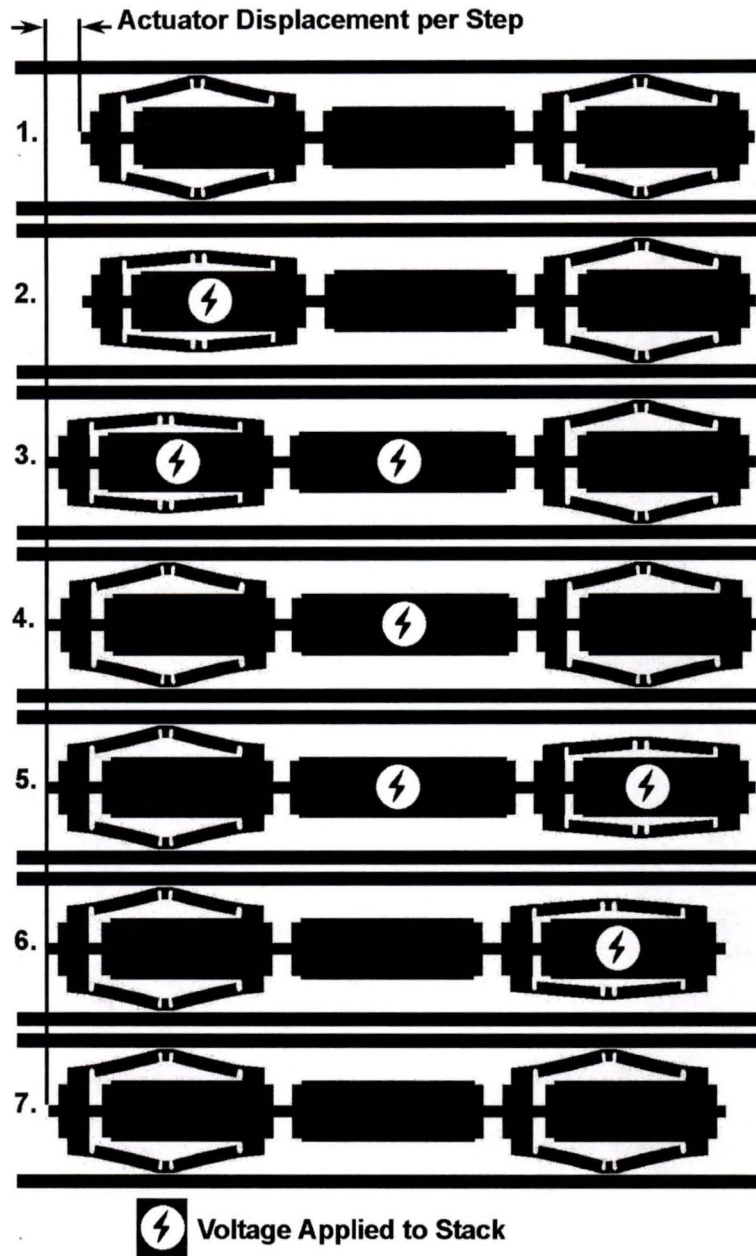


Figure 2-4 Inchworm actuator stack actuation sequence

2.4. Finite Element Modeling

The actuator design has been modeled using the finite element software Ansys. To reduce complexity, the actuator has been modeled in parts. The modeling of the piezoelectric/electrostrictive stack and the brake assembly are presented next.

Piezoelectric/Electrostrictive Stack Modeling

The stack was created in Ansys using the 10-node tetrahedral SOLID98 element type. This element is defined by ten nodes with up to six degrees of freedom at each node as shown in Figure 2-5.

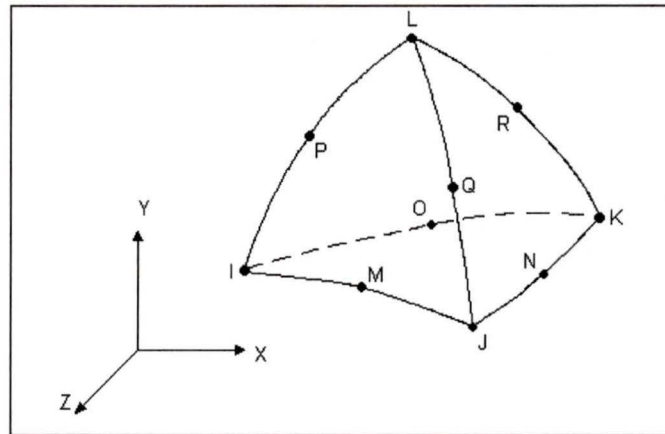


Figure 2-5 SOLID98 tetrahedral coupled-field solid

The degrees of freedom include three-dimensional magnetic, thermal, electric, piezoelectric, and structural field capabilities. This element type is particularly well suited for coupled structural and piezoelectric applications.

The stack to be modeled is assembled from wafers of piezoelectric material each having a thickness of 0.508mm (0.02in) with an outer diameter of 25.4mm (1in) and an inner diameter of 6.35mm (0.25in). The stack contains 100 wafers glued together to achieve a total height of 57.15mm.

Due to symmetry only one-quarter of the stack is modeled in Ansys as shown in Figure 2-6.

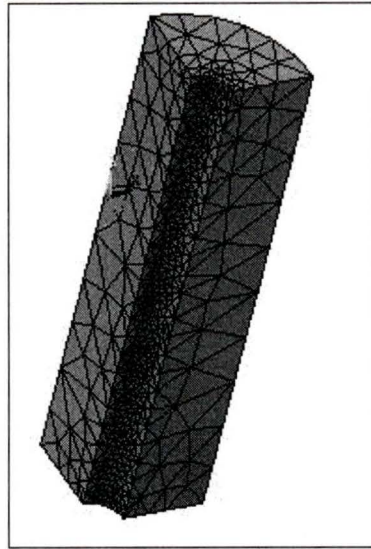


Figure 2-6 Ansys model of stack

The stack model contains 5,978 nodes, 3,645 elements and has 22,488 active degrees of freedom. The choices of material for the stack were piezoelectric material BM500 (PZT) and electrostrictive material BM600 (PMN) both supplied by Sensor Technology Limited [42].

Consider first a stack made from the piezoelectric material BM500. This material is characterized with a $d_{33} = 365 \text{ pC/N}$ [38]. When one end of the Ansys model was fixed and 200V was applied across each wafer, the stack elongated a free displacement of $7.2 \mu\text{m}$.

Assume now a stack with identical dimensions but made from the electrostrictive material BM600. Ultimately, the free displacement of this stack is desired. However, Ansys does not currently have an element type capable of calculating electrostrictive displacements. To overcome this, the electrostrictive stack was modeled as a piezoelectric stack with an “equivalent” d_{33} constant. This constant was calculated by rearranging Equation 1-1 for d_{33} and using the strain vs. electric field graph for PMN BM600 shown in Figure 2-7 [38].

$$d_{33} = \frac{e_3}{E_3} \quad (2-1)$$

where,

e_3 = Material strain

d_{33} = Piezoelectric constant

E_3 = Electric field

The graph of %strain vs. electric field for PMN BM600 is shown below.

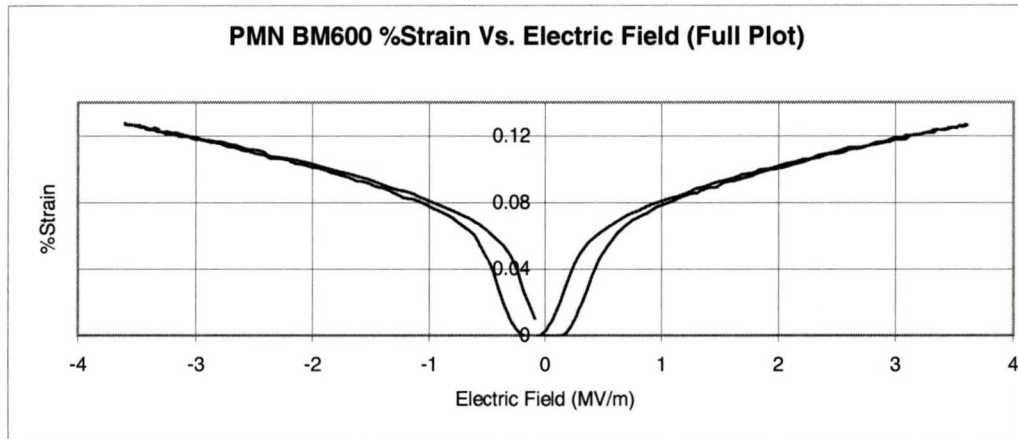


Figure 2-7 Graph of %strain vs. electric field for BM600

Since we are primarily interested in electric fields between $0 \leq E \leq 1.25$, the graph of the upper hysteresis curve in this region is shown in Figure 2-8.

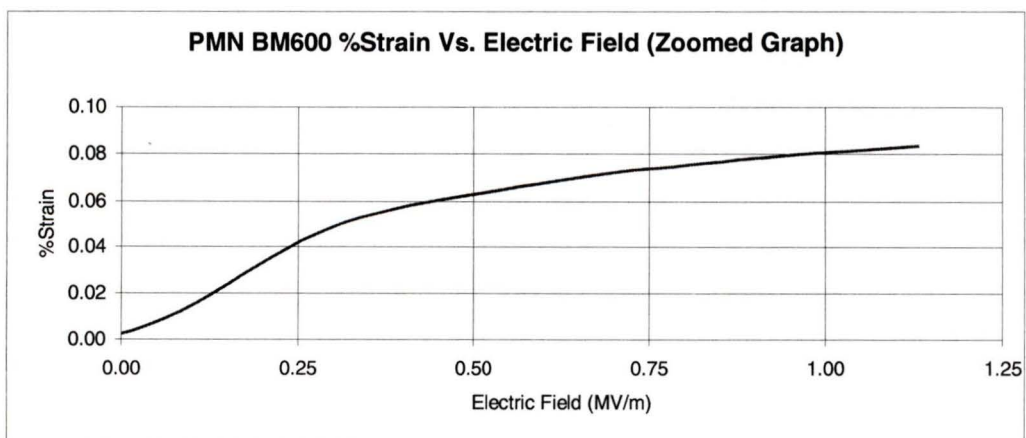


Figure 2-8 Graph of %strain vs. electric field for BM600 (zoom)

Using the manufacturer's suggested voltage of 200V with a stack wafer thickness of 0.508mm (0.02in), the electrostrictive material yields an electric field of 0.3937MV/m. Figure 2-8 shows the corresponding strain is 0.0567% (or 2.88×10^{-5} mm per stack element). Using these values, the calculated d_{33} is equal to $0.000567/0.3937 \times 10^6 = 1440 \text{pC/N}$. It is important to understand that the "equivalent" d_{33} value changes for every different value of applied voltage or wafer thickness.

Consider now an electrostrictive stack with identical dimensions as the previously mentioned piezoelectric stack. Fixing one end and applying 200V across each wafer, the stack model displaced a free displacement of 30.0 μm . The results obtained by the Ansys model and calculated theoretically are shown in Table 2-3.

Table 2-3 Comparison of free displacement of BM500 and BM600

	BM500 (PZT)		BM600 (PMN)	
	Ansys	Theoretical	Ansys	Theoretical
Free Displacement (μm)	7.2	7.3	30.0	28.8

Comparing the performance of the two piezoceramics it is apparent that BM600 (PMN) gives significantly more free displacement than BM500 (PZT). BM600 (PMN) has therefore been chosen as the actuation material.

The above discussion has been based on the stack used in the brake assembly. The extending stack of the inchworm has 133 layers (0.381mm each) and a total height of 3in. This stack provides a displacement of 39.9 μm when subjected to 200V.

Brake Assembly Modeling

The brake assembly that was modeled is presented in Figure 2-9, where the black lines indicate the outline of the flextensional frame.

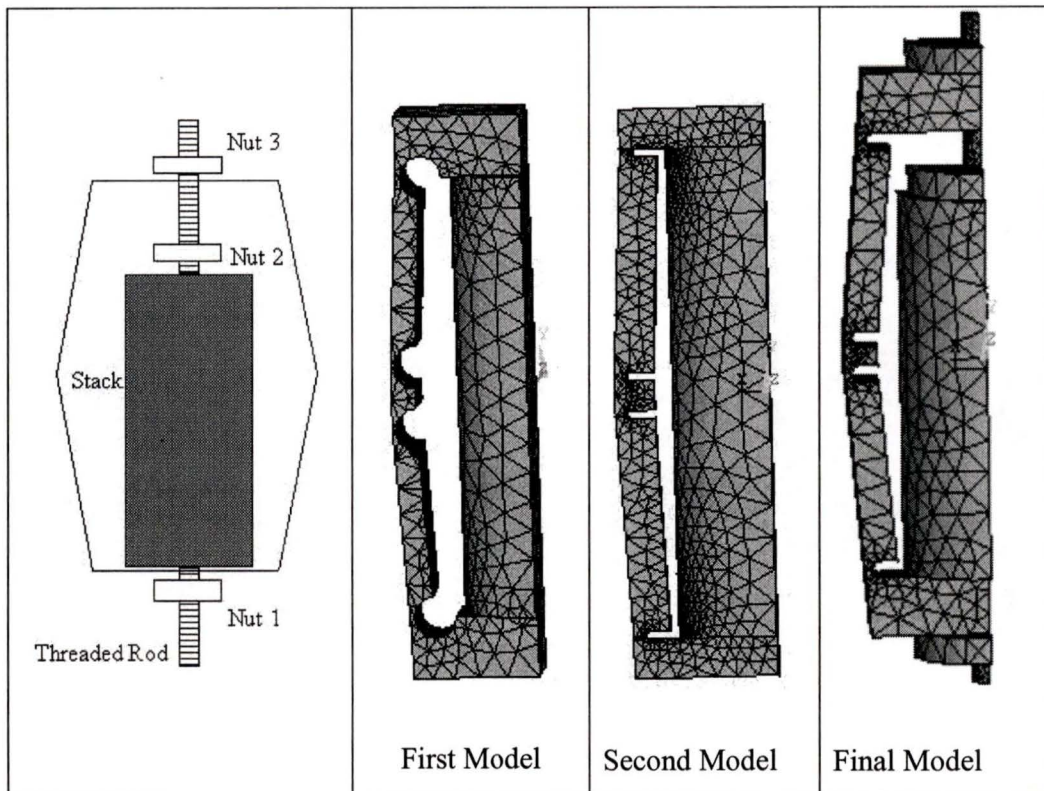


Figure 2-9 Finite element model for the flextensional frame and stack with nuts

The flextensional frame was created using the SOLID92 element primarily because it is well suited with the stack element type (SOLID98), which is also defined by ten nodes along its boundary [45]. The SOLID92 element type has x, y, and z degrees of freedom and is best used for structural applications. It is equipped with a quadratic displacement behaviour and used especially to model irregular meshes. This makes it possible to accurately model the bending notches in the frame.

Using this element, the first model of the brake assembly was created. This first model did not include the adjustment nuts. Only the flextensional frame and PMN stack were considered. The objective was to maximize the brake pad displacement. Based on this model, a rough aluminum prototype was machined [46]. Upon testing, a trade off was discovered between the pad displacement and the brake pad blocked force. One could not be increased without the other being decreased. Since this model had a high brake pad movement, the resulting blocked force was very small. It soon became apparent that this design could not deliver the necessary brake pad force needed for proper operation of the actuator.

To increase the blocked force, a new design was investigated. This was accomplished by increasing the thickness of the arms and at the notches, and changing the shape of the notches to long thin slots. Making these changes, the second model and an aluminum prototype [46] were created.

This design accomplished its goal of increasing the blocked force; however during testing, an inconsistency between the model and the prototype became apparent. The simplified model assumes the top end of the stack is rigidly connected with the inside upper surface of the frame. During actuation, this assumption falsely strengthens the upper section of the frame.

The final model was developed to include the adjustment nuts. This model is an accurate representation of the brake assembly and contains 12,455 nodes, 6,512 elements and has 38,063 active degrees of freedom. With the model fully developed, the brake assembly dimensions are scrutinized in great detail as presented in the next section.

2.5. Brake Assembly Design Optimization

The dimensions were broken down into two categories: the fixed dimensions and the free dimensions.

Fixed Dimensions

The fixed dimensions were set due to the size and shape of the PMN stacks quoted by Sensor Technology Limited. These stacks have an outer diameter of 25.4mm (1in), an inner diameter of 6.35mm (0.25in), and height of 57.15mm (2.25in). The resulting fixed dimensions are shown in Figure 2-10.

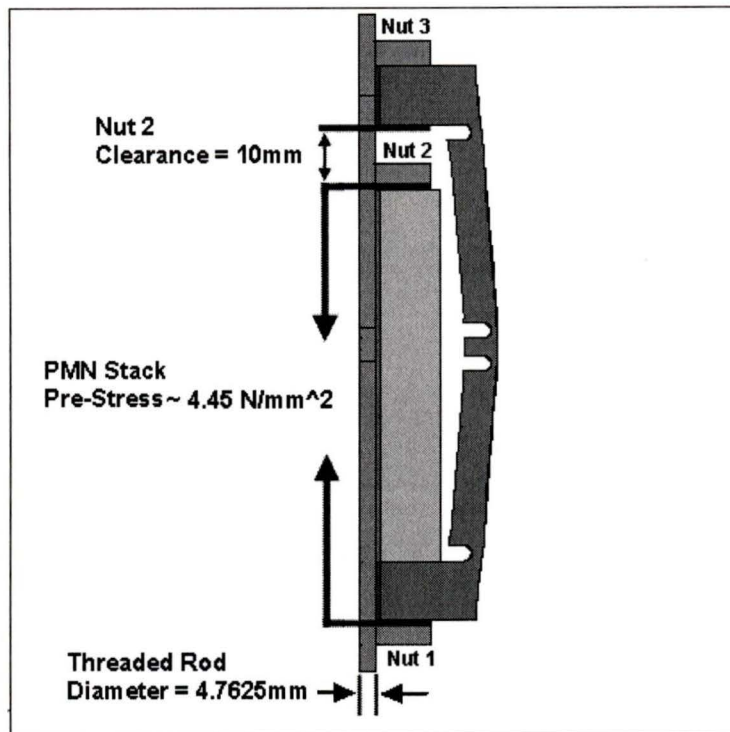


Figure 2-10 Actuator design dimensions

The minimum clearance required to adjust Nut 2 was 10mm [47], therefore, 10mm was chosen for this dimension. The pre-stress on the PMN stack was chosen to be 4.45N/mm^2 [43] as this is significantly lower than 40N/mm^2 , which is the maximum compressive loading for typical piezoceramic stacks [41]. The last fixed dimension was the threaded rod diameter. It was chosen to be 4.7625mm (0.1875in) since it was the next nominal size smaller than the PMN stack hole of 6.35mm (0.25in).

Free Dimensions

The free dimensions are presented in Figure 2-11.

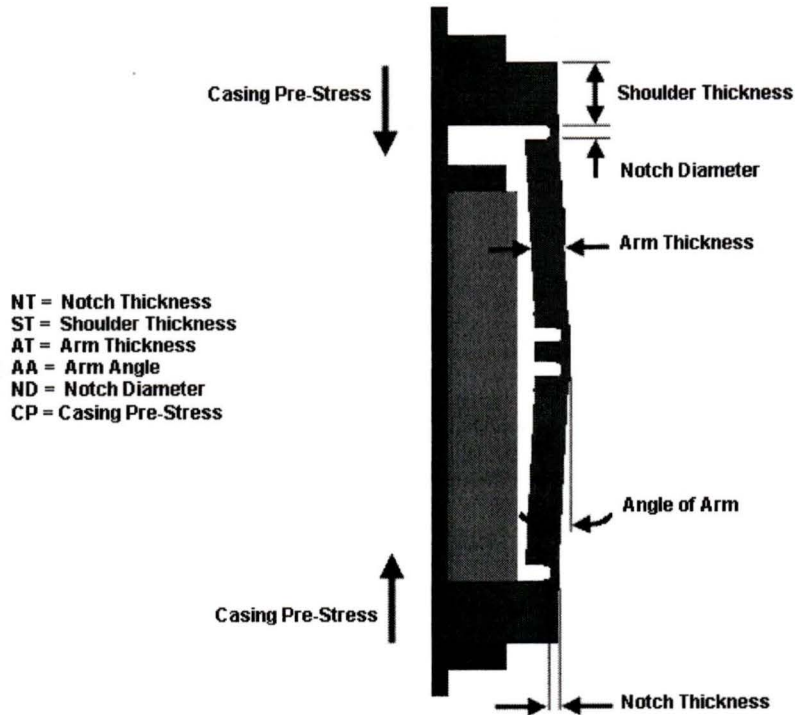


Figure 2-11 Brake assembly free dimensions

The dimensions having the greatest impact on the design were selected first. The order in which the dimensions were examined is presented below.

1. Notch Thickness (NT) in millimeters
2. Shoulder Thickness (ST) in millimeters
3. Arm Thickness (AT) in millimeters
4. Arm Angle (AA) in degrees
5. Notch Diameter (ND) in millimeters
6. Casing Pre-Stress (CP) in Newtons

2.6. Performance Criteria

To assist in the selection of the free dimensions, three performance criteria were defined: the range, the block force and the fatigue safety factor, as outlined below:

The Range

Referring to Figure 2-12, when adjustment Nut 3 is tightened, the flextensional frame bows outward and the brake pad moves out to position “A”. Now energizing the PMN stack forces the threaded rod to lengthen allowing the flextensional frame to move inward to position “B”. The distance between brake pad locations “A” and “B” is defined as the “Range”. The range is important because it is a measure of the brake pad movement during actuation. Too small a range may not allow the brake pad to free itself from the outer casing.

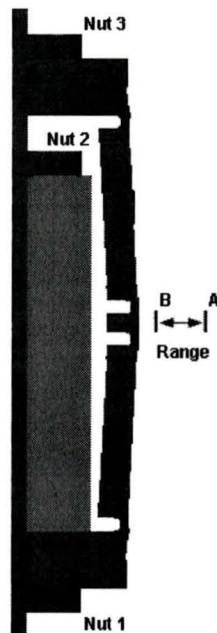


Figure 2-12 Brake assembly range

The Blocked Force

For the brake pad to come in and out of contact, the outer casing must be located somewhere between the maximum and minimum brake pad lateral displacements. To ensure the brake pads release from the outer casing during actuation there should be a clearance. The minimum suggested clearance is $25.4\mu\text{m}$ (0.001in). To make certain the pad release, the design aims for a clearance between $25.4\mu\text{m}$ (0.001in) and

50.8 μm (0.002in). For the brake pad to come in and out of contact, the outer casing (“C”) must be located somewhere between “A” and “B”, as shown in Figure 2-13.

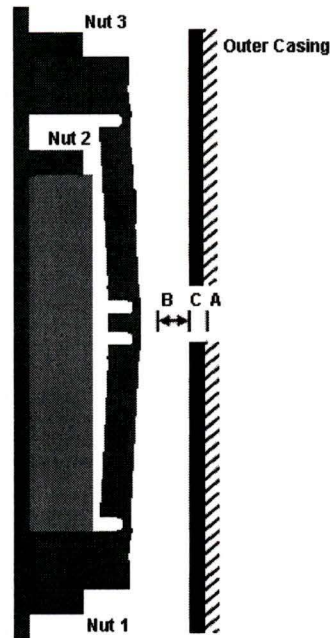


Figure 2-13 Brake assembly in contact with outer casing

Suppose the PMN stack was energized, and the location of the outer casing “C” was positioned at “B”. The brake pad and the outer casing would be in contact but without force. If the PMN stack was now de-energized, the flextensional frame would try to flex back to position “A” but would be stopped by the outer casing. The normal force exerted on the outer casing is coined the “zero clearance blocked force”.

To ensure the brake pads release from the outer casing during actuation there should be a clearance between “B” and “C”. The minimum suggested clearance is 25.4 μm (0.001in) [47]. To make certain the pad releases, the design aims for a clearance between 25.4 μm (0.001in) and 50.8 μm (0.002in).

The Fatigue Safety Factor

The operation of this actuator requires the flextensional frame to bend back and forth a high number of cycles. Each cycle induces a fluctuating stress, which over time may result in the possibility of fatigue failure. To safeguard against this, a fatigue analysis

was performed for each potential design. Using the modified Goodman relation [39], along with the surface roughness taken as machined, the allowable stress amplitude was calculated for each design. Subsequently, the actual stress amplitude was also determined for each design. Dividing the allowable stress amplitude by the actual stress amplitude gives the fatigue safety factor. Investigating the possible locations for fatigue failure it was determined that the most critical location was at the center notches.

The operation of this actuator requires the flextensional frame to bend back and forth a high number of cycles. Each cycle induces a fluctuating stress, which over time may result in a failure due to fatigue. To safeguard against this, the maximum and minimum Von Mises stresses (derived from distortional energy theory [48]) were analyzed. Using these upper and lower limits of stress, a fatigue analysis was performed for each potential design.

The modified Goodman relation in Equation 2-2 [39] is rearrange for σ_a and presented in Equation 2-3.

$$\frac{\sigma_a}{S_e} + \frac{\sigma_m}{S_{ut}} = 1 \quad (2-2)$$

where,

σ_a = Stress amplitude

S_e = Endurance limit

σ_m = Mean stress

S_{ut} = Ultimate stress

$$\sigma_a = S_e * \left(1 - \frac{\sigma_m}{S_{ut}}\right) \quad (2-3)$$

For each potential design the minimum (σ_{\min}) and maximum (σ_{\max}) stresses were evaluated using the Ansys finite element software. The mean stress (σ_m) was then calculated using Equation 2-4 [39].

$$\sigma_m = \frac{(\sigma_{\max} + \sigma_{\min})}{2} \quad (2-4)$$

Using this value of mean stress (σ_m) in Equation 2-4 with the endurance limit of machined titanium ($S_e = 279\text{MPa}$ [49], [50]) and the ultimate strength of titanium ($S_{ut} = 900\text{MPa}$ [39]) yields the maximum allowable stress amplitude ($\sigma_a = \sigma_{allow}$). Now, using the minimum (σ_{\min}) and maximum (σ_{\max}) stresses calculated by Ansys the actual stress amplitude (σ_{act}) is determined by Equation 2-5.

$$\sigma_{act} = \frac{\sigma_{\max} - \sigma_{\min}}{2} \quad (2-5)$$

Finally the “Fatigue Safety Factor” is calculated by dividing the allowable stress amplitude by the actual stress amplitude as shown in Equation 2-6 [51].

$$S.F. = \frac{\sigma_{allow}}{\sigma_{act}} \quad (2-6)$$

Investigating all the possible locations for fatigue failure it was determined through analysis that the most critical location was at the center notches of the flextensional frame. Therefore, all subsequent discussions of fatigue failure are focused on this aspect of the design.

2.7. Parametric Analysis

Notch Thickness (NT)

The first and most sensitive dimension that was studied was the notch thickness. To study the notch thickness all dimensions were fixed (to an initial guess at the best design) while only the notch thickness was varied. The notch thickness was varied from 0.75mm to 2mm as shown in Figure 2-16.

The design goal of the brake assembly aims for a range of not less than $90\mu\text{m}$, a blocked force of over 15N (on each brake pad), and a fatigue safety factor greater than 2.5. A range of $90\mu\text{m}$ should provide adequate adjustment should there be any slight tolerance inconsistency when the design is prototyped. A minimum force of 15N on each brake pad will generate a 30N normal force on the outer casing. This force multiplied by the coefficient of friction for the outer casing material ($\mu_{\text{steel on Ti}} = 0.69$ [52]) will lead to a acceptable actuator pushing force of 20.7N. A fatigue factor of safety over 2.5 will safeguard against the high number of cycles the design must endure over its lifetime. One last design goal aims to reduce the weight and length of the actuator.

Keeping these considerations in mind, the expected clearance is anticipated to be between $25.4\mu\text{m}$ (0.01") and $50.8\mu\text{m}$ (0.02") [47]. Choosing a notch thickness of 1.00mm gives acceptable values for the range, the blocked force, and the fatigue safety factor.

Shoulder Thickness

The next dimension that was considered was the shoulder thickness. Again, all the dimensions were fixed except the shoulder thickness which was varied from 5mm to 10mm as shown in Figure 2-17.

Increasing the shoulder thickness favorably increases both the range and the blocked force; unfortunately, the weight, and the actuator length also increase. A tradeoff between these parameters was met by selecting a shoulder thickness of 9mm.

Arm Thickness

The thickness of the arms was examined next. The arm thickness was varied from 4mm to 8mm as shown in Figure 2-18. Increasing the thickness of the arms increases range and blocked force, but decreases the fatigue safety factor. A compromise between these variables was chosen by selecting the arm thickness to be 5mm.

Arm Angle

The next free variable that was studied was the arm angle. The angle was varied from 1.19° to 9.42° as shown in Figure 2-19.

Interestingly, as the angle of the arm increases past 3.49° , the range begins to decline. Analyzing, the points before and after $AA=3.49^\circ$ shows the arms undergo a “snap through” condition. This means for angles of AA less than 3.49° ($AA < 3.49^\circ$) the arms are concave where as at angles above 3.49° ($AA > 3.49^\circ$) the arms are convex. Multiplying the true displacement by 75 and plotting the deformation for angles at $AA=3.03^\circ$ (Before Snap Through) and for $AA=3.95^\circ$ (After Snap Through) can be seen in Figure 2-14.

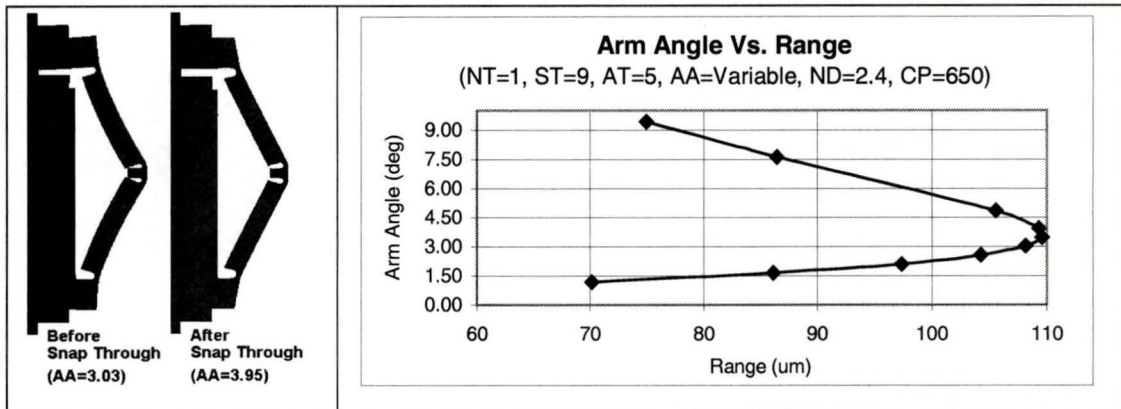


Figure 2-14 Arm deformation before and after snap through

If the arm angle was chosen to be 3.49° the range would be at its maximum of $109\mu\text{m}$ with the a resulting blocked force of 28N (clearance= 50.8N) and the fatigue safety factor of 2.9 . However, if the arm angle was chosen to be 4.87° the range would be decreased slightly to $106\mu\text{m}$ along with a decrease in the fatigue safety factor to 2.8 , but the blocked force would be drastically increased to 39N . Therefore, the angle of the arm was chosen to be 4.87° .

Notch Diameter

The next free variable that was tested was the notch diameter. The notch diameter was varied from 1mm to 3mm as shown in Figure 2-20.

The notch diameter has little effect on the range or blocked force. Therefore, the notch thickness was chosen to be 2.5mm to ensure a acceptable value of 3.3 for the fatigue safety factor.

Casing Pre-Stress

The last free variable that was investigated was the casing pre-stress. The casing pre-stress was varied from 400N to 800N as shown in Figure 2-21.

The range, blocked force, and fatigue safety factor decrease as the casing pre-stress is increased. Therefore, it is desirable to have a low casing pre-stress. However, the casing pre-stress must not be so low that Nut 3 comes out of contact with the outer casing during actuation. Choosing a casing pre-stress of 565N provides a force of 206N between Nut 3 and the casing during actuation, as shown in Figure 2-15

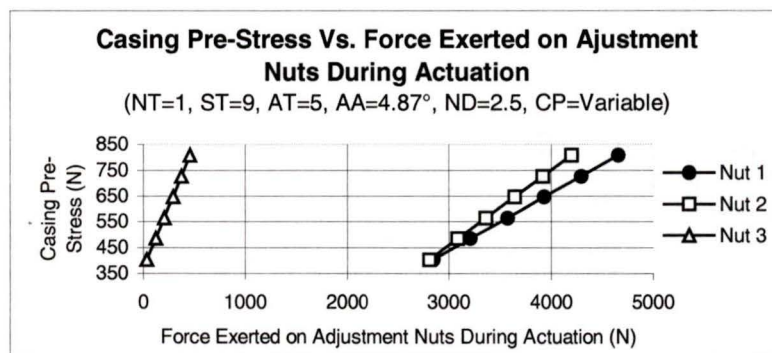


Figure 2-15 Casing pre-stress vs. force exerted on adjustment nuts during actuation

Note that for adjustment Nut 1 the positive force is taken downward where as for adjustment Nuts 2 and 3 the positive force is taken upward.

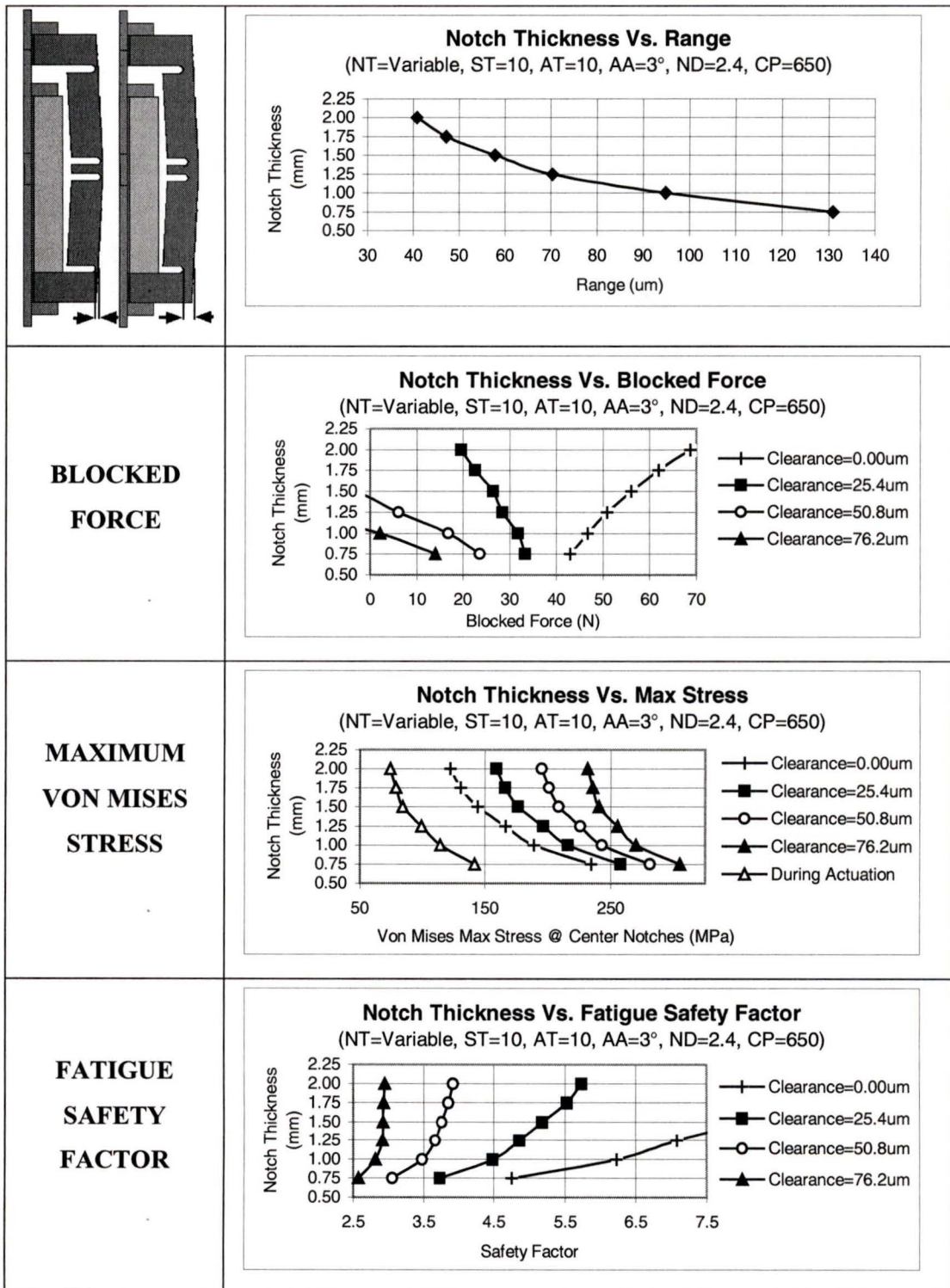


Figure 2-16 Variation of notch thickness with free dimension design parameters

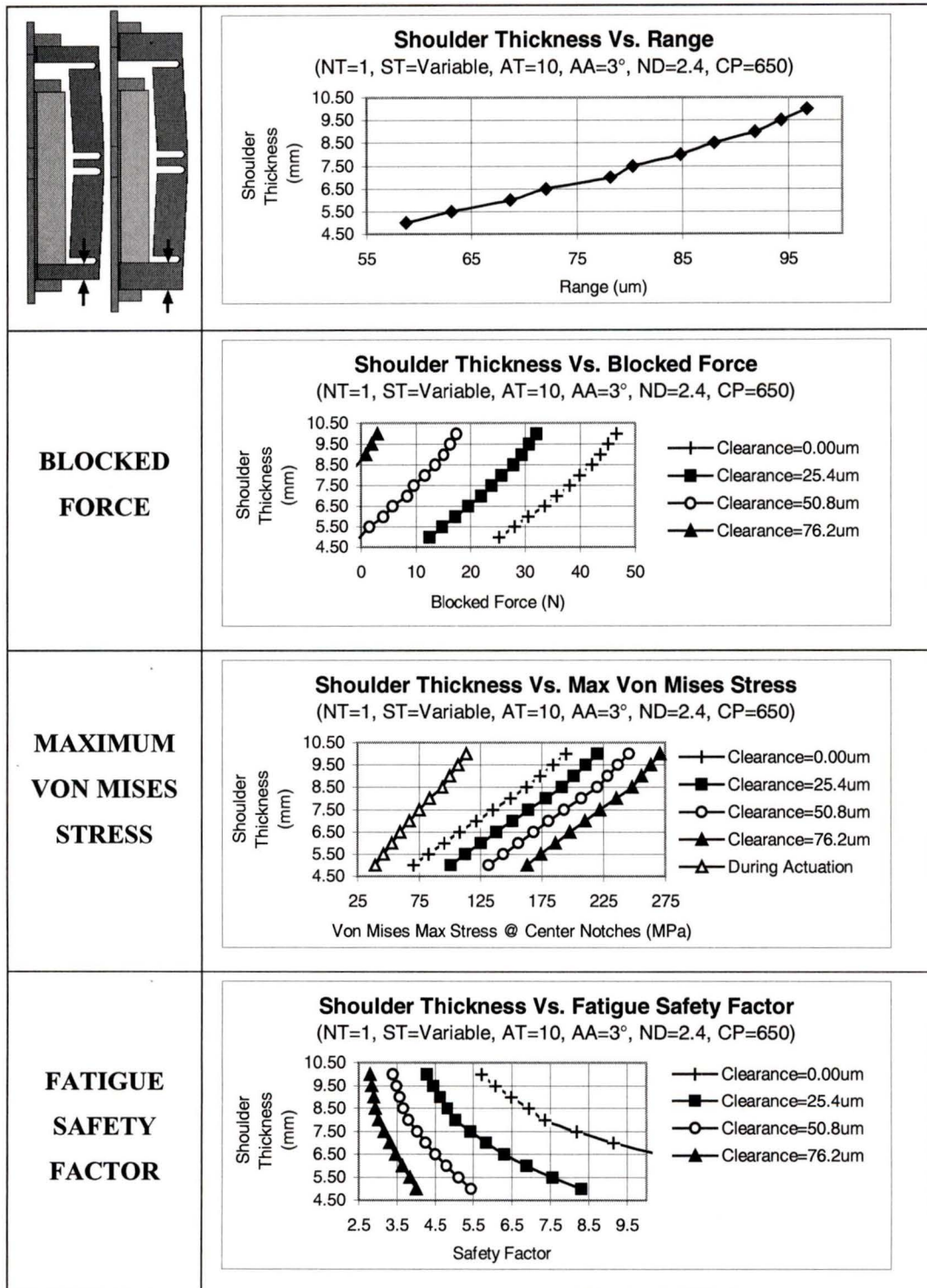


Figure 2-17 Variation of shoulder thickness with free dimension design parameters

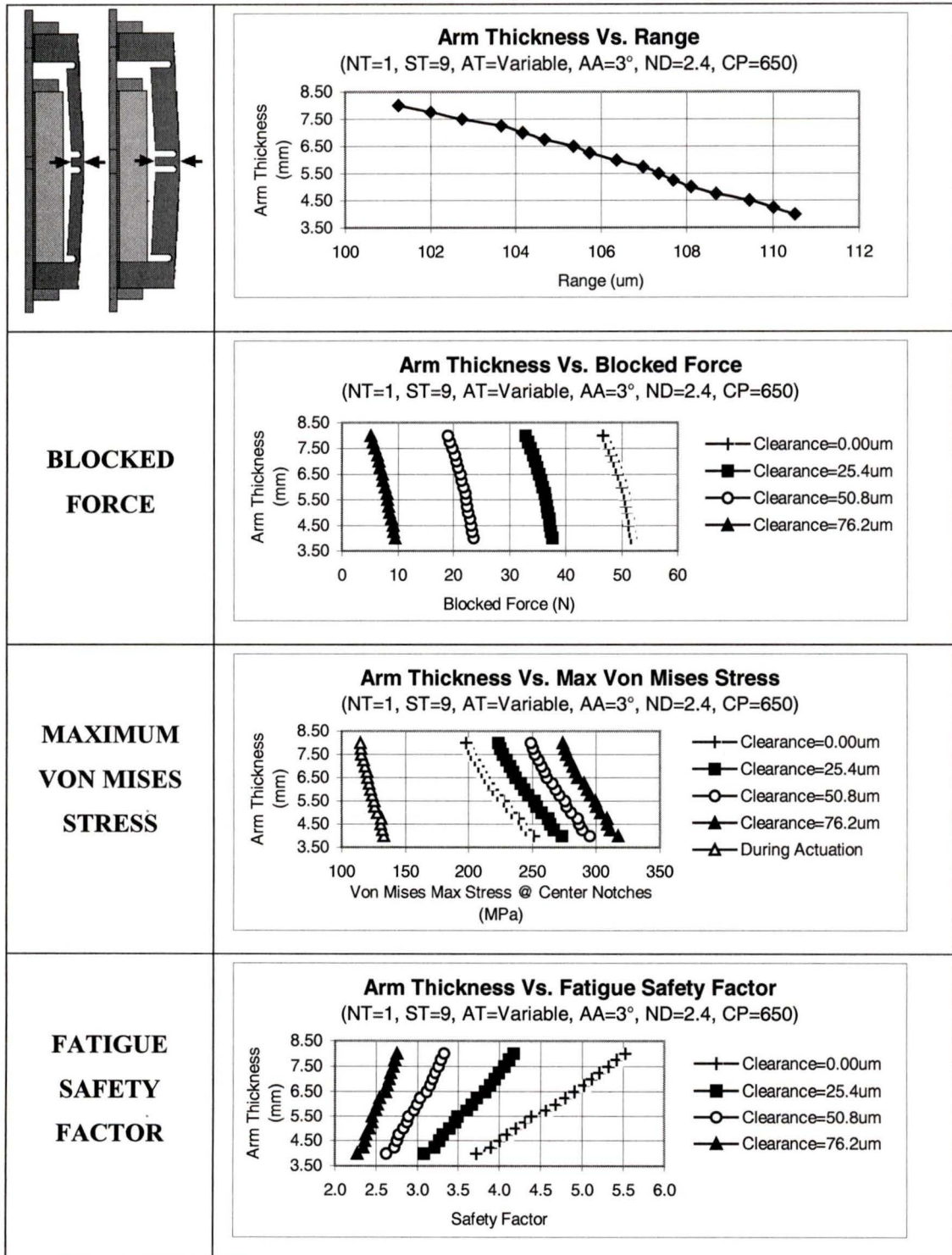


Figure 2-18 Variation of arm thickness with free dimension design parameters

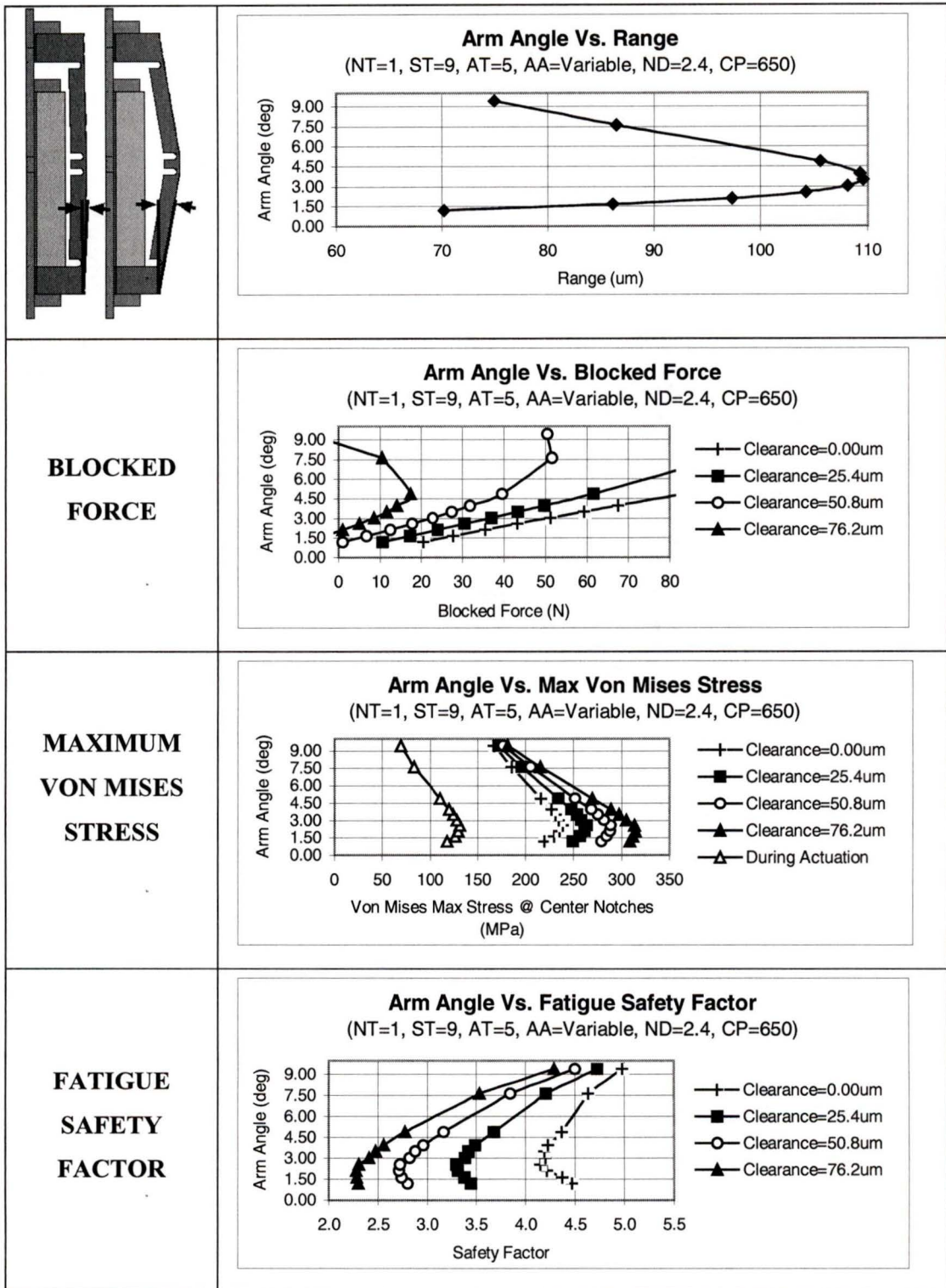


Figure 2-19 Variation of arm angle with free dimension design parameters

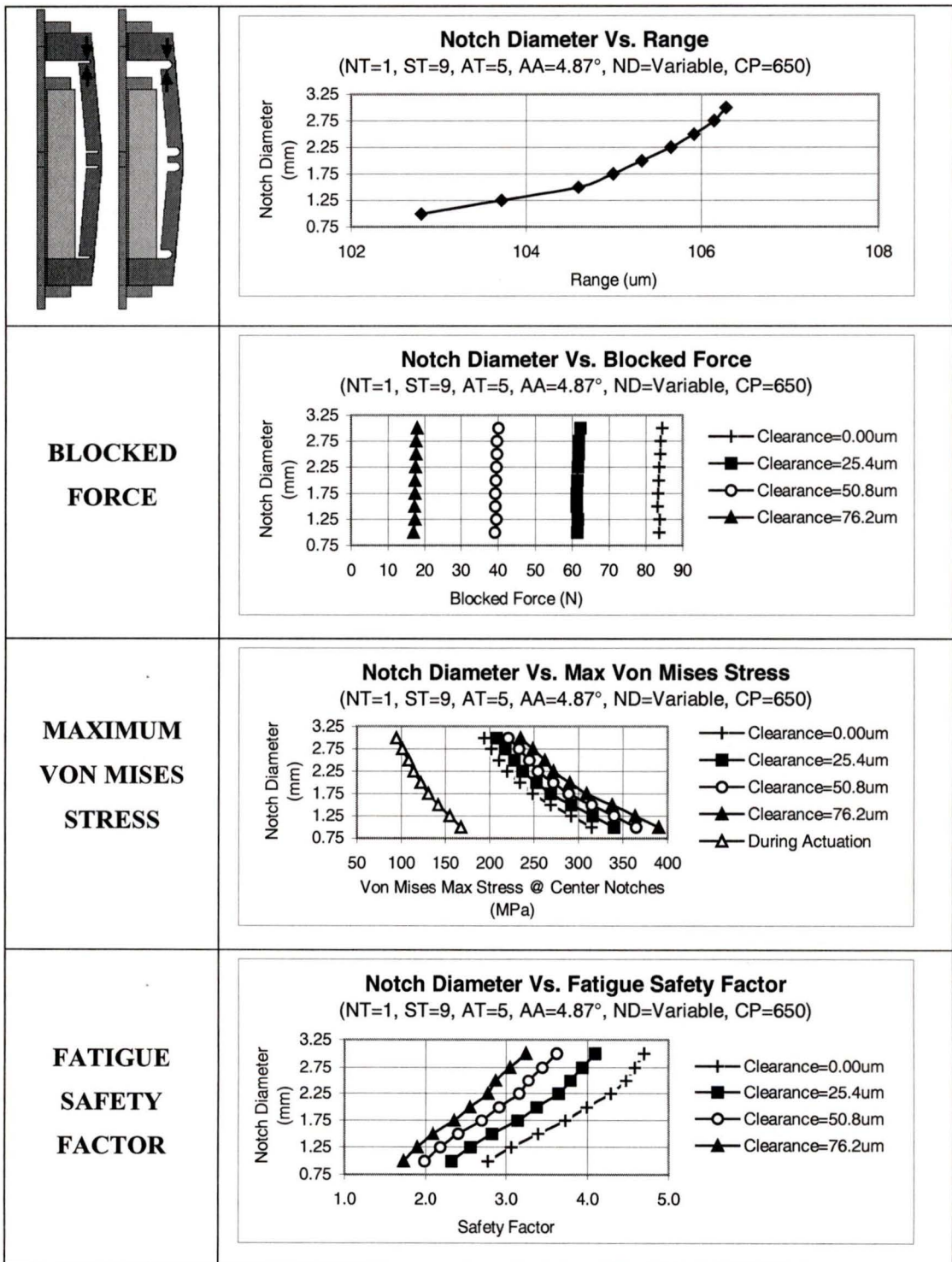


Figure 2-20 Variation of notch diameter with free dimension design parameters

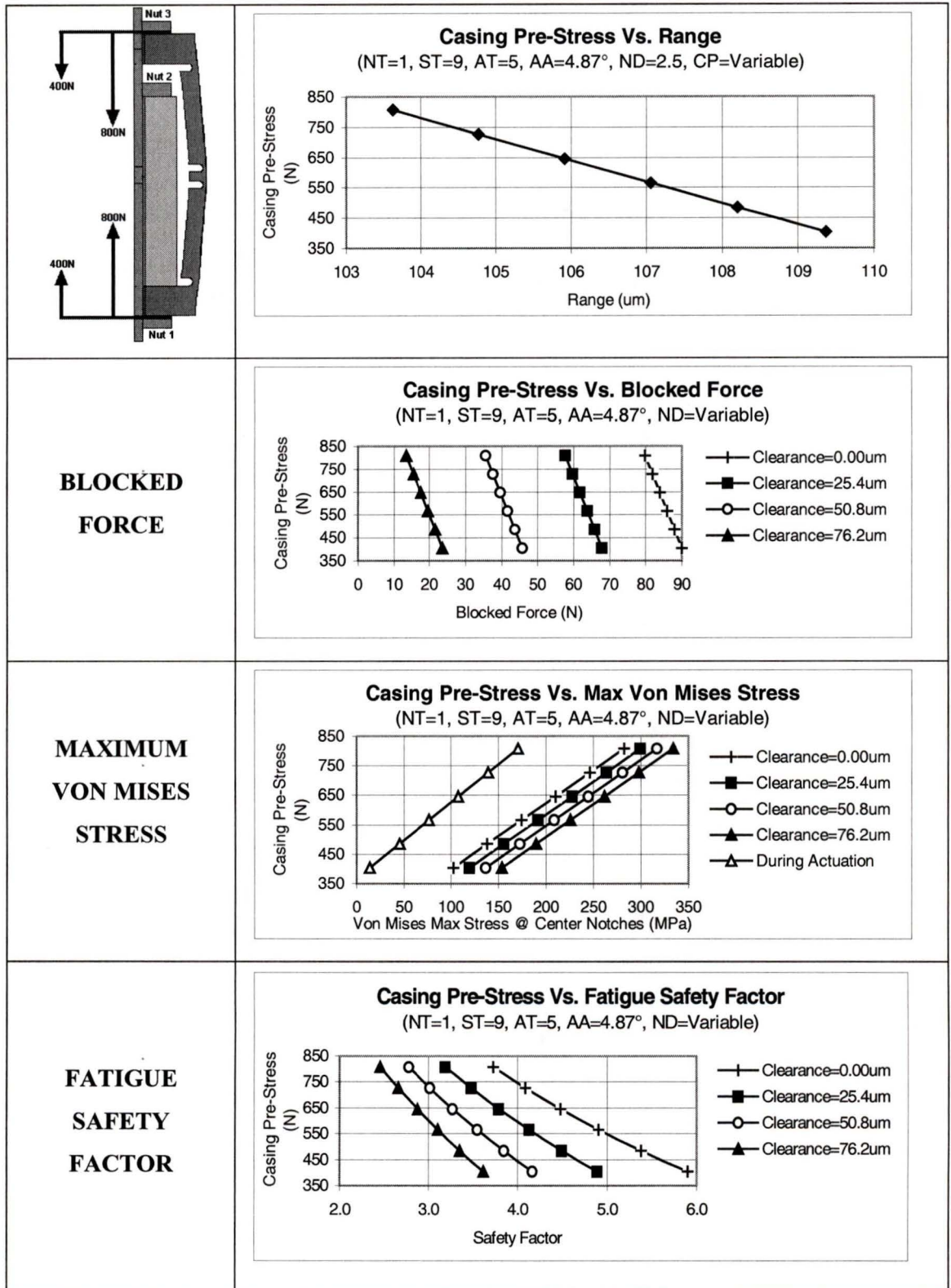


Figure 2-21 Variation of notch diameter with free dimension design parameters

2.8. Final Design

The dimensions of the brake assembly for the final brake assembly are shown in Figure 2-22, (refer to Figure 2-11 for definitions).

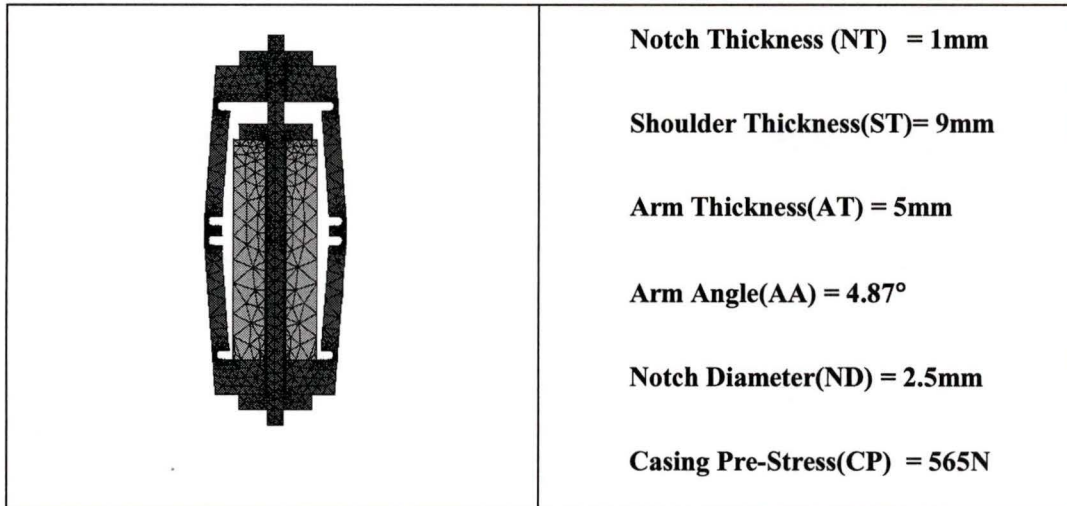
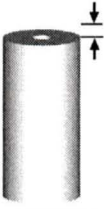
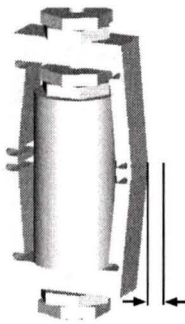
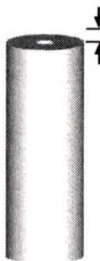


Figure 2-22 Final design modeling results

Using these dimensions the results of the actuator are shown in Table 2-4.

Table 2-4 Ansys design model results

Inchworm Actuator Design Model Results	Ansys Design Model
Brake Stack Free Disp. (um) 	30.0
Brake Pad Disp. (um) 	107.4
Extending Stack Free Disp. (um) 	39.9
Brake Pad Blocked Force (N): 25.4 Clearance 50.8 Clearance	64.2 41.6
Actuator Output Force (N): 25.4 Clearance 50.8 Clearance	83.5 54.0

The brake pad blocked force is related to the actuator output force through the coefficient of friction constant “ μ ” as defined in Equation 2-7.

$$AOF = 2 * \mu * N \quad (2-7)$$

where,

$$AOF = \text{Actuator output force}$$

μ = Static coefficient of friction

N = Brake pad blocked force

The multiple of “2” exists in the above equation to account for the two brake pads. Unfortunately, the coefficient of friction constant “ μ ” is a system property, not a material property. It is dependant on many factors such as material, counter-material, lubrication, temperature, speed, loading force, surface finish, surface finish of the counter-material, and type of motion (reciprocating, rotating). Published values can have large variations and range from 0.05 to 0.90. The inside crawler is made from titanium and the outside casing can either be made from titanium or oil hardened tool steel. A typical value is 0.65 for titanium against steel and 0.38 for titanium against titanium [52]. Using these values the actuator output forces are presented in Table 2-5. It is expected the actuator clearance should be between 25.4 μm and 50.8 μm [47].

Table 2-5 Actuator output force

Brake Pad Clearance (μm)	Actuator Output Force (N)	
	Ti on Steel	Ti on Ti
0	112	65
25.4	84	48
50.8	54	32
76.2	25	15

For reduced cost of machining and increased frictional force the material choice for the prototype is oil hardened tool steel.

2.9. Finite Element Mesh Study

The accuracy of the FEA model is dependant upon the mesh density [45]. To ensure a sufficient mesh density, the final model was analyzed with a fine and a coarse mesh as shown in Figure 2-23.

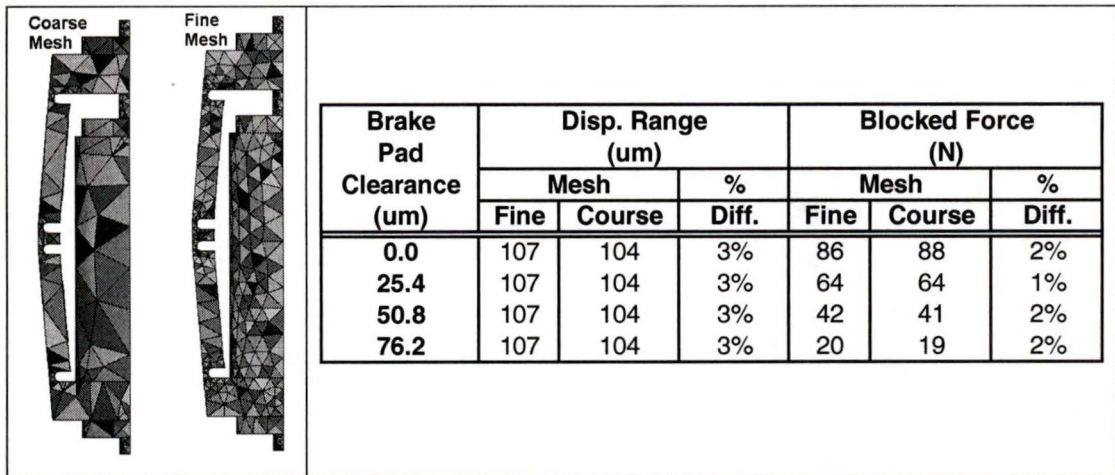


Figure 2-23 Mesh density analysis

The fine mesh consisted of 12,455 nodes and 6,512 elements, while the coarse mesh had 5,421 nodes and 2,588 elements. The results differ by less than 5%, ensuring the mesh density is acceptable.

ACTUATOR PROTOTYPE AND TESTING

A prototype of the computer model was built to attain physical measurements to validate the final design of the actuator. To accomplish this, the procedure was performed in three steps: the assembly of the inner crawler, the manufacturing of the outer casing and the design of the controller. Upon completion of each component of the actuator, the prototype was assembled and tested. A discussion of each prototype component prototyping and testing is followed by a comparison of results.

3.1. Electrostrictive Stacks

The final design of the actuator assumed the incorporation of actuator stacks with a layer thickness of 0.381mm. Due to manufacturing difficulties, as this is still a maturing technology, Sensor Technology Limited was unable to deliver the projected stacks that were intended to be used in the prototype. The differences between the projected stacks originally modeled in Ansys and the supplied prototype stacks are given in Table 3-1.

Table 3-1 Comparison of design and prototype stacks

	Braking Stacks		Extending Stacks	
	Ansys Design Model	Supplied Prototype Stacks	Ansys Design Model	Supplied Prototype Stacks
Layer Thickness (mm)	0.381	0.500	0.381	0.760
Number of Layers	100	70	133	40
Total Stack Height (mm)	57.15	57.15	76.20	50.80
Maximum Voltage (V)	200	285	200	285
Equivalent d33 (pC/N)	1440	1187	1440	1465

The supplied prototype stacks are shorter, have fewer layers and a greater layer thickness. These factors contribute to a diminished stack performance. In efforts to compensate for these shortcomings a higher stack operating voltage was suggested. Despite this effort, the performance of the supplied extending stack was still significantly lower. The exact performance of each stack is discussed later in this chapter.

A pictorial representation of the stacks can be seen in Figure 3-1. The left stacks are the design stacks used in the Ansys model and the right stacks are the supplied stacks used in the prototype. Two brake stacks and one extending stack were used to assemble the inner crawler.

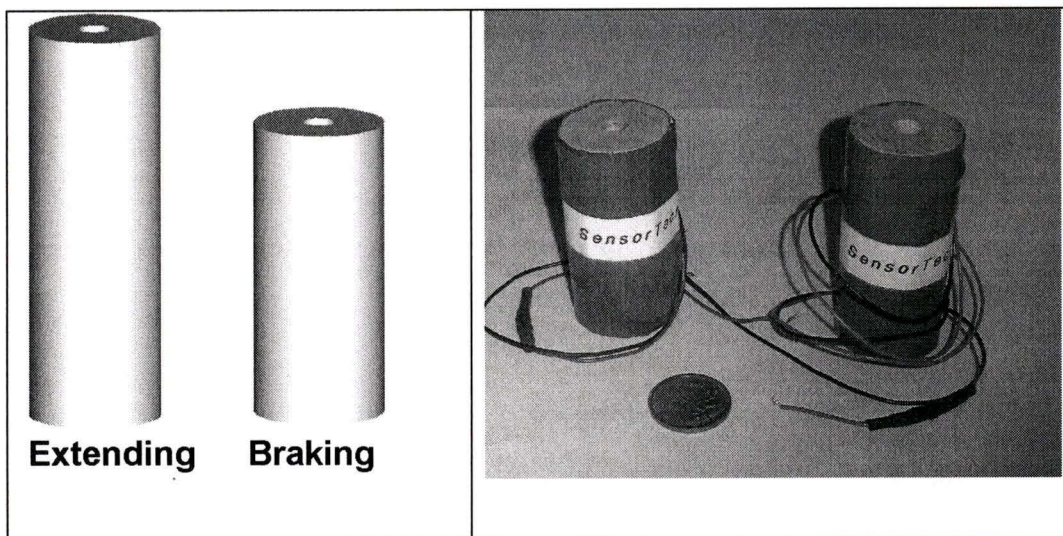


Figure 3-1 Design and prototype stacks

3.2. The Inner Crawler

The inner crawler is assembled from two flextensional frames, two brake stacks, one center stack, and a center rod with adjustment nuts to hold everything together, as shown in Figure 3-2.

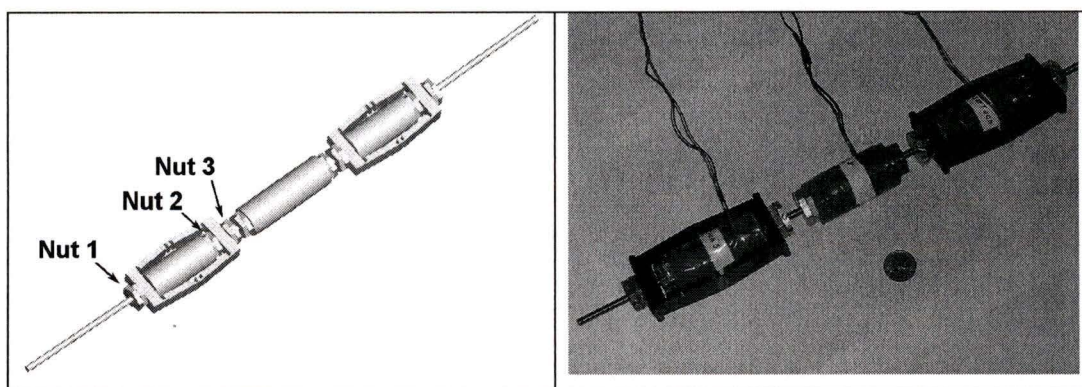


Figure 3-2 Inner crawler

Because the flextensional frames, shown in Figure 3-3, have a complex geometry and need to be manufactured with a tolerance of $12.7\mu\text{m}$ (0.0005in), electro discharge machining (EDM) was the chosen manufacturing method.

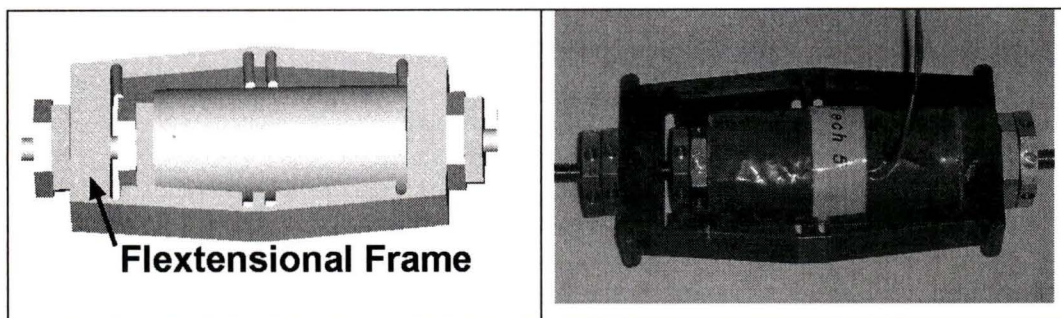


Figure 3-3 Flextensional frame

This process cuts each solid block of titanium using a fine copper wire passing a high voltage. The wire never actually touches the titanium enabling tolerances up to $2.54\mu\text{m}$ (0.0001in) [53].

It should be noted that the prototype frame has extra protrusions (called, guide bumps) along its outer perimeter. These protrusions were an after thought to help keep the inner crawler aligned within the channel during operation. Since the guide bumps are located in regions of low stress, they will not cause any significant discrepancies with the computer model results.

After the flextensional frames were machined, the inside crawler was ready for assembly. To accomplish this, the components were fitted onto the threaded rod and pre-stressed using the adjustment nuts. In order to apply the proper pre-stress the nuts are tightened using a two step sequence. See Figure 3-4 for the force on the adjustment nuts before stack actuation for different casing pre-stress values.

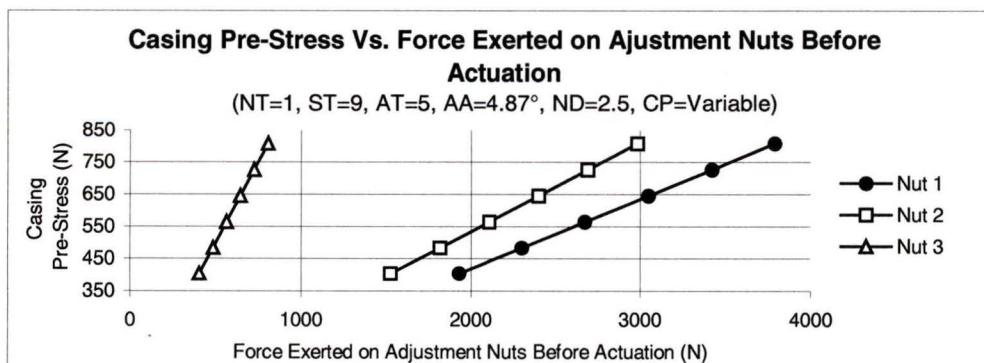


Figure 3-4 Casing pre-stress vs. force exerted on adjustment nuts before actuation

Initially Nut 3 is loose and the stack is not energized. Choosing a pre-stress of 565N (as discussed earlier in §2.7.) Nut 1 and Nut 2 are tightened to a value of 2676N, while Nut 3 remains loose. Now, Nut 1 is tightened against Nut 3 to a value of 565N. The action of tightening Nut 1 and Nut 3 reduces the force between Nut 1 and Nut 2 to a value of 2111N. The corresponding pressure on the stack is therefore 4.45N/mm², (which is the recommended pre-stress by the manufactures of the stacks [43]).

The nuts on the center stack are also tightened to a value of 2111N to achieve a stack pre-stress of 4.45N/mm². To apply the correct pre-stress the necessary tightening torque was evaluated using Equation 3-1 [39].

$$T = \frac{Fd_r}{2} \left(\frac{\tan \lambda + \mu_r \sec \alpha}{1 - \mu_r \tan \lambda \sec \alpha} \right) + \frac{F\mu_p d_n}{2} \quad (3-1)$$

where,

T = Tightening torque

F = Pre-stress force

d_r = Mean diameter of threaded rod

μ_r = Coefficient of friction on nut threads

λ = Thread lead angle

α = Thread angle

μ_p = Coefficient of friction of nut surface against the stack

d_n = Outer mean diameter of nut

The rod is made from titanium with a 10-32 thread ($d_r = 4.318 \times 10^{-3}$ m, $\lambda = 3^\circ$, $\alpha = 30^\circ$). The outer mean diameter of the nut is $d_n = 2.395 \times 10^{-2}$ m. The coefficient of friction is taken as a lubricated thread ($\mu_r = \mu_p = 0.15$ [39]). Using this information to achieve a pre-stress of 2676N the necessary tightening torque is 6.12N·m (4.50ft·lbf).

Similarly, to achieve a pre-stress of 565N the necessary tightening torque is 1.29N·m (0.95ft·lbf).

3.3. Outer Casing

The first idea for the outer casing is shown in Figure 3-5.

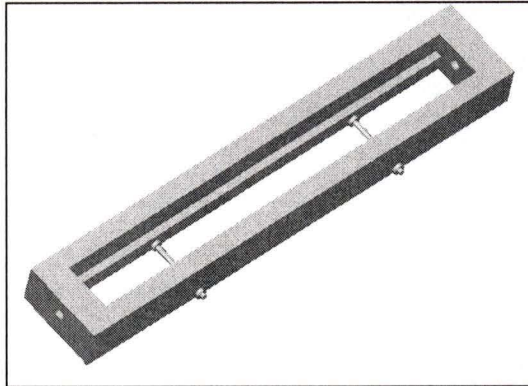


Figure 3-5 First outer casing design

The inner channel was to be cut from a solid block of titanium using the wire EDM process. Smooth delrin rails were then to be mounted on the inside of the channel to guide the inner crawler. Bracing bolts would then be used to stiffen the channel walls. The cost to manufacture such a part was not economically feasible, therefore, a different design was necessary.

The second option for the outer casing design is presented in Figure 3-6.

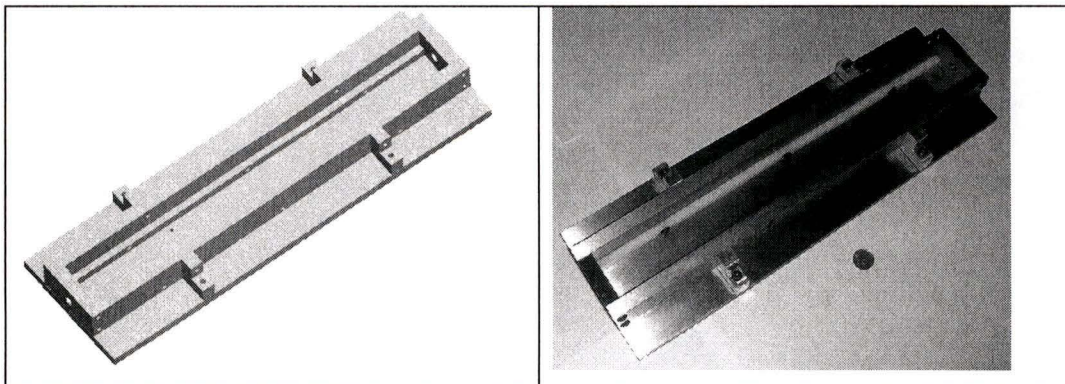


Figure 3-6 Final outer casing design

This design is made from oil hardened tool steel instead of titanium. The primary aim of this design is to achieve a casing wall width within a tolerance of $25.4\mu\text{m}$ (0.001in) [47]. Insertion of the inner crawler into the outer casing is shown in Figure 3-7.

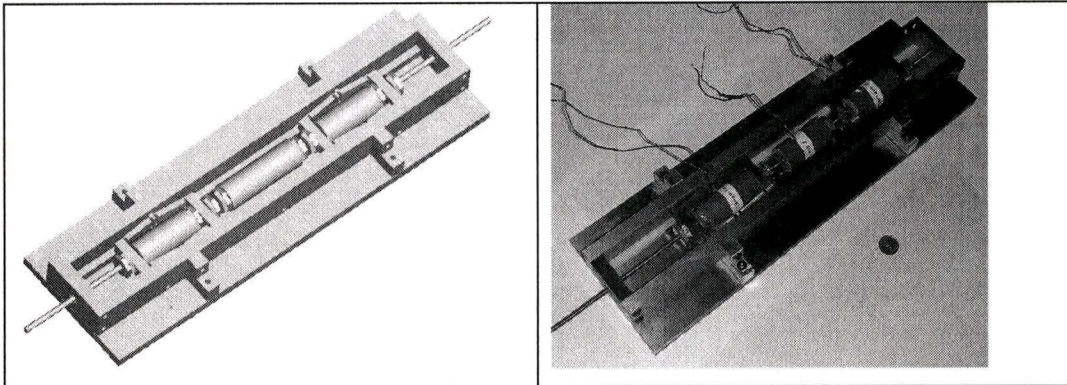


Figure 3-7 Assembly of outer casing and inner crawler

To create motion of the inner crawler, the stacks need to be fired in a particular sequence. This is done by means of a controller.

3.4. Controller Design

A controller was designed to control the actuation of each stack. The controller was made with two modes: one for assembly, and one for actuating. The assembly mode, energized the braking stacks to allow insertion of the crawler into the outer casing. The actuation mode was designed to fire each stack in a sequence that would cause the inner mechanism to linearly translate.

In actuating mode the waveforms supplied to the stacks were varied in frequency, amplitude, duty cycle and form. This was accomplished by using a PicStic 4x microprocessor that was programmed in the PicBasic language. The features of the microcontroller consist of: its two channel 12 bit digital to analog converter, its 8 bi-directional bit programmable high current input output lines and its high performance processor. In order to supply a voltage differential to the stacks to excite them a two-step power amplification circuit was designed. The first stage amplified the waveforms output by the PicStic using (AMP02) high accuracy instrumentation amplifiers. The AMP02s design allows a very high bandwidth over a wide range of gains making it ideal for rapid data acquisition [54]. Gain of the AMP02 is set using a

single external resistor (R_G) and can range from 1 – 10,000. The gain, G , is calculated from the Equation 3-2:

$$G = \frac{50k\Omega}{R_G} + 1 \quad (3-2)$$

For a chosen R_G value of 33k Ω the gain is 2.5. The output from the AMP02 can then be further amplified by using a high voltage power amplifier.

Three model SA-10 high voltage power amplifiers and one SA-20 high voltage power supply were obtained from Sensor Technology Limited. The SA-10 is a two-channel high voltage power amplifier, it can be used as two individual ground referenced amplifiers providing a gain of 15, or a single bridged amplifier providing a gain of 30. Each channel gives a maximum ground referenced voltage variation of nominally 280 V peak-to-peak. In bridged mode, the SA-10 provides a differential voltage variation of 560V [55]. During prototype testing the high voltage amplifiers and instrumentation amplifiers were configured to obtain a voltage of 285V across each stack. The circuit schematic is shown in Figure 3-8.

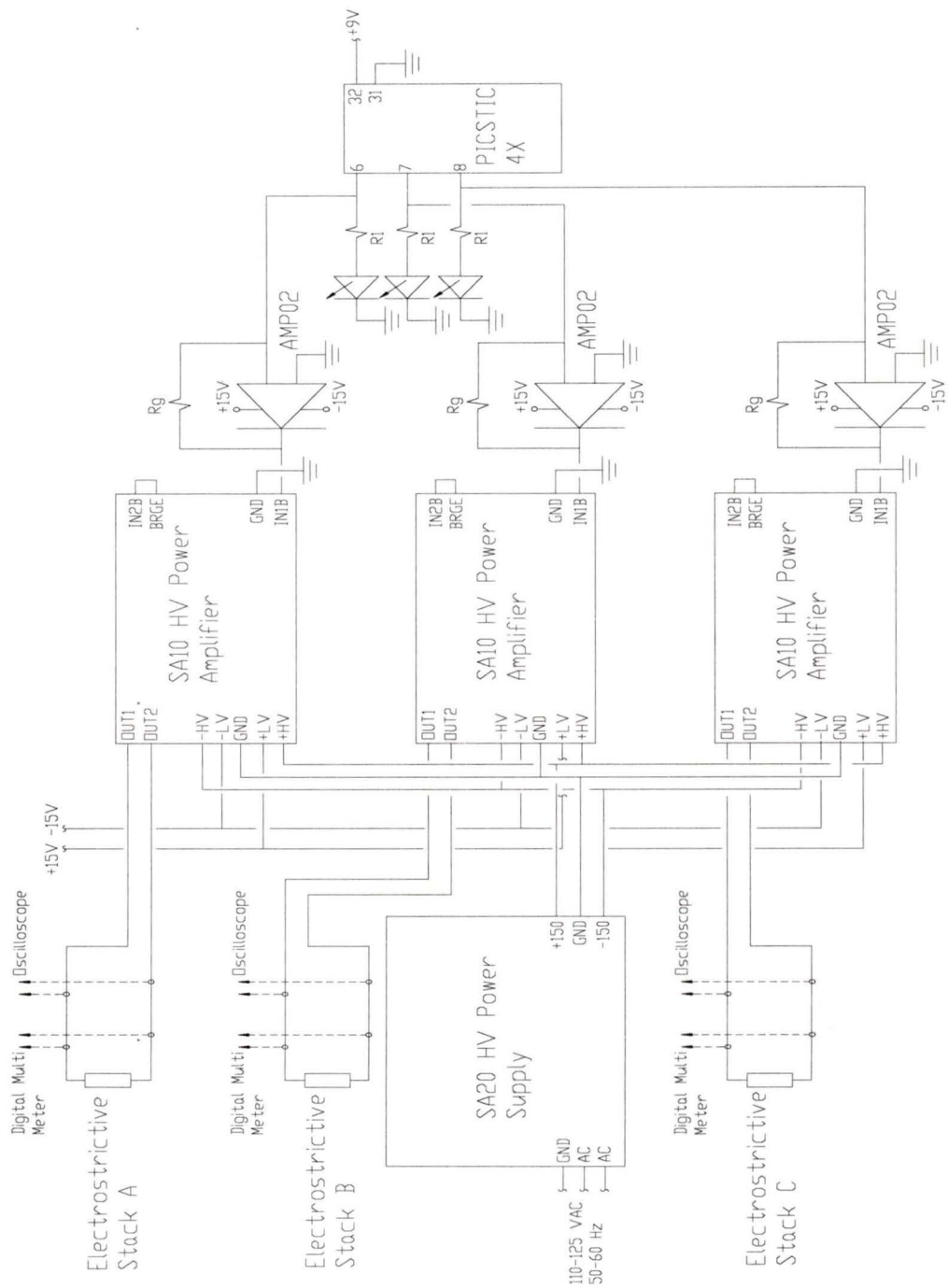


Figure 3-8 Controller schematic

The diodes are used as a visual representation of the firing of each stacks, where R_1 is 333Ω . A picture of the circuit is shown in Figure 3-9.

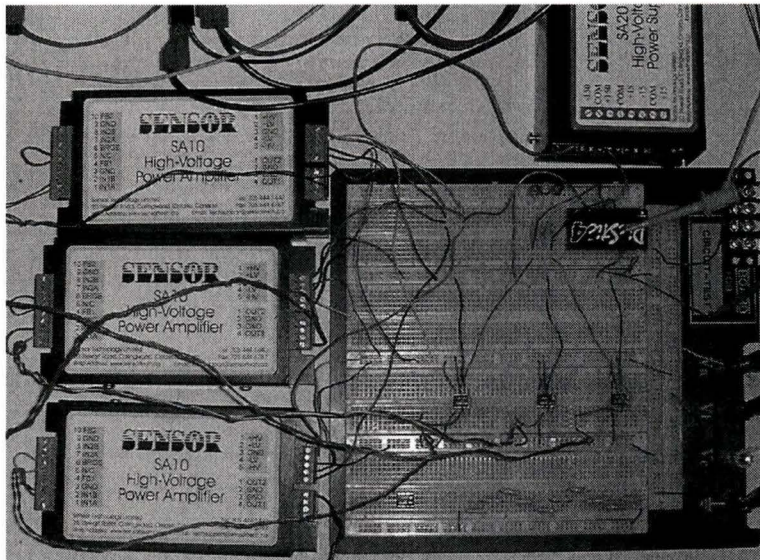


Figure 3-9 Controller assembly

The actuating mode of the controller has two options. The first used square waves output from the PicStic that were then varied in amplitude, frequency and duty cycle. These waveforms were constructed using high and low logic levels cycled over chosen input-output pins of the PicStic. The waveforms applied to each stack are shown in Figure 3-10.

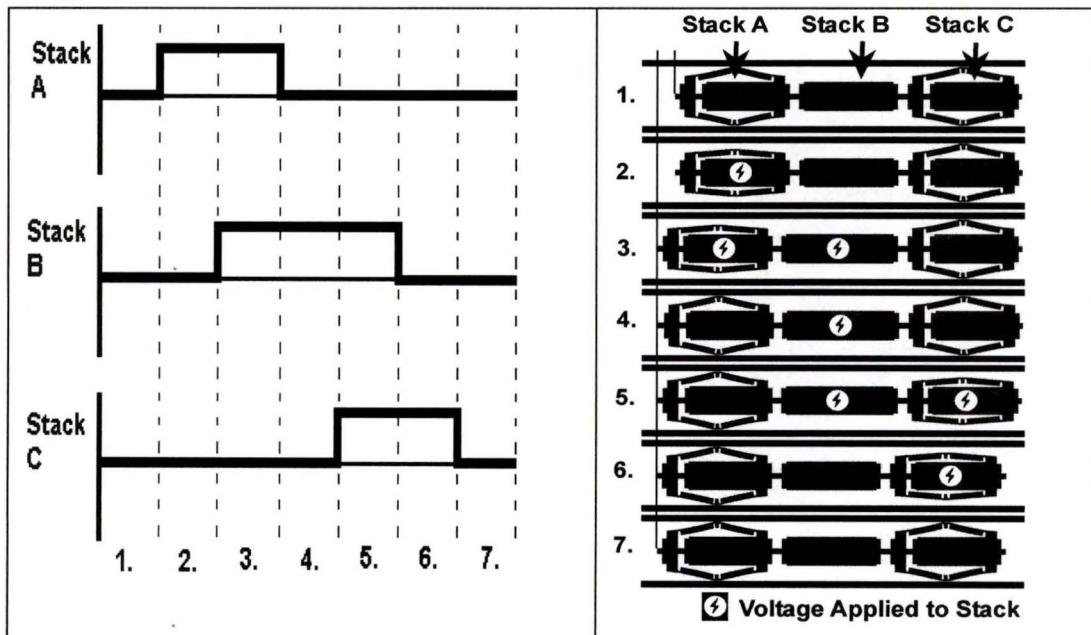


Figure 3-10 Controller waveforms

This firing sequence is intended to make the inner crawler move within the channel with a maximum controller frequency of 170Hz. The second actuation option uses a ramping waveform applied to the center stack.

From previous papers [33,34] it was discovered that ramping the signal of the center stack provided an increase in velocity of similar actuators when compared against the square wave signal at frequencies above 100Hz (due to less jarring motion). The ramping of the center stack was accomplished by using the digital to analog converter of the input-output coprocessor on the PicStic; to create four intermediate steps between the high and low voltage levels, as shown in Figure 3-11.

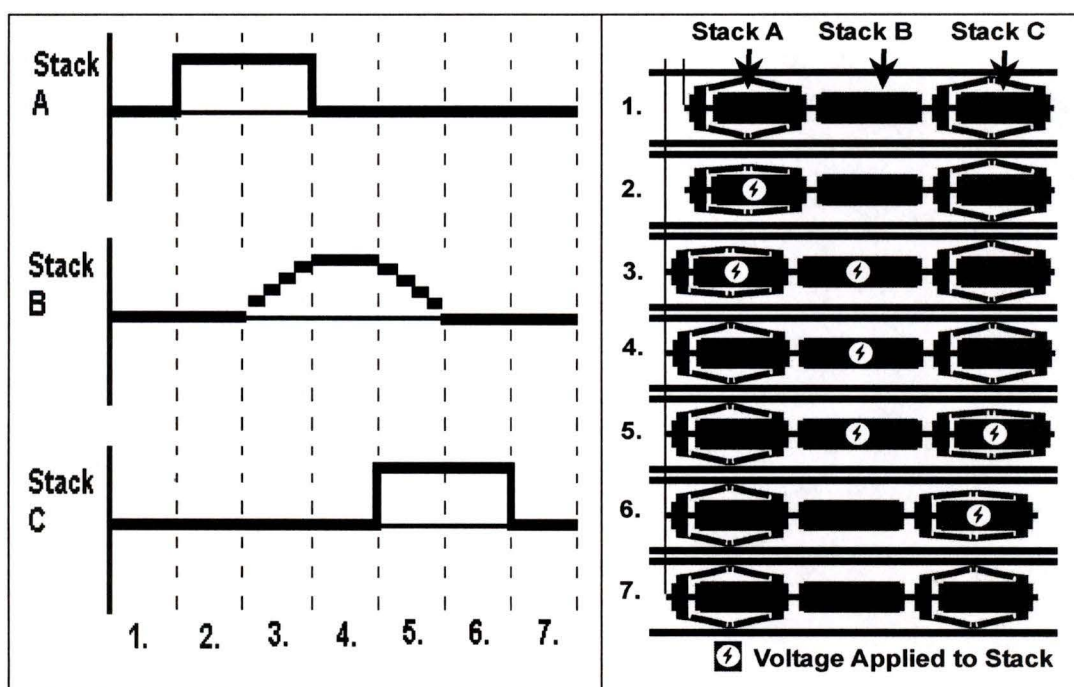



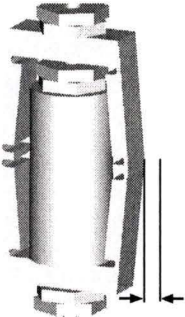

Figure 3-11 Controller waveform with ramping function

Because the ramping function requires several intermediate steps, the maximum operating frequency of this signal is limited to 45Hz.

3.5. Prototype Results

The prototype was tested. For comparison purposes and to have a common frame of reference, the Ansys model was modified to reflect the stacks supplied by Sensor Technology Limited. The results of the prototype and the Ansys prototype model are presented in Table 3-2.

Table 3-2 Brake assembly results of Ansys prototype model and prototype

Inchworm Prototype Results	Ansys Prototype Model	Measured from Prototype
Brake Stack Free Disp. (um) 	27.1	26.0
Brake Pad Disp. (um) 	78.2	71.1
Extending Stack Free Disp. (um) 	16.7	16.0
Brake Pad Blocked Force (N): 25.4 Clearance 50.8 Clearance	18.6 7.5	---
Actuator Output Force (N): 25.4 Clearance 50.8 Clearance	24.2 10.0	15.1
Max. Operating Freq. (Hz)	2.22	0.33
Actuator Speed (mm/min)	1.0	0.2

The quickest time the stacks can become charged (87% of maximum charge) or de-charged (13% of maximum charge) is 0.075s [43]. Since there are six steps in each cycle of the actuator motion, the quickest time for one cycle of the inchworm movement is $6 \times 0.075s = 0.45s$. This corresponds to a maximum operating frequency of 2.22Hz. Multiplying this value by the extending stack displacement per step (7.2 μ m) gives the theoretical actuator speed of 1.0mm/min. During testing this

frequency was unattainable. Only a frequency of 0.33Hz could be obtained before the inchworm started to decrease in velocity because the stacks were not fully charging and de-charging. For frequencies greater than 1.67Hz the actuator did not move. Identical results were achieved when using the controller ramping signal. Neglecting the operating frequency, the difference in results between the model and the prototype differ by less than 9%, therefore validating the computer simulations.

ADAPTIVE TRUSS STRUCTURES

The concept of integrating active truss members into the design of space systems is anticipated to have many advantages over conventional structures. Vibration suppression [11], improved antenna pointing accuracy [56], obstacle avoidance [13] and increased structural strength [57] are some of the advantages these hybrid structures can offer.

Space systems projected for launch in the near future include the Geostationary Platform (GPF) planned by NASDA (Figure 4-1), and these large space platforms require accurate pointing of antennas in the presence of structural flexibility [56].

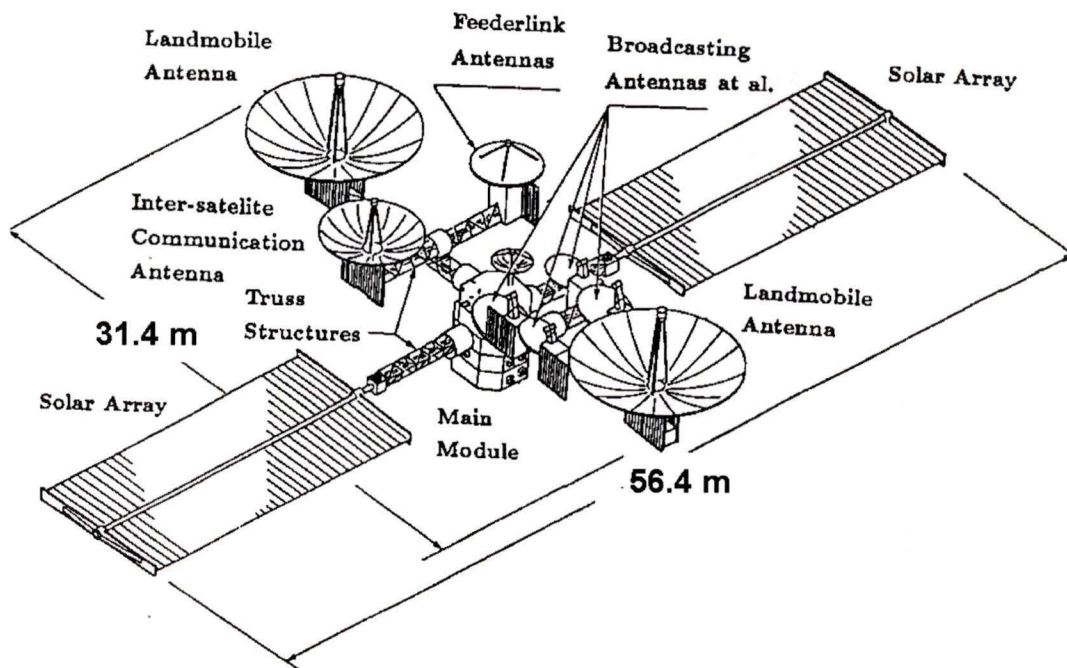


Figure 4-1 NASDA's future geostationary platform (GPF)

The GPF system has antennas for broadcasting, land mobile communications, feeder links, and inter-satellite communications. Since the antennas are fixed to the structure, pointing error may arise from unevenness of material properties, thermal expansions

(transition from daylight to darkness), and structural vibrations. To correct for these potential errors, strain induced actuators are proposed to be integrated into this design [56]. Another proposed spacecraft by a European research group ARES consists of an antenna attached to an adaptive truss is shown in Figure 4-2.

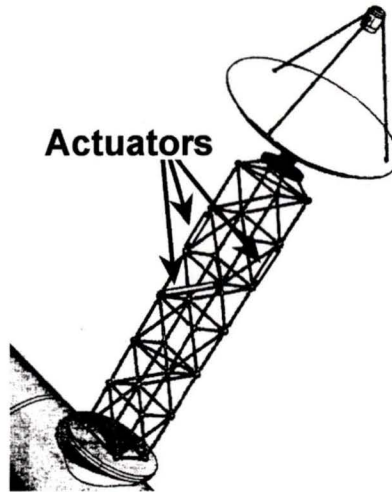


Figure 4-2 ARES's proposed space system

Space structures are often exposed to loads during shuttle docking, docking of structural members for construction, and capturing of floating satellites by a robotic arms [59]. Thus a concern for space structures is to maintain adequate structural strength in the presence of moving and varying forces and this has been a topic of research in the last decade [6-10]. This chapter demonstrates the application of the proposed inchworm actuator in variable geometry truss structures in order to maintain the overall strength of the truss assembly.

4.1. The Concept

When a load varying in direction is applied to an adaptive structure, it changes its shape in order to maintain or improve its overall structural strength. To demonstrate this concept, a fixed statically determinate one-story truss is optimized and compared with the same truss having a single active element (member containing an actuator). The structures were analyzed using Ansys and the results verified using MatLab. Next, the optimization algorithms available in Ansys and MatLab are discussed using the one-story truss as an example. Subsequently, two more statically determinate structures (a two-story truss and a 3D pyramid) were analyzed. Finally, more

complicated statically indeterminate structures were also solved to prove its applicability in complex systems as well. For all the cases studied, each element of the truss structure is assumed to have an ultimate strength of 260MPa and a circular cross sectional area of $1 \times 10^{-4} \text{m}^2$.

One-Story Truss

In this section, a fixed and adaptable one-story truss have been analyzed and compared. In both cases, the top two members (elements 6 & 7) are assumed to be very strong and not considered in the analysis. Consider the one-story 2D truss structure as shown in Figure 4-3.

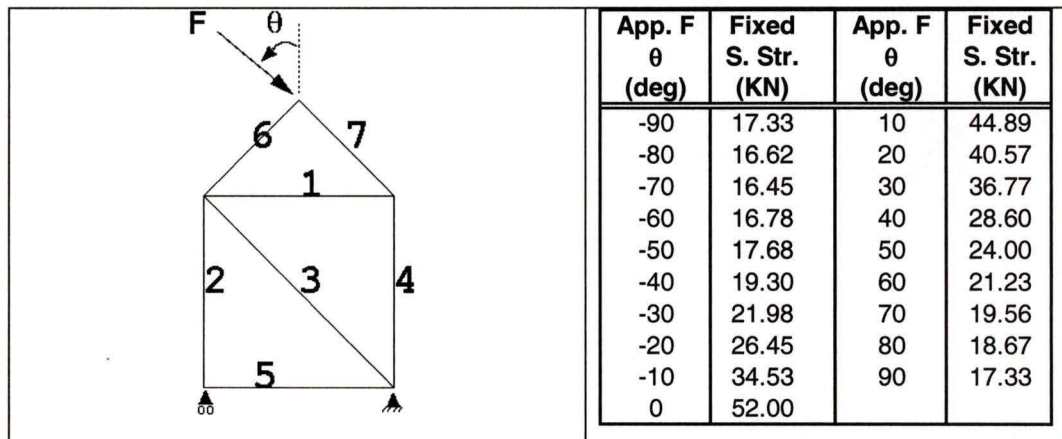


Figure 4-3 One-story fixed truss

The statically determinate structure has its right base fixed and its left base on rollers. A unit load is applied to the apex of the one-story structure at an angle θ with the vertical. Naturally, for each different θ value a new set of element stresses is created.

Since the analysis is linear, ratios were used to determine the maximum structural strength. More precisely, multiplying the ultimate stress by the unit load and dividing by the stress created by the unit load yields the structural strength as shown in Equation 4-1.

$$\text{Structural_Strength} = \text{Ultimate_Stress} \left(\frac{\text{Unit_Load}}{\text{Stress_Created_by_Unit_Load}} \right) \quad (4-1)$$

The corresponding structural strength is shown in Figure 4-4. Evidently, the structure is strongest when $\theta \approx 0^\circ$, while the strength tapers off as the load moves from the vertical position.

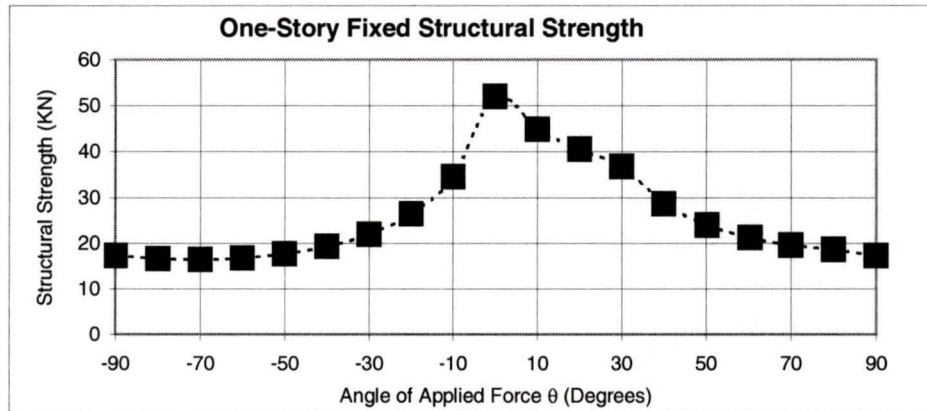


Figure 4-4 One-story fixed structural strength

Consider now the same truss with one active member as shown in Figure 4-5.

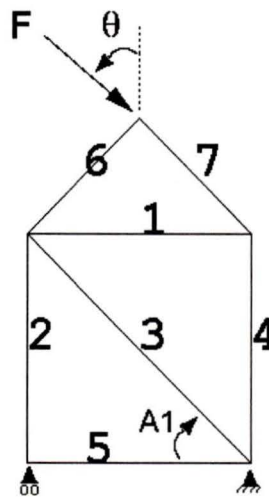


Figure 4-5 One-story adaptive truss

All members are fixed and do not change length except for active element number 3. When element number 3 changes length, the angle it makes with the horizontal ($A1$) also changes. We may therefore consider either the angle $A1$, or the length of element 3 as our design variable. For ease of computation $A1$ has been chosen. When $A1$ approaches 0° the structure leans to the left, whereas when $A1$ approaches 90° the structure leans right.

For each angle θ there is an angle $A1$ that minimizes the maximum absolute stress among all the elements. When the maximum absolute stress is minimized, the structural strength is maximized. Defining this problem as an optimization problem, the maximum structural strengths were determined using Ansys and verified in MatLab. The resultant structural strengths can be seen in Figure 4-6.

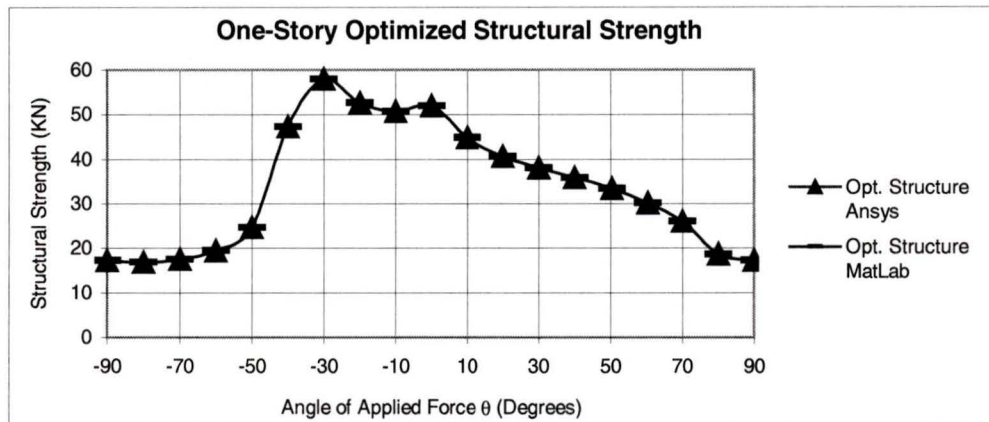


Figure 4-6 One-story optimized structural strength in Ansys and in MatLab

The above graph shows that the Ansys and MatLab results strongly agree. Also, the greatest structural strength is achieved when $\theta = -30^\circ$. These results also agree with the results reported in the literature in reference [57]. Referring to Table 4-1, slight variations in the optimized angles and the maximum stresses can be seen between the two optimization methods, and this is attributed to numerical round-off errors.

Table 4-1 One-story comparison of structural strength and optimized angle

App. F θ (deg)	Anslys Opt. A1 (deg)	MatLab Opt. A1 (deg)	Anslys S. Str. (KN)	MatLab S. Str. (KN)	Elem. #	T=1 C=0
-90	45.00	45.00	17.33	17.34	2	0
-80	53.72	53.72	16.91	16.92	2	0
-70	61.13	61.13	17.55	17.55	2	0
-60	68.53	68.53	19.53	19.54	2	0
-50	77.93	77.93	24.66	24.67	2	0
-40	81.42	81.44	47.33	47.38	2	0
-30	72.68	72.67	57.97	58.00	3	0
-20	61.59	61.57	52.61	52.66	1	1
-10	52.40	52.40	50.71	50.73	1	1
0	45.01	45.00	51.99	52.01	1	1
10	45.00	45.00	44.89	44.90	4	0
20	45.00	45.00	40.57	40.58	4	0
30	44.23	44.23	38.05	38.06	4	0
40	38.34	38.34	35.92	35.93	3	0
50	32.31	32.32	33.35	33.36	4	0
60	26.18	26.18	30.14	30.16	8	0
70	19.98	19.97	26.02	26.05	3	0
80	45.11	45.11	18.69	18.70	2	1
90	45.00	45.00	17.33	17.34	2	1

The rightmost two columns indicate the element with the maximum absolute stress and its state of tension or compression in the optimized configuration. The varying geometry shapes of the one-story truss are plotted in Figure 4-7.

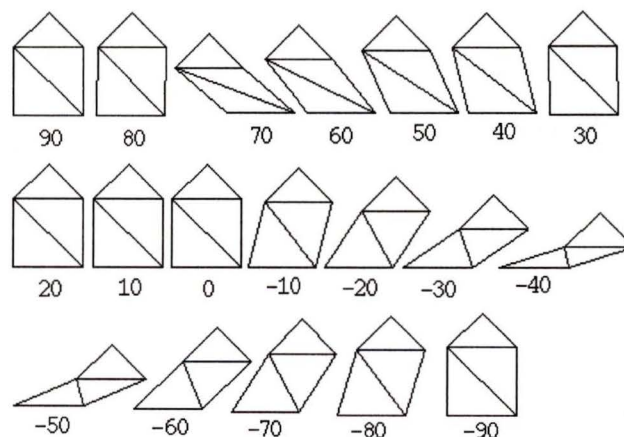


Figure 4-7 One-story adaptive shapes

The numbers below each varying shape correspond to the angle of applied force (θ). The structure remains upright ($A1 = 45^\circ$) at angles near 90° , 0° , and -90° . For all other angles, the structure leans left or right to minimize the maximum element stress.

Comparison of the results for the fixed and adaptive one-story trusses is shown in Table 4-2.

Table 4-2 One-story results

App. F θ (deg)	Ansys Opt. A1 (deg)	MatLab Opt. A1 (deg)	Ansys S. Str. (KN)	MatLab S. Str. (KN)	Fixed S. Str. (KN)	Elem. #	T=1 C=0
-90	45.00	45.00	17.33	17.34	17.33	2	0
-80	53.72	53.72	16.91	16.92	16.62	2	0
-70	61.13	61.13	17.55	17.55	16.45	2	0
-60	68.53	68.53	19.53	19.54	16.78	2	0
-50	77.93	77.93	24.66	24.67	17.68	2	0
-40	81.42	81.44	47.33	47.38	19.30	2	0
-30	72.68	72.67	57.97	58.00	21.98	3	0
-20	61.59	61.57	52.61	52.66	26.45	1	1
-10	52.40	52.40	50.71	50.73	34.53	1	1
0	45.01	45.00	51.99	52.01	52.00	1	1
10	45.00	45.00	44.89	44.90	44.89	4	0
20	45.00	45.00	40.57	40.58	40.57	4	0
30	44.23	44.23	38.05	38.06	36.77	4	0
40	38.34	38.34	35.92	35.93	28.60	3	0
50	32.31	32.32	33.35	33.36	24.00	4	0
60	26.18	26.18	30.14	30.16	21.23	8	0
70	19.98	19.97	26.02	26.05	19.56	3	0
80	45.11	45.11	18.69	18.70	18.67	2	1
90	45.00	45.00	17.33	17.34	17.33	2	1

The difference in structural strengths between the fixed and adaptive one-story trusses can be seen in Figure 4-8. The adaptive structure is significantly stronger than the fixed truss, especially when θ is between -50° and -10° .

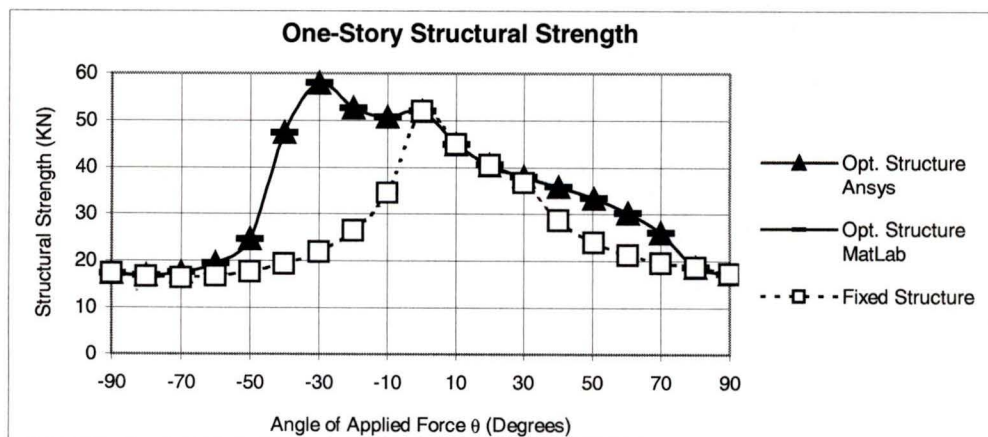


Figure 4-8 Structural strength of fixed and adaptive one-story trusses

4.2. Optimization Algorithms

Using the one-story truss as an example, the optimization algorithms will now be discussed. Optimization code was developed in both Ansys and MatLab to confirm and validate the results. Both methods approach the problem differently, but converge to the same results. The optimization procedure in Ansys will now be discussed followed by the procedure in MatLab.

Ansys Optimization

Performing an optimization in Ansys requires the use of two files: the analysis file and the optimization file. The analysis file contains all the model geometry, material properties, load information, and meshing data. This file was made parametrically so the optimization file could later access and modify the design variables during optimization. When the optimization file is opened, it accesses the analysis file and selects a random value of the design variable(s) within a predefined range. Considering the one-story truss as an example, the optimization file randomly chooses a value of $A1$ between an upper and lower limit of 0° and 90° , respectively. The structure is then analyzed using this value of $A1$. The maximum absolute element stress is stored for this particular $A1$ value. Repeating this for 130¹ randomly chosen $A1$ values generates 130 maximum absolute element stresses. The best value of $A1$ producing the lowest maximum absolute element stress (among the 130) is kept for the second optimization pass. The second optimization pass, like the first, uses 130 iterations. However, this time the range of $A1$ is reduced based on the best value of $A1$ from the first optimization. At most, the range of $A1$ is reduced by a factor of $2/3$, (found by trial and error). A factor greater than $2/3$ does not ensure the global minimum will be captured. Optimizing the one-story truss for each angle θ required ten optimization passes.

This optimization technique may best be illustrated by using a visual example. Imaging a unit load applied to the apex of the one-story adaptive truss at $\theta = -30^\circ$. To optimize the structural strength, the value of $A1$ that minimizes the maximum

¹ The maximum number of values the random optimization routine in Ansys can store is 130 [45]. The maximum number of evenly spaced values the sequential step routine can store is 10 [45]. The random optimization routine was therefore chosen over the sequential step routine due to increased probability of capturing the absolute minimum.

absolute stress among all the elements needs to be determined. Representation of the range of A1 angles on a line from 0° to 90° is shown in Figure 4-9



Figure 4-9 Line representation of A1 range

Taking 130 random values of A1 between 0° and 90° performs the first optimization pass. Each “x” in Figure 4-10 indicates a random A1 value.

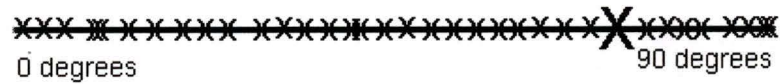


Figure 4-10 Random values of A1 between 0° and 90°

The best value of A1 (producing lowest maximum absolute element stress) occurs at 82° and is shown by “X”.

For the next optimization, a new reduced range of A1 is calculated. Adding and subtracting a fixed value to the best A1 determines this new range. As mentioned before, this fixed value ensures the design space is not reduced by more than 2/3 of the previous. In this case, the new upper and lower ranges are $82^\circ - 45 \cdot 2/3 = 50^\circ$ and $82^\circ + 45 \cdot 2/3 = 112^\circ$, respectively; however, since 112° is outside the maximum value of 90°; the upper limit is taken as 90°. Therefore, the new range becomes $50^\circ \leq A1 \leq 90^\circ$ for the second optimization. Again, 130 random values of A1 are generated, this time between 50° and 90°. The best solution occurs at $A1 = 75^\circ$ as shown in Figure 4-11.

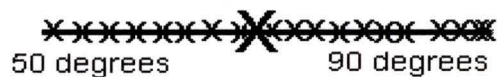


Figure 4-11 Random values of A1 between 50° and 90°

For the third optimization, the new range is not reduced by more than $2/3$ of the previous. Therefore, the new limits are now $75^\circ - 45 \cdot (2/3)^2 = 59^\circ$ and $79^\circ + 45 \cdot (2/3)^2 = 99^\circ$. Again the calculated upper limit of A1 is outside the maximum value of 90° , so the upper limit is taken as 90° . The new range of A1 is between 59° and 90° for the third optimization. Once again we take 130 random values of A1 between 59° degrees and 90° degrees. This time the best solution of A1 occurs at 74° as shown in Figure 4-12.



Figure 4-12 Random values of A1 between 59° and 90°

Continuing this procedure ten times, the final optimization tests 130 random A1 angles between 71.51° and 73.85° . The optimal A1 was found to be 72.68° . This method was repeated for each θ value.

MatLab optimization

The optimization procedure in MatLab is quite different from that used in Ansys. Moreover, it is limited to determinate structures. At each node, a force equilibrium equation is written. All the generated equations are then arranged into the matrix form:

$$Ax = b \quad (4-2)$$

where,

x is a column vector containing the element forces ($x = [F_1, F_2, F_3, F_4, F_5]$).

This set of equations constitutes the optimization constraints. Next, the objective function is defined. The maximum structural strength is achieved when the absolute minimum of the maximum force is reached. If the one-story truss is considered, the objective function may be written as:

$$Objfun = \max[abs(x)] \quad (4-3)$$

An equivalent objective function can be written if we consider the built in MatLab function $NORM(x, n)$, (when n approaches infinity: $n \rightarrow \infty$). The function takes the n^{th} norm of the column vector x . Then, $NORM(x, n) = [\text{abs}(F_1)^n + \text{abs}(F_2)^n + \text{abs}(F_3)^n + \text{abs}(F_4)^n + \text{abs}(F_5)^n]^{1/n}$. Considering the limit as $n \rightarrow \infty$, the largest force becomes more prevalent while the other forces become more insignificant. Hence, $NORM(x, n \rightarrow \infty) = (\text{abs}(F_i)^n)^{1/n} = \text{abs}(F_i)$, where i is the index of the absolute maximum force, and $NORM(x, n \rightarrow \infty) = \max(\text{abs}(x))$. The objective function can alternatively be written as:

$$Objfun = NORM(x, n \rightarrow \infty) \quad (4-4)$$

The optimization problem in MatLab can be defined as:

$$\text{Minimize: } Objfun = NORM(x, n \rightarrow \infty)$$

$$\text{Subject to: } Ax = b$$

When the objective function is minimized, an angle $A1$ is found such that the magnitude of the maximum absolute force in the one-story truss is minimized, for optimum structural strength.

The built in MatLab function “fmincon” (using sequential quadratic programming) was used to solve the optimization problem.

When optimizing more complicated structures, several minima may exist. To ensure the global minimum is attained, two hundred random starting values are used for each optimization pass.

4.3. Two-Story Truss

The two-story truss is shown in Figure 4-13.

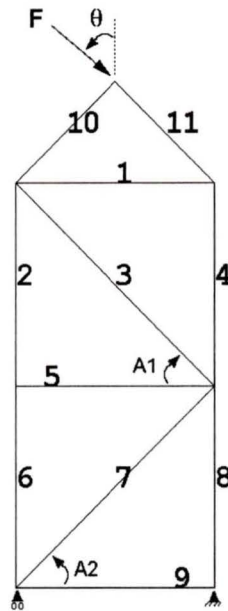


Figure 4-13 Two-story adaptive truss

The structure was analyzed in Ansys; and the results verified in MatLab are shown in Table 4-3.

Table 4-3 Two-story results

App. F θ (deg)	Ansys Opt. A1 (deg)	MatLab Opt. A1 (deg)	Ansys Opt. A2 (deg)	MatLab Opt. A2 (deg)	Ansys S. Str. (KN)	MatLab S. Str. (KN)	Fixed S. Str. (KN)	Elem. #	T=1 C=0
-90	75.00	75.00	44.70	45.00	13	13	10	2	0
-80	73.20	73.20	38.70	38.80	15	15	11	8	1
-70	69.20	69.20	34.00	33.80	17	17	12	8	1
-60	68.50	68.50	41.00	36.30	20	20	14	2	0
-50	77.90	77.90	39.80	42.30	25	25	16	2	0
-40	81.40	81.40	31.40	30.40	47	47	19	3	0
-30	72.70	72.70	37.10	37.70	58	58	22	3	0
-20	61.60	61.60	44.70	45.10	53	53	26	1	1
-10	52.40	52.40	47.90	47.80	51	51	35	1	1
0	45.00	45.00	45.20	45.00	52	52	52	6	0
10	45.00	45.00	60.30	63.20	45	45	28	4	0
20	44.00	44.20	73.60	74.00	41	41	20	4	0
30	36.00	36.10	81.40	82.70	36	36	15	4	0
40	27.60	27.60	81.80	82.20	30	30	13	4	0
50	20.30	20.30	76.60	77.00	24	24	12	8	0
60	15.30	15.30	67.90	68.10	19	19	11	8	0
70	12.10	12.10	58.90	59.30	17	17	10	8	0
80	9.89	9.88	51.43	51.72	15	15	10	8	0
90	15.00	15.00	45.28	45.00	13	13	10	8	0

The structural strength for the adaptive and fixed two-story trusses is shown in Figure 4-14.

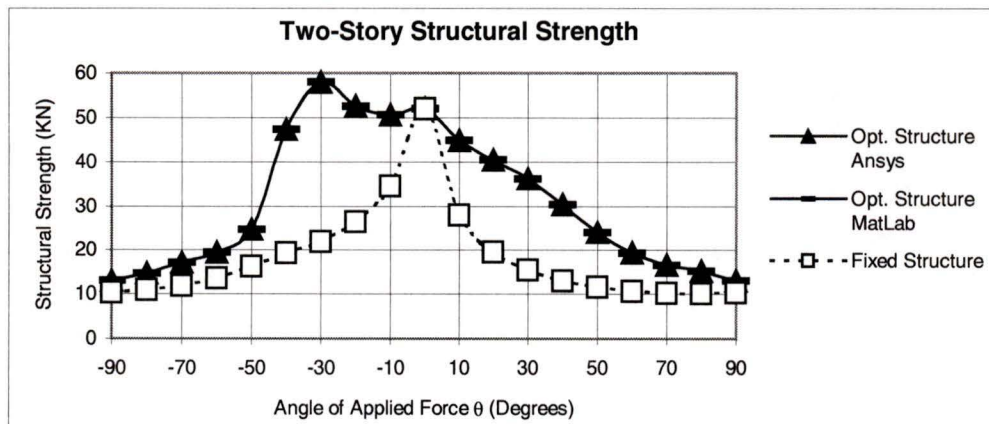


Figure 4-14 Two-story structural strength

The adaptive two-story truss is significantly stronger than the fixed truss, especially when $-50^\circ \leq \theta \leq -10^\circ$ and when $10^\circ \leq \theta \leq 80^\circ$. The adaptive shapes are presented in Figure 4-15.

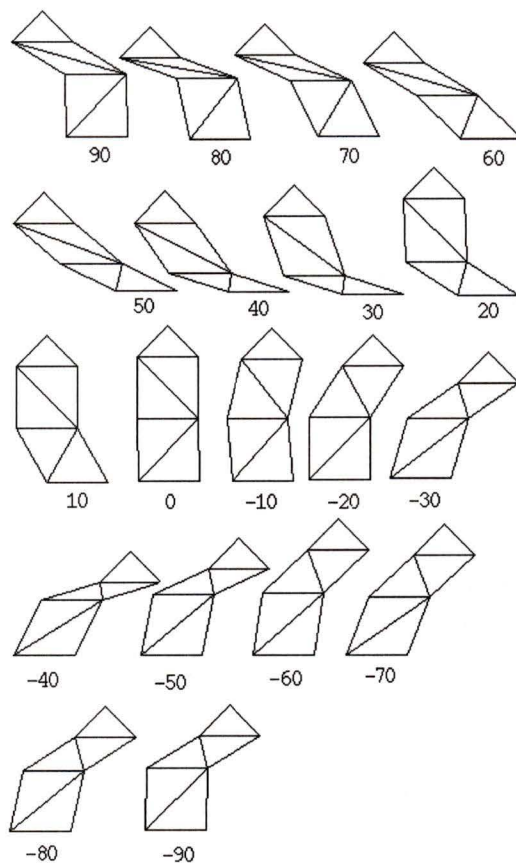


Figure 4-15 Two-story adaptive shapes

To further ensure the validity of these results, the two-story truss subjected to a unit load at an angle $\theta = -90^\circ$ is considered. This problem has more than one design variable and as a result has two local minima. To ensure the global minimum was reached, a 3D surface plot of A_1 , A_2 , and the minimum of the maximum absolute stress was created using MatLab. The plot of stress when $\theta = -90^\circ$ and $5^\circ \leq A_1, A_2 \leq 85^\circ$ is shown in Figure 4-16.

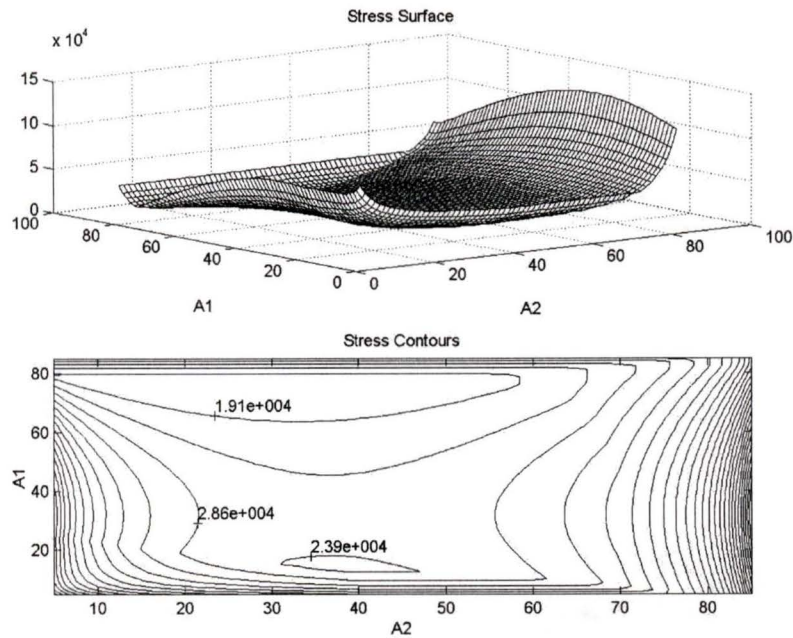


Figure 4-16 Two-story stress contour plot with $\theta = -90^\circ$

This surface shows two local minima regions. Experimenting with different starting points leads to different minima convergence as shown in Table 4-4:

Table 4-4 Local minima convergence for the two-story truss with $\theta = -90^\circ$

App. F θ (deg)	Opt. A1 (deg)	Opt. A2 (deg)	Max Stress (Pa)	Elem. #	T=1 C=0
Minima #1 -90	15.00	44.80	20002	8	1
Minima #2 -90	75.00	45.00	19994	2	0

The second minimum is the global minimum. To ensure the global minimum was reached, two hundred random starting points were used for each optimization.

Plotting the contour plots for two additional angles $\theta = -30^\circ$ and $\theta = 80^\circ$ produced similar results as shown in Figure 4-17 and Figure 4-18.

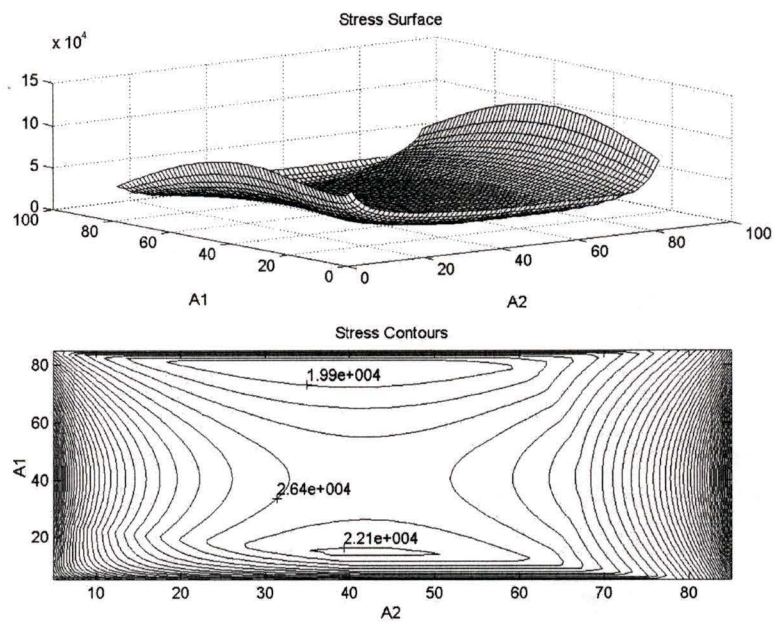


Figure 4-17 Two-story stress contour plot with $\theta = -30^\circ$

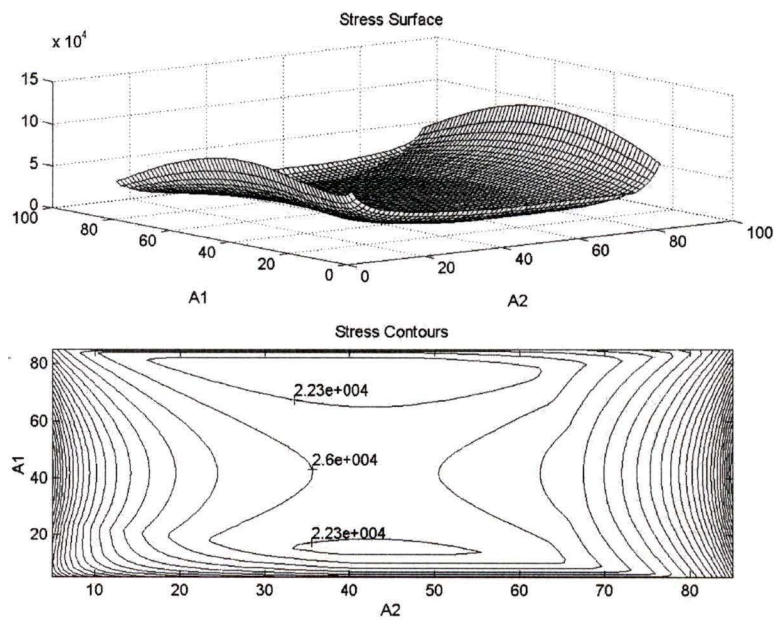


Figure 4-18 Two-story stress contour plot with $\theta = 90^\circ$

The MatLab 3D surface plots verify the two-story adaptive shapes.

4.4. Pyramid Structure

The 3D pyramid structure, shown in Figure 4-19, is statically determinate.

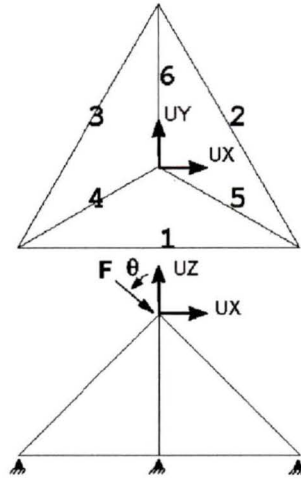


Figure 4-19 Adaptive pyramid

Elements 4, 5, and 6 are active, however the pyramid must always remain a height of 1m. Elements 1, 2, and 3 remain a fixed length of 2m. During the optimization, the apex of the pyramid is confined to move inside the rectangle shown in Figure 4-20.

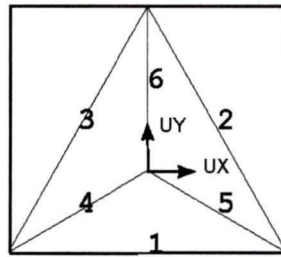


Figure 4-20 Boundary conditions for the apex of the pyramid

Optimizing the pyramid when subjected to a unit load at various angles of θ produced Table 4-5.

Table 4-5 Pyramid results

App. F θ (deg)	Ansys Apex UX (deg)	MatLab Apex UX (deg)	Ansys Apex UY (deg)	MatLab Apex UY (deg)	Ansys S. Str. (KN)	MatLab S. Str. (KN)	Fixed S. Str. (KN)	Elem. #	T=1 C=0
-90	0.00	0.00	-0.57	-0.58	37	37	34	4	1
-60	1.00	1.00	0.87	0.86	43	43	28	4	1
-30	0.79	0.79	-0.06	-0.06	57	58	32	5	1
0	0.00	0.00	0.00	0.00	51	51	51	5	1
30	-0.79	-0.79	-0.06	-0.06	57	58	32	6	1
60	-1.00	-1.00	0.87	0.86	43	43	28	6	1
90	0.00	0.00	-0.57	-0.58	37	37	34	4	0

The rightmost two columns indicate the maximum stress element and its state of tension or compression in the optimized configuration. The structural strengths are shown in Figure 4-21.

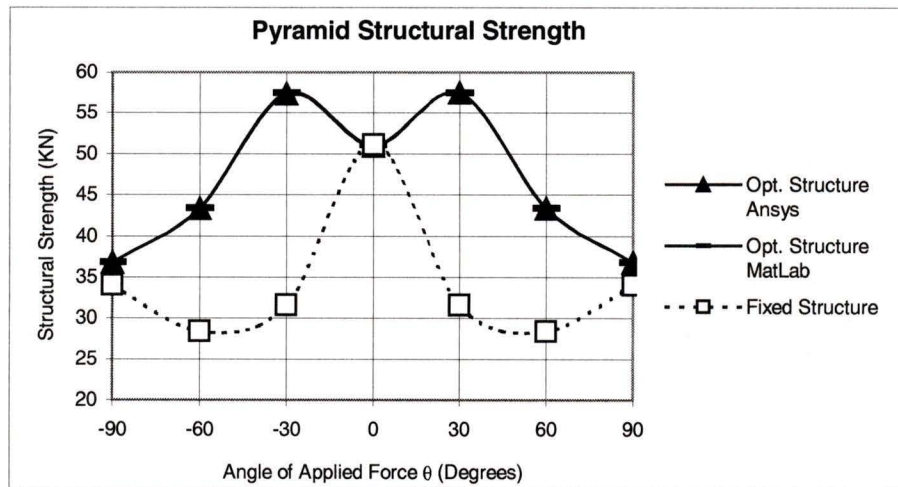


Figure 4-21 Pyramid structural strength

The adaptive pyramid is exceptionally strong when $\theta = \pm 30^\circ$. The adaptive shapes are presented in Figure 4-22.

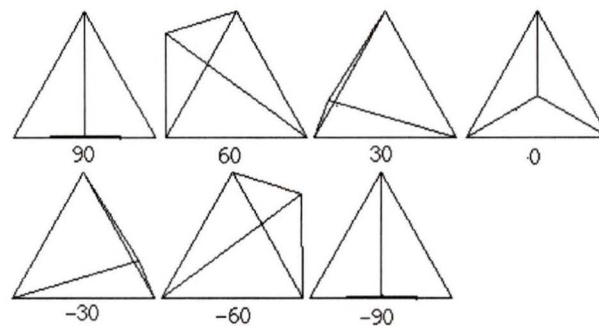


Figure 4-22 Pyramid adaptive shapes

As expected, since the pyramid is a symmetric structure the maximum stress for loadings 30° , 60° , and 90° are the same as those for -30° , -60° , and -90° .

4.5. Dome Structure

The dome structure, shown in Figure 4-23, is a statically indeterminate structure and was analyzed using only Ansys.

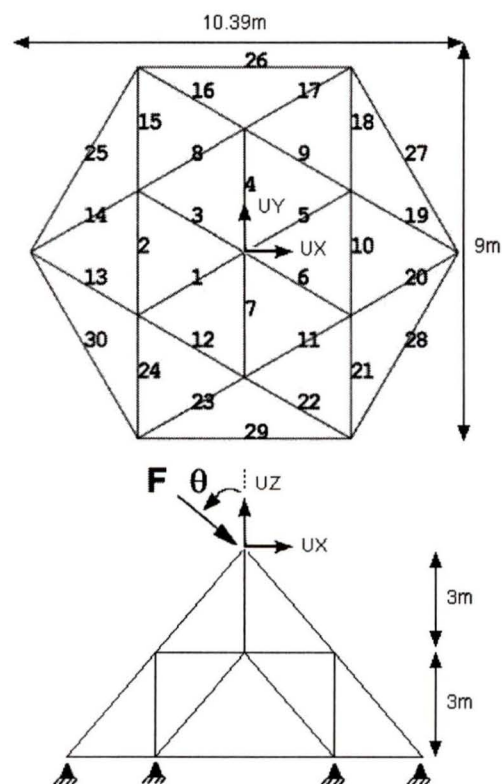


Figure 4-23 Dome structure

Similar to the adaptive pyramid, elements 1, 3, 4, 5, 6, and 7 are active permitting the apex to move, but the apex must always remain a height of 6m. During optimization, the apex of the dome is confined to move inside the rectangle shown below in Figure 4-24.

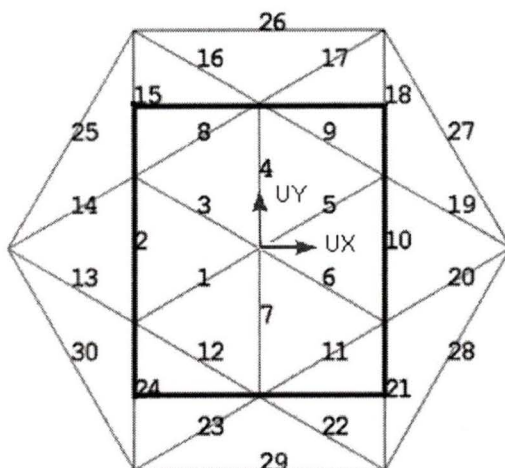


Figure 4-24 Dome apex boundary conditions

The results for optimizing the location of the dome apex are shown in Table 4-6.

Table 4-6 Dome results

App. F θ (deg)	Ansys Apex UX (deg)	Ansys Apex UY (deg)	Ansys S. Str. (KN)	Fixed S. Str. (KN)	Elem. #	T=1 C=0
-90	0.00	0.00	64	64	5	0
-60	2.60	0.00	81	55	3	1
-30	2.21	0.00	108	64	16	1
0	0.00	0.00	110	110	5	1
30	-2.11	0.00	107	64	22	1
60	-2.60	0.00	81	55	6	1
90	0.00	0.00	64	64	1	0

The rightmost two columns indicate the maximum stress element and its state of tension or compression in the optimized configuration. The structural strengths are shown in Figure 4-25.

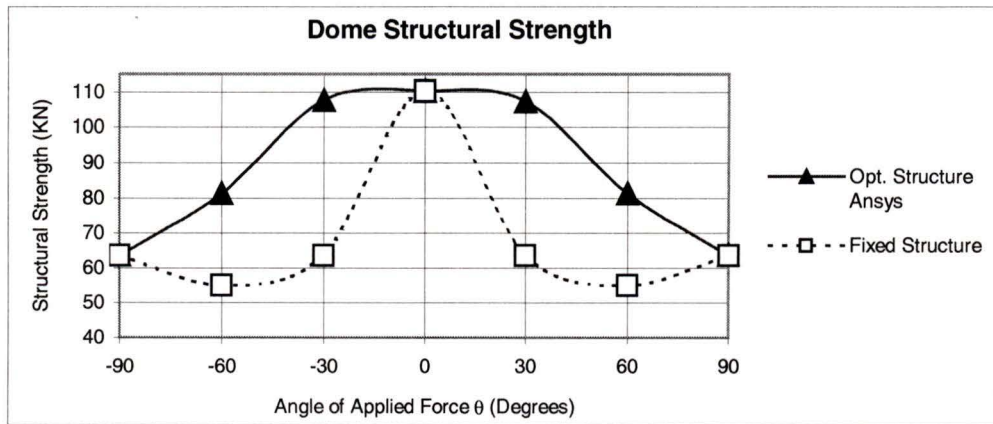


Figure 4-25 Dome structural strength

The structural strength of the adaptive dome is significantly stronger than the fixed dome when $-60^\circ \leq \theta \leq -30^\circ$ or when $30^\circ \leq \theta \leq 60^\circ$. The adaptive shapes are presented in Figure 4-26.

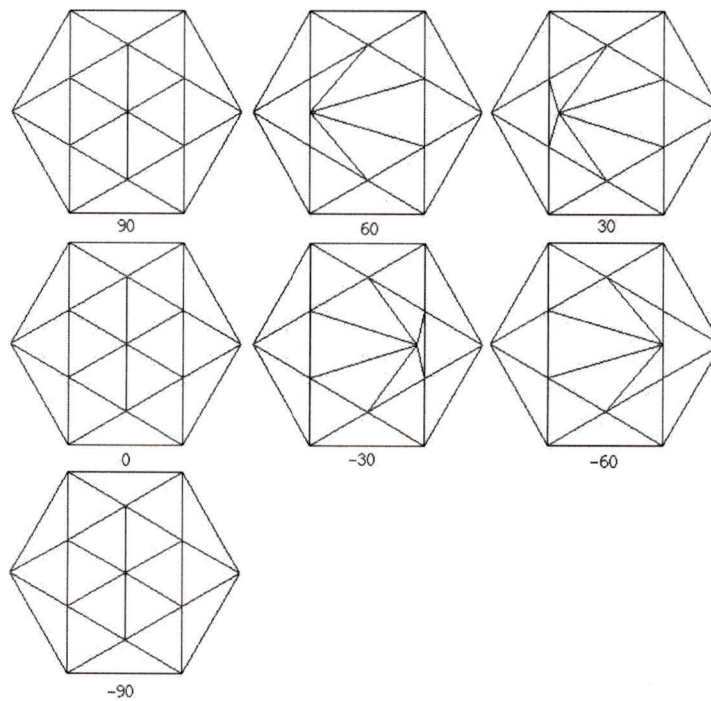


Figure 4-26 Adaptive dome shapes

As expected, since the dome is a symmetric structure, the maximum stress for loadings 30° , 60° , and 90° are the same as those for -30° , -60° , and -90° .

4.6. Asymmetric Truss Structure

The asymmetric adaptive truss structure in Figure 4-27 is a statically indeterminate structure and is analyzed using only Ansys. The top two members (elements 24 & 25) are assumed very strong and not considered in the analysis.

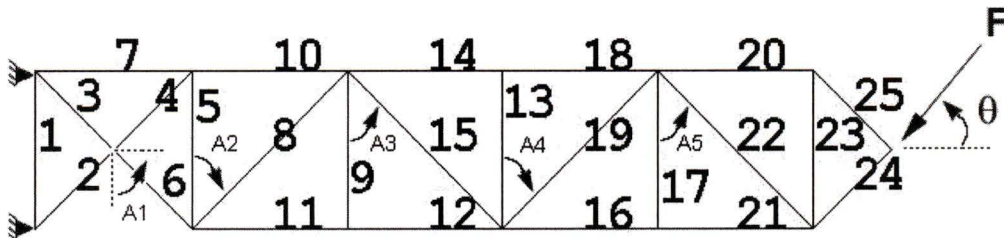


Figure 4-27 Asymmetric truss structure

The structure has five angles which can adopt a range of values between $0^\circ \leq A1 \leq 180^\circ$ and $0^\circ \leq A2, A3, A4, A5 \leq 90^\circ$. Consequently, elements 7, 8, 15, 19, and 22 are active. When a unit load is applied to the apex at angles $-90^\circ \leq \theta \leq 90^\circ$, the resultant adaptive angles are presented in Table 4-7.

Table 4-7 Asymmetric truss results

App. F θ (deg)	Ansyp Opt. A1 (deg)	Ansyp Opt. A2 (deg)	Ansyp Opt. A3 (deg)	Ansyp Opt. A4 (deg)	Ansyp Opt. A5 (deg)	Ansyp S. Str. (KN)	Fixed S. Str. (KN)	Elem. #	T=1 C=0
-90	179.98	42.13	42.51	42.11	42.15	38	3	6	1
-80	9.89	44.45	45.20	45.13	45.79	40	3	7	0
-70	21.11	45.96	45.76	44.82	44.53	42	3	7	0
-60	31.15	43.35	43.37	43.62	43.47	44	3	10	0
-50	41.23	45.68	45.47	45.26	45.48	44	3	10	0
-40	51.47	47.60	47.58	47.77	47.81	42	4	3	0
-30	61.69	43.44	43.46	43.71	43.56	41	5	10	0
-20	71.64	43.80	43.84	43.56	43.51	41	8	10	0
-10	81.52	44.94	45.00	45.08	44.84	42	15	10	0
0	91.25	45.67	45.69	45.81	45.45	44	37	10	0
10	101.59	44.33	44.19	44.24	44.36	42	13	10	0
20	112.20	44.11	44.02	44.18	43.83	40	8	10	0
30	122.42	40.76	40.64	40.99	40.81	38	5	2	0
40	132.62	47.21	46.86	47.05	46.99	37	4	2	0
50	142.62	40.28	40.19	40.35	39.99	37	3	2	0
60	152.42	44.27	44.25	44.32	44.06	38	3	2	0
70	162.19	47.59	47.23	47.43	47.36	39	3	10	0
80	172.01	52.83	52.59	52.73	52.44	39	3	4	0
90	179.98	42.13	42.51	42.11	42.15	38	3	6	0

The furthest two columns refer to the absolute maximum stress and its state of tension or compression in the optimized configuration. These results agree with the references [59]. The adaptive shapes are presented in Figure 4-28.

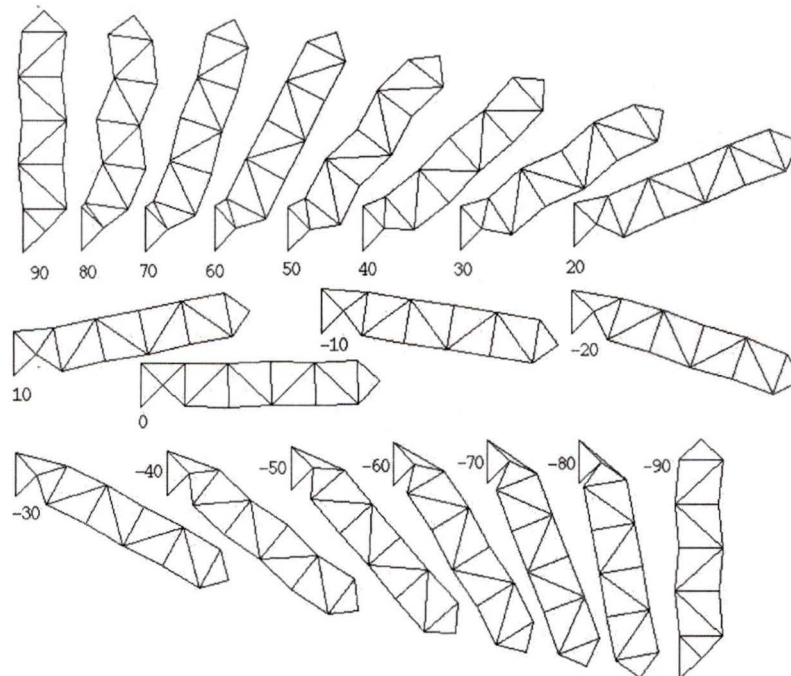


Figure 4-28 Adaptive asymmetric truss shapes

The fixed and structural strengths are shown in Figure 4-29.

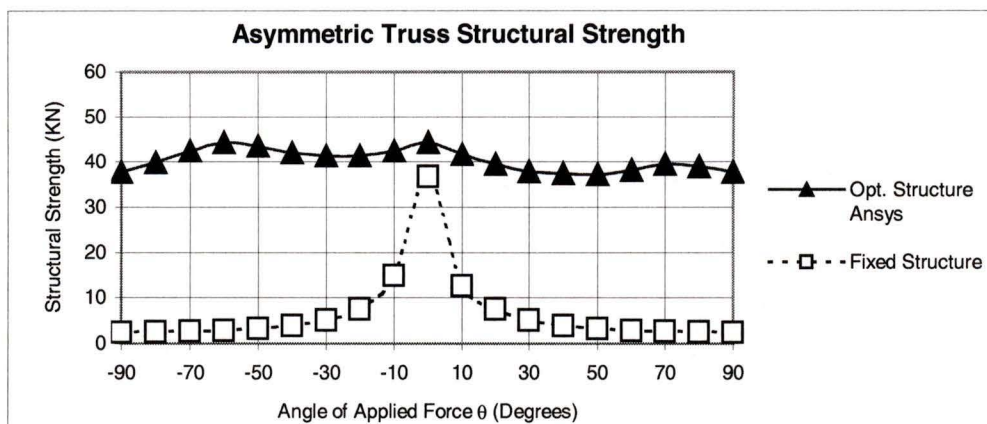


Figure 4-29 Asymmetric truss structural strength

Interestingly, unlike all the previous structures, when $\theta = 0^\circ$, the adaptive shape seems stronger when compared against the fixed structure. To inspect this result, the element stresses in the fixed structure are investigated at angles near $\theta \approx 0^\circ$, (with $A_1=90^\circ$ and $A_2, A_3, A_4, A_5 = 45^\circ$). The results are shown in Figure 4-30.

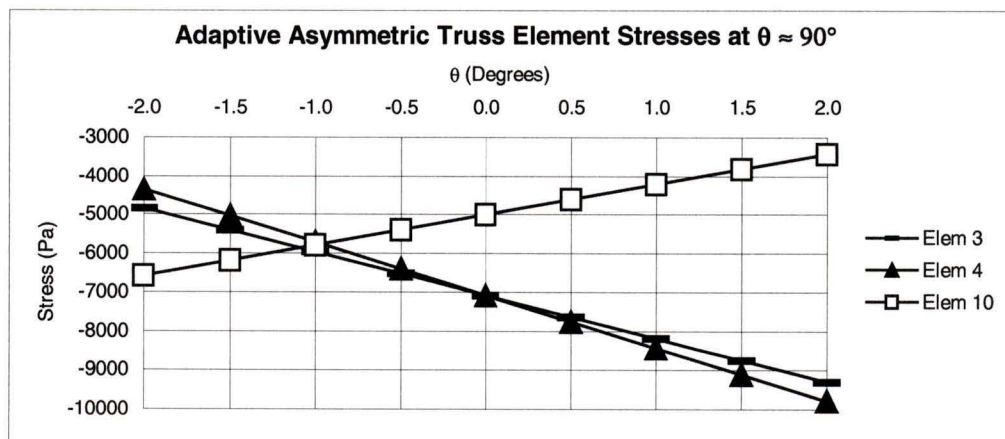


Figure 4-30 Adaptive asymmetric truss element stresses for angles $\theta \approx 90^\circ$

Logically, as θ increases, element 10 is put under less compression, and elements 3 and 4 are put under more compression. However, because the structure is not symmetric, the minimum of the maximum stress occurs at $\theta = -1.09^\circ$. This data point is shown in Figure 4-31.

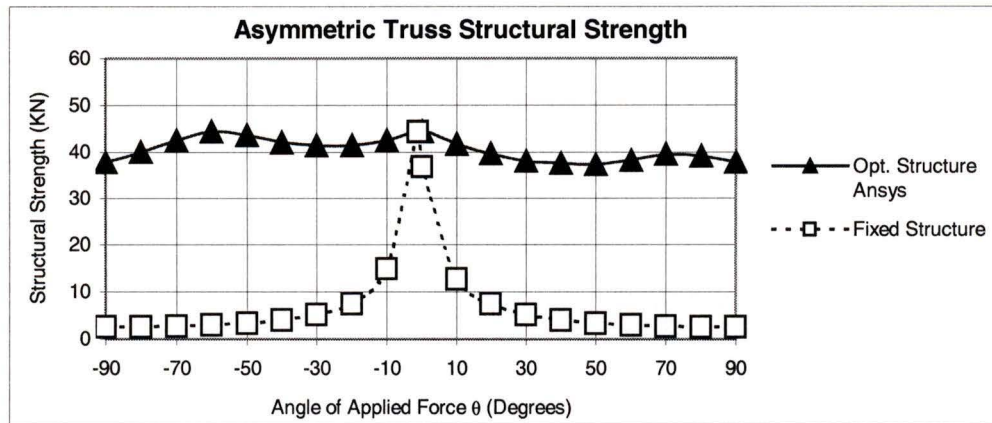


Figure 4-31 Asymmetric truss structural strength with extra data point $\theta = -1.09^\circ$

The structural strength for the asymmetric structure is extremely sensitive for angles near $\theta \approx 0^\circ$.

4.7. Symmetric Truss Structure

The symmetric truss structure, shown in Figure 4-32, is the same as the asymmetric truss structure except it has one extra element. Element number 24 is an active element and works in conjunction with active element 7 to rotate the base through an angle $0^\circ \leq A1 \leq 180^\circ$. Therefore, elements 7, 24, 8, 15, 19, and 22 are active. The top two members (elements 25 & 26) are assumed very strong and not considered in the analysis.

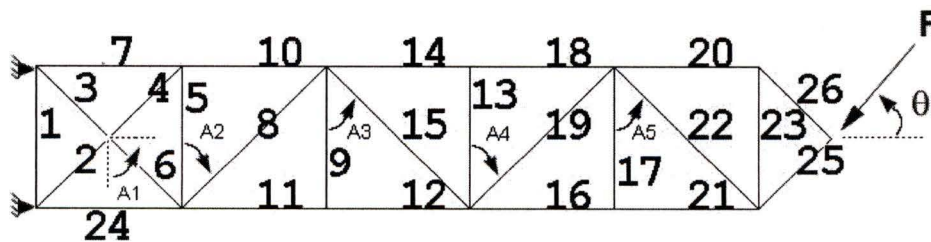


Figure 4-32 Symmetric truss structure

When a unit load is applied to the apex at angles $-90^\circ \leq \theta \leq 90^\circ$, the results in Table 4-8 are attained. The furthest two columns refer to the absolute maximum stress and state of tension or compression in the optimized configuration. The adaptive shapes are presented in Figure 4-33.

Table 4-8 Symmetric truss results

App. F θ (deg)	Anslys Opt. A1 (deg)	Anslys Opt. A2 (deg)	Anslys Opt. A3 (deg)	Anslys Opt. A4 (deg)	Anslys Opt. A5 (deg)	Anslys S. Str. (KN)	Fixed S. Str. (KN)	Elem. #	T=1 C=0
-90	0.0	58.6	58.7	58.6	58.4	35	5	23	1
-80	7.1	51.9	53.4	52.4	52.8	41	5	12	1
-70	15.6	50.9	51.3	51.0	50.9	47	5	12	0
-60	25.9	50.5	50.8	50.6	50.6	47	6	12	0
-50	39.2	46.4	46.4	46.2	46.1	51	6	23	1
-40	49.8	45.2	45.5	45.2	45.2	52	7	23	1
-30	60.1	45.0	44.9	45.1	45.0	52	9	23	0
-20	69.0	46.1	46.5	46.2	46.1	51	13	23	1
-10	79.4	44.7	45.1	44.9	45.7	51	20	23	1
0	89.9	45.4	45.4	45.2	45.1	52	52	23	1
10	99.4	46.0	46.1	45.9	45.8	51	21	23	1
20	109.4	46.1	46.1	45.9	45.8	51	12	23	1
30	119.0	46.0	46.6	46.1	46.1	50	9	23	1
40	129.8	45.2	45.5	45.2	45.2	52	7	23	1
50	139.9	45.3	45.5	45.4	45.1	52	6	23	1
60	149.6	49.1	49.1	48.8	48.8	46	6	23	1
70	160.8	50.4	50.8	50.5	50.4	43	5	23	1
80	171.5	52.8	52.7	52.9	52.6	40	5	4	0
90	0.0	58.6	58.7	58.6	58.4	35	5	23	0

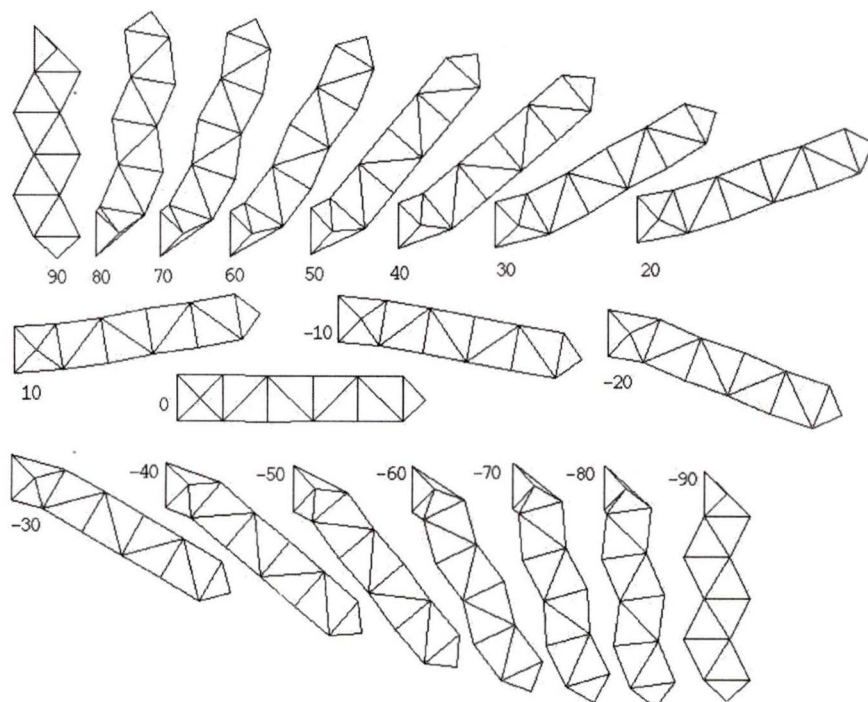


Figure 4-33 Adaptive symmetric truss shapes

The structural strengths are shown in Figure 4-34.

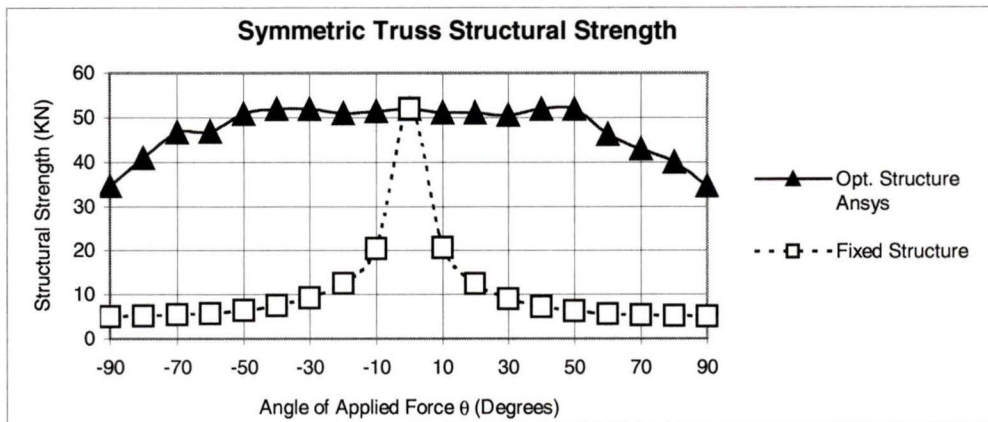


Figure 4-34 Symmetric truss structural strength

As expected, the maximum structural strength for the fixed and adaptive symmetric truss agree when $\theta = 0^\circ$, however, it is apparent that for angles $\theta \leq 50^\circ$ and $\theta \geq 50^\circ$ the structural strength begins to drop off. To further investigate the structural strength reduction when $\theta \leq 50^\circ$, consider the element stresses when $\theta = 50^\circ$, 60° , and 70° . When $\theta = 50^\circ$, Figure 4-35 is generated.

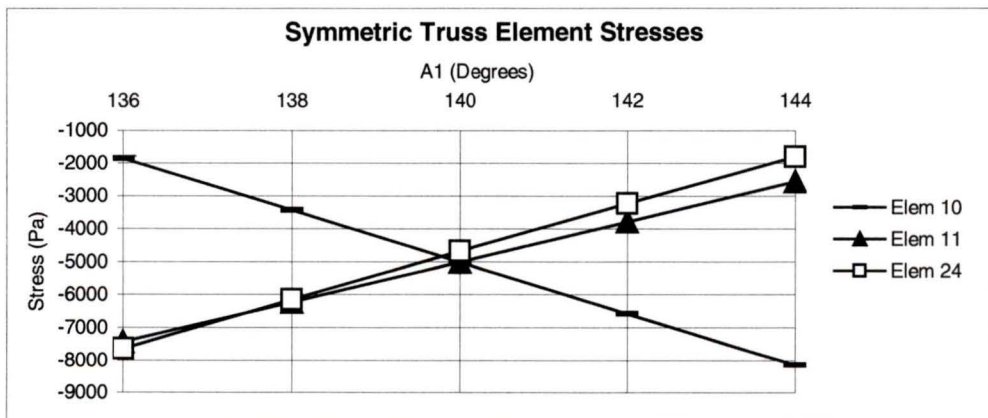


Figure 4-35 Symmetric truss element stresses for $\theta = 50^\circ$ and $A1 \approx 140^\circ$

The minimum occurs at $A1 = 140^\circ$ with an absolute value of 5000Pa. The corresponding structural strength of 52KN is attained by multiplying the unit load (1N) by the ultimate strength of 260MPa and dividing by the maximum unit load stress (5000Pa). When $\theta = 60^\circ$, Figure 4-36 is generated.

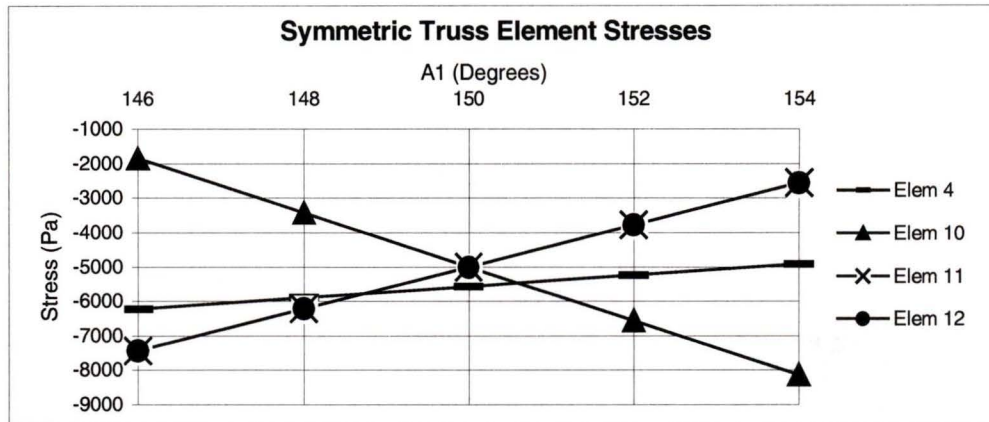


Figure 4-36 Symmetric truss element stresses for $\theta = 60^\circ$ and $A1 \approx 150^\circ$

The minimum occurs at $A1 = 150.6^\circ$ with an absolute value of 5474Pa. The corresponding structural strength is 47KN. When $\theta = 70^\circ$, Figure 4-37 is generated.

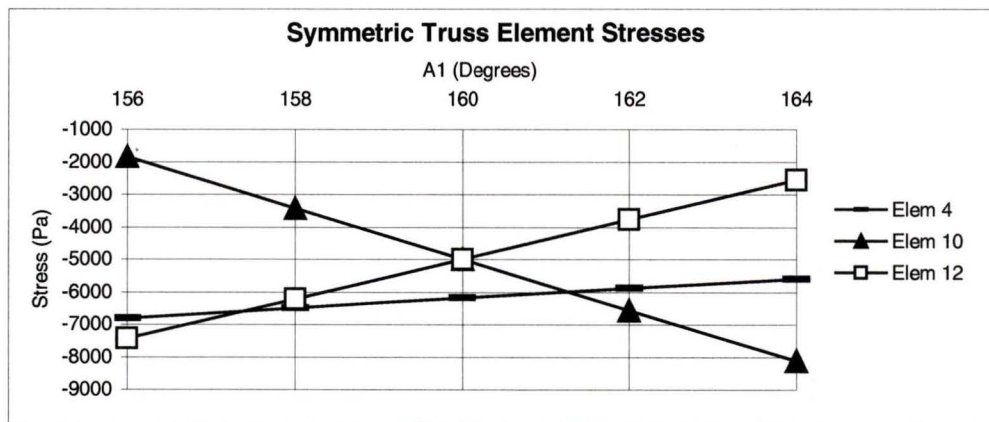


Figure 4-37 Symmetric truss element stresses for $\theta = 70^\circ$ and $A1 \approx 160^\circ$

In this case, the minimum occurs at $A1 = 161.26^\circ$ with an absolute value of 5992Pa. The corresponding structural strength is 43KN.

The element stresses in Figures 4-35, 4-36, 4-37 seem reasonable and confirm the plot of structural strength in Figure 4-34.

4.8. Tower Structure

Consider the eight-story tower shown in Figure 4-38.

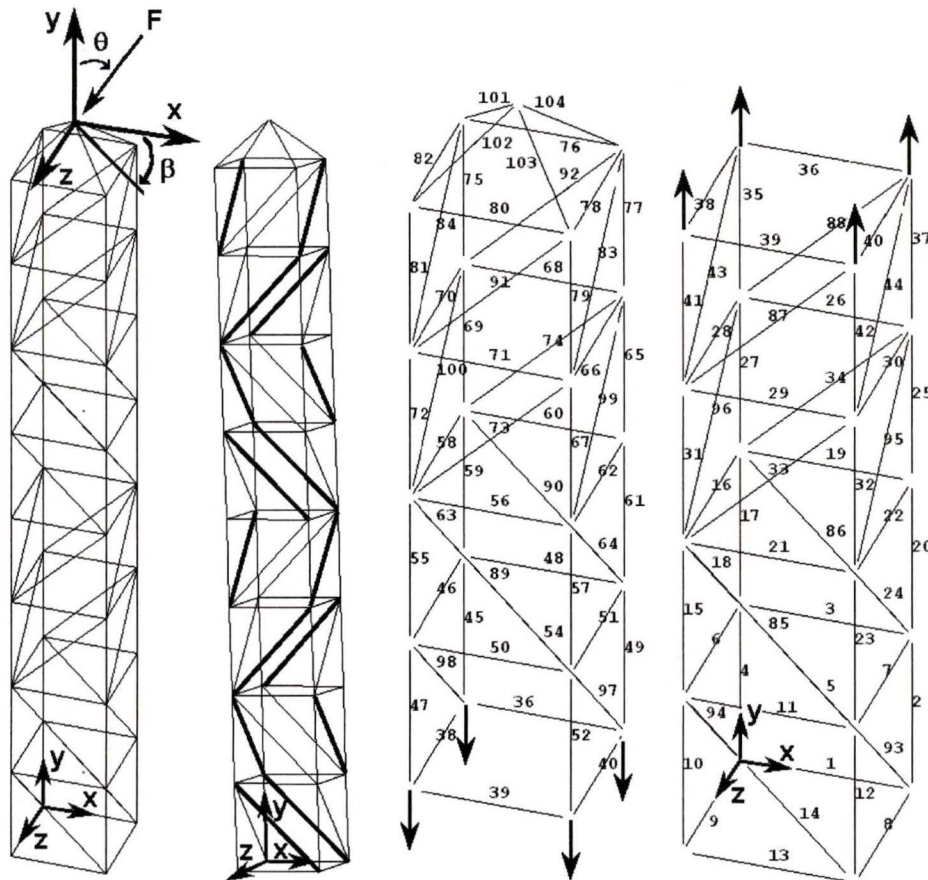


Figure 4-38 Tower structure

The leftmost picture shows the tower structure subject to a unit force at angles θ and β . The second picture from the left, shows the active elements by means of bold lines. The design variables are the angles ($A_1, A_2, A_3, A_4, A_5, A_6, A_7, A_8$) each bold line makes with the horizontal. The remaining two pictures, are the top half and bottom half of tower showing the element numbering. The top four elements (101, 102, 103, 104) are assumed very strong and not considered in the analysis.

A unit load was applied to the apex of the fixed tower structure at angles $-90^\circ \leq \theta \leq 90^\circ$, with $\beta = 0$. Due to the expensive time required to simultaneously optimizing

eight design variables, the adaptive tower structure was only optimized for angles $\theta = 0^\circ$ and $\theta = 12.5^\circ$. The results of the optimization are shown in Table 4-9.

Table 4-9 Tower results

App.F θ, β (deg)	Ansys Optimized Angles								Ansys S.Str. (KN)	Fixed S.Str. (KN)	Elem. #	T=1 C=0
	A1 (deg)	A2 (deg)	A3 (deg)	A4 (deg)	A5 (deg)	A6 (deg)	A7 (deg)	A8 (deg)				
-90,0										6.1	2	1
-80,0										6.2	2	1
-70,0										6.6	2	1
-60,0										7.2	2	1
-50,0										8.3	2	1
-40,0										9.9	2	0
-30,0										12.3	2	0
-20,0										17.0	2	0
-10,0										28.8	2	0
0,0										104.0	72	0
0,0	43.2	45.7	47.0	43.2	45.2	44.0	44.2	45.4	81.1		4	0
10,0										26.2	4	0
12.5,0	61.3	44.2	29.1	46.2	59.7	45.3	31.5	45.8	52.8		72	0
20,0										15.3	4	0
30,0										11.0	4	0
40,0										8.8	4	0
50,0										7.5	4	0
60,0										6.8	4	0
70,0										6.3	4	0
80,0										6.1	4	0
90,0										6.1	4	0

The difference in structural strengths between the fixed and adaptive tower structure can be seen in Figure 4-39.

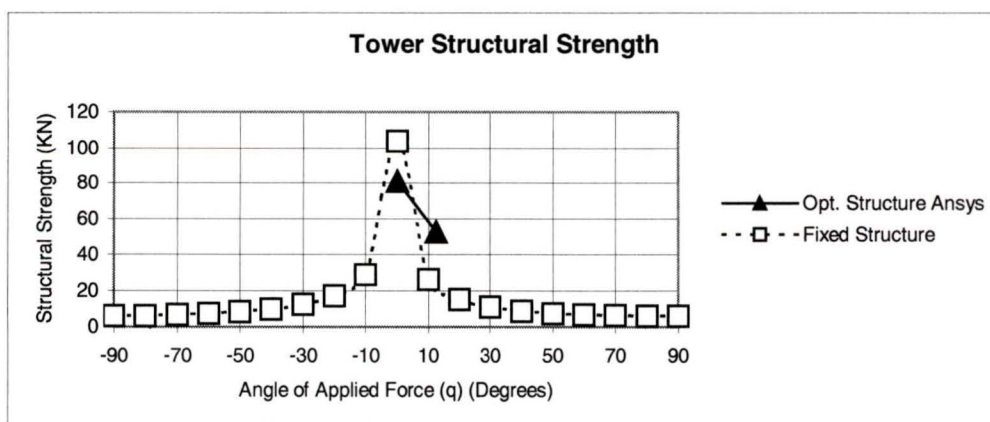


Figure 4-39 Tower structural strength

The results of structural strength for the adaptive structure are lower than expected. This is caused by the inaccuracy of the optimization results. Due to the expensive computational time of simultaneously optimizing eight design variables, the Ansys model was set to converge to a low final optimization tolerance ($\pm 2^\circ$). Evidently, the tower structure is sensitive to angles near the true optimum. The resultant shapes of the adaptive tower structure are shown in Figure 4-40.

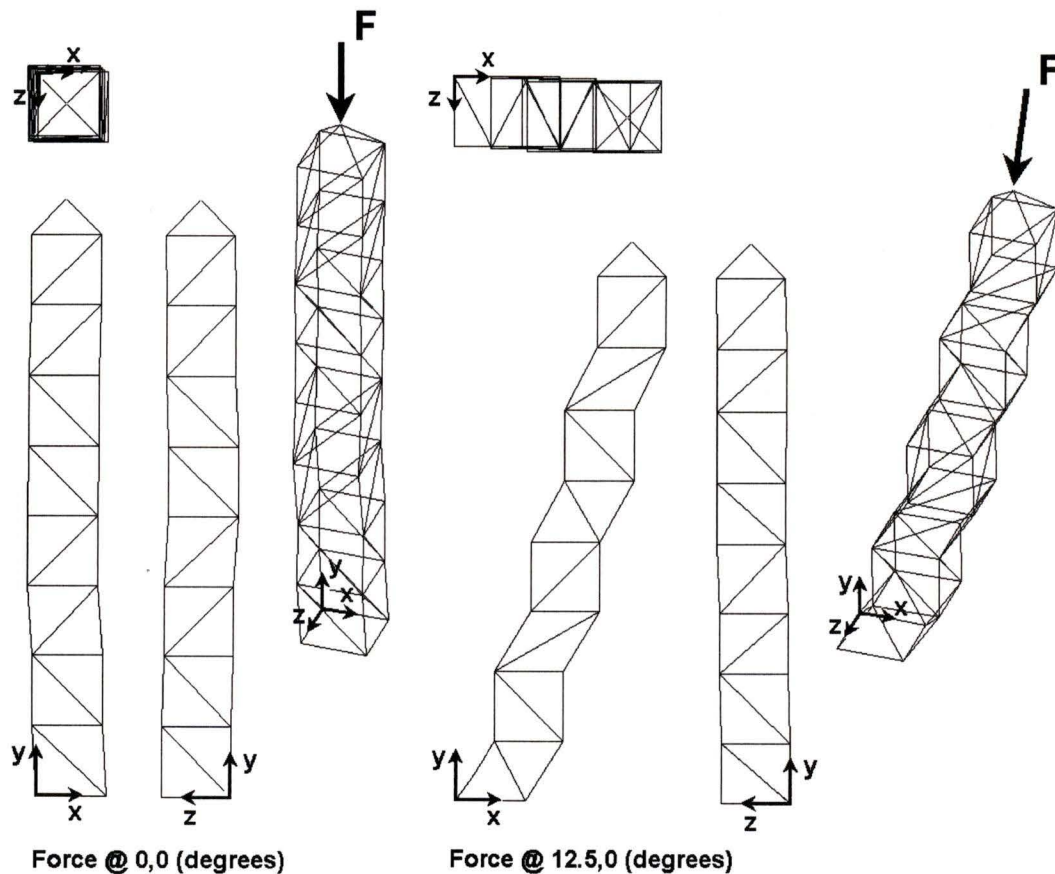


Figure 4-40 Adaptive tower shape for F at $\theta = 0^\circ$, $\beta = 0^\circ$ and $\theta = 12.5^\circ$, $\beta = 0^\circ$

Here we can see the tower tries to align itself into the direction of the applied load. To further investigate the behavior of the adaptive tower, the tower was optimized for an arbitrary angle of $\theta = 38^\circ$ and $\beta = 33^\circ$. The results of this optimization are compared to the same load applied to the fixed tower shown in Table 4-10.

Table 4-10 Adaptive tower results for F at $\theta = 38^\circ$, $\beta = 33^\circ$

App.F θ, β (deg)	Ansys Optimized Angles								Ansys S.Str. (KN)	Fixed S.Str. (KN)	Elem. #	T=1 C=0
	A1 (deg)	A2 (deg)	A3 (deg)	A4 (deg)	A5 (deg)	A6 (deg)	A7 (deg)	A8 (deg)				
38,33	74.3	25.4	16.6	64.4	74.0	25.0	15.1	65.3	9.6		72	0
38,33										8.2	4	0

The corresponding adaptive tower shape is shown in Figure 4-41.

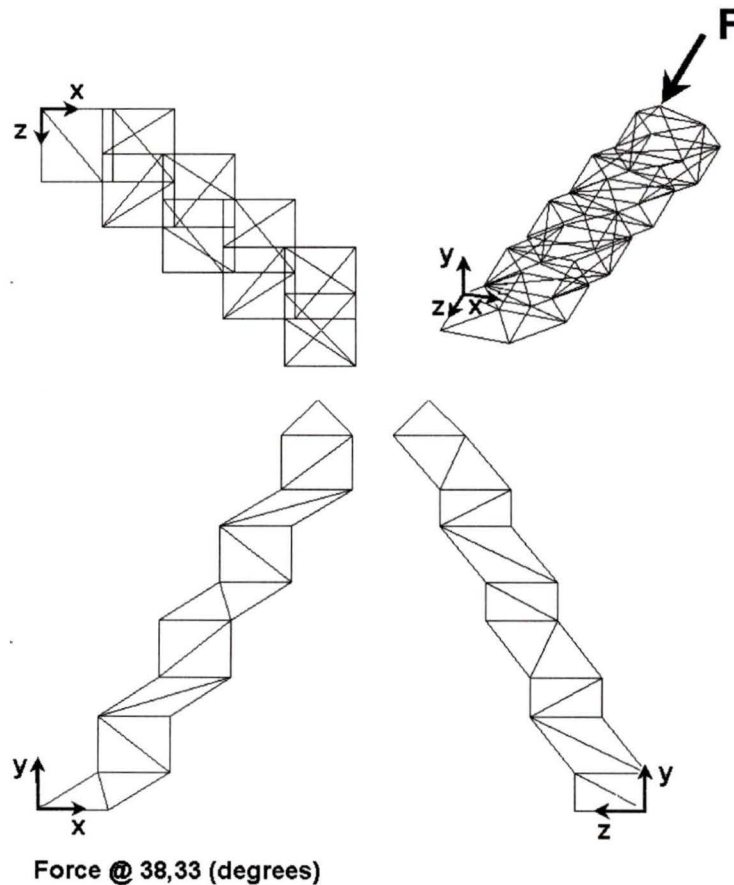


Figure 4-41 Adaptive tower shape for F at $\theta = 38^\circ$ and $\beta = 33^\circ$

Again, the tower aligns itself into the direction of the applied load to maximize its structural strength.

CONCLUSIONS AND FUTURE WORK

The motivation to advance strain induced actuator technology stems from the desire to replace polluting hydraulic actuators and their potential use in structurally adaptive space truss systems, aircraft flight control systems and automobile brake systems. This thesis investigates the design of such an actuator by using the inchworm actuator concept. To prevent re-inventing existing designs and to stimulate new ideas an extensive paper and patent search was conducted. Based on this search a new inchworm actuator was designed and prototyped. To meet the requirements defined by the funding company, Sensor Technology Limited, several options for the inchworm actuator were considered. The best design was chosen based on its ability to maintain a locked position with no electrical power, fewer number of parts to reduce manufacturing complexity, and its adjustability.

A parametric computer model of the proposed design was developed using the finite element software Ansys. The mesh accuracy of the model was validated by a less than 5% difference in results between the fine and coarsely meshed models. Tests of the brake assembly model were performed to select dimensions providing appropriate force/displacement characteristics.

To validate the computer model, a prototype was built. Unfortunately, due to manufacturing difficulties, the stacks used in the prototype were different from the projected stacks used in the original design model. For validation purposes, however, the model was modified to accurately reflect the changes in the stacks used in the prototype. The results of the design model, the prototype model, and the actual prototype are shown in Table 5.1.

The results of the prototype and the Ansys prototype model differ by less than 9% validating the computer simulations. It is expected, therefore, that if the design stacks were supplied and used in the prototype, the results would be similar to those of the design model. This task is recommended to be continued as future work.

The major advantage of this new actuator is its adjustment capabilities. All previously developed actuators do not have a simple means of adjustment. In the case of Frank et al. [34], for example, the tolerance between output shaft and clamping stacks is $5\mu\text{m}$ (0.000197in). This makes the actuator extremely delicate. Any slight temperature variation between dissimilar materials or bending of the output shaft (by an off-axis load, for example) would cause the output shaft to lock in position. To safeguard against this the proposed design incorporates adjustment nuts to allow fine-tuning of clearance surfaces. This makes the actuator more adjustable. Another advantage of this design offers the potential for future miniaturization. The design can be scaled down to meet dimensional constraints. Control circuitry can also be integrated into the actuator itself to minimize external wiring.

Frequency response (and actuator output speed) was limited in this case by the stack RC constant, however improvement in the stack design and manufacturing would improve the response of the actuator. The controller driving circuit has a maximum upper limit of 170Hz, whereas the limiting frequency of the inchworm cycle is 2.22Hz. Future work may be done to the stacks to enhance the maximum operational frequency and displacement. Moreover, the natural frequency of the actuator system may be investigated through possible future experimentation. At high frequencies, the ramping signal of the controller may also prove useful.

Quantification of strains due to thermal gradients has not been explored, but is another very important issue. The design was manufactured with all components using titanium to eliminate unwanted thermal expansions between dissimilar metals. The stacks, however, with a thermal coefficient of ($\sim 1 \times 10^{-6}/\text{C}$ [41]) are pre-stressed by a titanium threaded rod with thermal coefficient ($9.5 \times 10^{-6}/\text{C}$ [40]). It is expected that during operation heating will occur and the threaded rod will expand more than the stacks. The expansion is expected to alleviate some of the stack pre-stress. To guard against this situation, the rod was wrapped with thermal insulating tape. A more detailed study of this phenomenon should be undertaken at a future date.

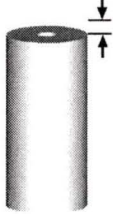
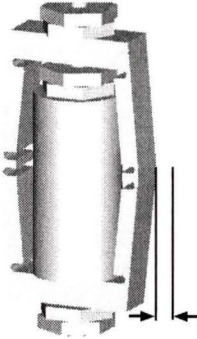

The force of friction between the pads and the outer casing is another important aspect. Hard materials associated with high precision machining exhibit low coefficients of friction [52]. Conversely, materials associated with high coefficients of friction are soft and show significant wear. Future research should be done on special

coatings that increase the coefficient of friction while simultaneously exhibiting low wear characteristics.

A potential application of the proposed actuator was investigated by its integration into adaptive truss structures. Numerical results indicate adaptive structures demonstrate significant increases in structural strength when compared with equivalent conventional structures. Future work that can be performed on adaptive structures may include control systems with closed loop feedback, sensitivity near optimized geometries and an investigation on optimal actuator placement.

Additional applications of the proposed actuator could be introduced into the automotive market through adaptive suspensions or advanced braking systems. The design may also be integrated into the design of aircraft in active control surface applications.

Table 5-1 Summary of inchworm actuator results

Inchworm Actuator Results	Ansys Design Model	Ansys Prototype Model	Measured from Prototype
Brake Stack Free Disp. (um) 	30.0	27.1	26.0
Brake Pad Disp. (um) 	107.4	78.2	71.1
Extending Stack Free Disp. (um) 	39.9	16.7	16.0
Brake Pad Blocked Force (N): 25.4 Clearance 50.8 Clearance	64.2 41.6	18.6 7.5	---
Actuator Output Force (N): 25.4 Clearance 50.8 Clearance	83.5 54.0	24.2 10.0	15.1
Max. Operating Freq. (Hz) Actuator Speed (mm/min)	--- ---	2.22 1.0	0.33 0.2

REFERENCES

- [1] K. Uchino, "Materials Issues in Design and Performance of Piezoelectric Actuators- An Overview", *Acta Materials*, Vol. 46, No. 11, pp3745-3753 , 1998.
- [2] K. L. Koudela and B. Hassier, "A 500Hz Mechanical Amplifier for use with Multilayered Piezoelectric Actuators," *Proceedings of The Ninth International Conference on Adaptive Structures and Technologies*, Boston, Massachusetts, U.S.A., p13-21, October 1998.
- [3] G. R. Lui, Z. Yili, K. Y. Lam, X. Q. Peng and J.Tani, "Finite Element Modelling of Piezoelectric Sensors and Actuators Bonded in Thick Composite Laminates," *Proceedings of The Eighth International Conference on Adaptive Structures and Technologies*, Wakayama, Japan, p113-122, October 1997.
- [4] D. R. Martinez, T. D. Hinnerichs and J. M. Redmond, "Vibration Control For Precision Manufacturing Using Piezoelectric Actuators," *Proceedings of The Sixth International Conference on Adaptive Structures and Technologies*, Rome, Italy, p3-22, October 1997.
- [5] B. Pletner and H. Abramovich, "Piezoelectric Sensors For Adaptive Suspensions," *Proceedings of The Sixth International Conference on Adaptive Structures and Technologies*, Rome, Italy, p404-417, October 1997.
- [6] Y. B. Cohen, S. Leary, M. Shahinpoor, J. O. Harrison and J. Smith, "Electro-Active Polymer (EAP) Actuators for Planetary Applications," *Proceedings of The SPIE Smart Structures and Materials*, Newport Beach, California, Vol. 3669, p57-63, March, 1999.
- [7] P. C. Hughes, W. G. Sincarsin and K. A. Carroll, "Trussarm-A Variable Geometry Truss Manipulator," *Proceedings of The First Joint Japan/US Conference on Adaptive Structures*, Nagoya, Japan, p715-725, November 1991.

- [8] S. Shao and Y. Murotsu, "Some Approaches to the Optimal Adaptive Geometries of Intelligent Truss Structures," Proceedings of The First Joint Japan/US Conference on Adaptive Structures, Nagoya, Japan, p743-771, November 1991.
- [9] K. Uchino, "Recent Development of Piezoelectric Actuators for Adaptive Structures," Proceedings of The Third International Conference on Adaptive Structures and Technologies, San Diego, California, U.S.A., p245-257, November 1992.
- [10] A. Benjeddou, M. A. Trindade and A. Ohayon, "A Finite Element Model for Shear Actuated Adaptive Structures," Proceedings of The Eighth International Conference on Adaptive Structures and Technologies, Wakayama, Japan, p133-142, October 1997.
- [11] M. E. Regelbrugge, and B. J. Huribut, "Developing of a Self-Sensing Multilayer Piezoceramic Actuator for Structural Damping Applications," Proceedings of The Fourth International Conference on Adaptive Structures and Technologies, Cologne, Federal Republic of Germany, p29-42, November 1993.
- [12] H. Janocha, D. J. Jendritza, and J. Schafer, "Active Damping of Forced Periodic Vibrations with Solid State Actuators," Proceedings of The Fourth International Conference on Adaptive Structures and Technologies, Cologne, Federal Republic of Germany, p497-511, November 1993.
- [13] M. T. D'Eleuterio and G. B. Sincarsin, "Articulatory Dynamics of Variable-Geometry Truss Structures", Univ of Toronto Source: Jt Japan/US Conference on Adaptive Structures, Proceedings of the Second Joint Japan/U.S. Conference on Adaptive Structures, Nov 12-14 1991, 1992, Nagoya, Jpn Sponsored by: PA, Publ by Technomic Publ Co Inc, Lancaster, USA, p 621.
- [14] R. Stibitz, "Incremental Feed Mechanisms", U.S. Patent: 3,138,749, 1964.
- [15] M. McNancy, "Inchworin actuator", U.S. Patent: 5,3323,942, 1994.
- [16] K. Hsu and A. Biatter, "Transducer", U.S. Patent: 3,292,019, 1966.

- [17] G.L. Locher, "Micrometric linear actuator", U.S. Patent: 3,296,467, 1967.
- [18] A.D. Brisbane, "Position control device", U.S. Patent: 3,377,489, 1968.
- [19] G. V. Galutva, "Device for precision displacement of a solid body", 1987.
- [20] R. A. Bizzigotti, "Electromechanical translational apparatus". US. Patent: 3,902,085, 1975.
- [21] Y. Sakitani, "Stepwise fine adjustment", U.S. Patent: 3,952,215, 1976.
- [22] M. Ishikawa and Y. Sakitani, "Two-directional piezoelectric driven fine adjustment device", U.S. Patent: 4,163,168, 1979.
- [23] G. O'Neill, "Electromotive actuator", U.S. Patent: 4,219,755, 1980.
- [24] T. Taniguchi, "Piezoelectric driving apparatus", US Patent: 4,454,441, 1984.
- [25] A. Hara, H. Takao, Y. Kunio, T. Sadayuki and N. Keiji, "Electromechanical translation device comprising an electrostrictive drive of a stacked ceramic capacitor type", U.S. Patent: 4,570,096, 1986.
- [26] C. W. Staufenberg and R. J. Hubbell, "Piezoelectric electromechanical translation apparatus", U.S. Patent: 4,622,483, 1986.
- [27] T. Fujimoto, "Piezo-electric actuator and stepping device using same", U.S. Patent: 4,714,855, 1987.
- [28] T. Murata, "Drive apparatus and motor unit using the same", U.S. Patent: 4,974,077, 1990.
- [29] S. Shibuta, Y. Morino, Y. Shibayama and K. Sekine, "Adaptive Control of Space Truss Structures by Piezoelectric Actuator", Tsukuba Space Cent Source: Jt Japan/US Conference on Adaptive Structures, Proceedings of the Second Joint Japan/U.S. Conference on Adaptive Structures, Nov 12-14 1991, 1992, Nagoya, Japan Sponsored by: PA, Publ by Technomic Publ Co Inc, Lancaster, USA, p 245.

- [30] G. Rennex, "Inchworm actuator", U.S. Patent: 5,3323,942, 1994.
- [31] T. Pandell and E. Garcia, "Design of a piezoelectric caterpillar motor" Proceedings of the ASME aerospace division, AD-Vol. 52, p. 627-648, 1996.
- [32] T. P. Galante, "Design and Fabrication of a High Authority Linear Piezoceramic Actuator: The PSU H3 Inchworm", The Pennsylvania State University: Graduate School, Department of Mechanical Engineering, August 1997.
- [33] S. Canfield, S. Edinger, B. M. Frecker, and G. Koopmann, "Design of Piezoelectric Inchworm Actuator and Compliant End-Effect for Minimally Invasive Surgery", Society of Photo-Optical Instrumentation Engineers, p 835-843, Part of the SPIE Conference on Smart Structures and Integrated Systems, Newport Beach California, March 1999.
- [34] J. Frank, G. Koopmann, W. Chen and G. A. Lesieutre, "Design and Performance of a High Force Piezoelectric Inchworm Motor", Proceedings of SPIE - The International Society for Optical Engineering , v 3668, n II, Proceedings of the 1999 Smart Structures and Materials - Smart Structures and Integrated Systems, 1999, Society of Photo-Optical Instrumentation Engineers, Bellingham, WA, USA, p 717-723.
- [35] Dr. H. W. King, "Mechanical Engineering University of Victoria", Professor, Private Communication, Sept. 2001.
- [36] The Materials Information Society, "Ceramics and Glasses", Vol 4, 1991.
- [37] K. Uchino, "Piezoelectric Actuators and Ultrasonic Motors", 1997, Kluwer Academic Publishers.
- [38] Sensor Technology Limited, "Measurement of Properties of Piezoelectric Ceramics", publication 91-300 Piezoelectric Ceramics.
- [39] J. E. Shigley and C. R. Mishcke, "Mechanical Engineering Design 5th Edition", McGraw-Hill Book Co., Singapore, International Edition 1989.

- [40] M. Capozzoli, J. Gopalakrishnan, K. Hogan, J. Massad, T. Tokarchik, S. Wilmarth, H. T. Banks, K. M. Mossi and R.C. Smith, "Modeling Aspects Concerning THUNDER Actuators," Proceedings of The SPIE Smart Structures and Materials, Newport Beach, California, Vol. 3667, p719-727, March, 1999.
- [41] Marco Inc. "Piezoceramic Stack Actuators", 2001
<http://www.marco.de/E/D/pa/ps/003.html>, (July 2001).
- [42] Sensor Technology Limited, 2000, <http://www.sensortech.ca>, (Aug. 2001).
- [43] D. Waechter, "Sensor Technology Limited", Private Communication, Jan-Nov, 2001.
- [44] V. Giurgiutiu and C. A. Rogers, "Energy-Based Comparison of High-Power Commercially-Available Induced-Strain-State Actuators," Proceedings of The Sixth International Conference on Adaptive Structures and Technologies, Rome, Italy, p113-130, October 1997.
- [45] Ansys Inc., 2001, www.ansys.com, (Aug. 2001).
- [46] J. Houghton, "Sensor Technology Limited", Private Communication, Jan. 2001.
- [47] R. Katz, "Mechanical Engineering University of Victoria", Machinist, Private Communication, Aug. 2001.
- [48] Vishay Measurements Group, Inc., 2001,
<http://www.measurementsgroup.com/guide/glossary/vonmises.htm>, (Aug. 2001).
- [49] F. P. E. Beer and R. Johnston "Mechanics of Materials 2nd Edition", McGraw-Hill Inc., United States of America, 1992.
- [50] D. Broek, Elementary Engineering Fracture Mechanics, 4th revised edition, Martinus Nijhoff Publishers, (1986).

- [51] J. Provan, "Mechanical Engineering University of Victoria", Professor, Private Communication w, June 2001.
- [52] BryCoat Inc., 2000, "Titanium Nitride"
<http://www.brycoat.com/physprop.html> (June 2001).
- [53] J. Ricmar, "Victoria Tool and Die", Private Communication, July 2001.
- [54] Analog Devices "High Accuracy 8-pin Instrumentation Amplifier – AMP02", Rev. D, Norwood MA USA.
- [55] Reference Sensor Technology Limited "SA-10 High-Voltage Power Amplifier Technical Manual", Rev. 2, March 23, 2000.
- [56] K. Sekine, Y. Shibayama, N. Iwasawa, N. Tagawa, S. Sunahara, S. Yoshida and T. Arikabe, "Identification and Adaptive Control of Flexible Truss Structures", NEC Corp Source: US/Japan.
- [57] Y. Murotsu and S. Shao, "Optimum Adaptation of Intelligent Truss Structures", University of Osaka Prefecture, Sakai, Osaka 591 Japan, Journal of Intelligent Material Systems and Structures, Vol. 1, p 175-188, April 1990.

VITA

Surname: Burns

Given Names: Stanley George

Place of Birth: Grand Forks, British Columbia, Canada

Educational Institutions Attended:

University of Victoria

1994 to 2001

Degrees Awarded:

B.Eng.

University of Victoria

1999

Honours and Awards:

Dean's Entrance Scholarship

1994

Publications:

S. Burns, A. Suleman, D. Waechter and E. Prasad, "Flexural Brake Mechanism for Inchworm Actuator", Proceedings of the CANSMART Workshop, Montreal, QB, October 22-23, 2001

UNIVERSITY OF VICTORIA PARTIAL COPYRIGHT LICENSE

I hereby grant the right to lend my thesis to users of the University of Victoria Library, and to make single copies only for such users or in response to a request from the Library of any other university, or similar institution, on its behalf or for one of its users. I further agree that permission for extensive copying of this thesis for scholarly purposes may be granted by me or a member of the university designated by me. It is understood that copying or publication of this thesis for financial gain by the University of Victoria shall not be allowed without my written permission.

Title of Thesis:

Design and Modeling of an Electrostrictive Inchworm Actuator

Author:



Stan Burns

Date:

Dec 12, 2001